LOW-FREQUENCY VARIABILITY OF CURRENTS IN THE DEEPWATER EASTERN GULF OF MEXICO

A Thesis

by

KELLY LYNNE COLE

Submitted to the Office of Graduate Studies of
Texas A&M University
in partial fulfillment of the requirements for the degree of

MASTER OF SCIENCE

August 2008

Major Subject: Oceanography

LOW-FREQUENCY VARIABILITY OF CURRENTS IN THE DEEPWATER EASTERN GULF OF MEXICO

A Thesis

by

KELLY LYNNE COLE

Submitted to the Office of Graduate Studies of
Texas A&M University
in partial fulfillment of the requirements for the degree of

MASTER OF SCIENCE

Approved by:

Chair of Committee,	Steven F. DiMarco
Committee Members,	Matthew K. Howard
	Richard S. Mercier
Head of Department,	Piers Chapman

August 2008

Major Subject: Oceanography

ABSTRACT

Low-Frequency Variability of Currents in the
Deepwater Eastern Gulf of Mexico. (August 2008)
Kelly Lynne Cole, B. S., Texas A&M University
Chair of Advisory Committee: Dr. Steven F. DiMarco

Vertical structure of the low frequency horizontal currents at the northern edge of the Loop Current during eddy shedding events is observed using concurrent hydrographic, moored, and satellite altimetry data from 2005. Dynamic modes are calculated at three deep (~3000 m), full water-column moorings in the eastern Gulf of Mexico. Time-series of the barotropic and first two baroclinic modes are found using a least squares minimization that fits theoretically derived modes to observed moored velocity data.

EOF analyses show that the majority of observed variance is explained by a surface-trapped mode that is highly coherent with the temporal amplitudes of the first baroclinic mode, and a lower, but significant percentage of variance is captured in bottom-intensified modes. Amplitudes of the second empirical mode indicate that currents are more coherent in the ocean interior approaching the Loop Current, as more variance is explained by this mode at the southernmost mooring near the Loop Current.

A dynamic mode decomposition of the horizontal currents reveals that the barotropic and first baroclinic modes exhibit low frequency variability and eddy time scales of 10 – 40 days. Second baroclinic mode amplitudes show higher frequency variability and shorter time scales. A model utility test for the least squares fit of modeled to observed velocity shows that the second baroclinic mode is useful to the statistical model during 50 – 85 % of the mooring deployment, and is particularly necessary to the model when cyclonic features are present in the study area. The importance of the second baroclinic mode to the model increases significantly closer to the Loop Current.

High-speed currents associated with the Loop Current and anticyclones stimulate a strong first baroclinic response, but the second baroclinic mode amplitudes are found to be similar in magnitude to the first baroclinic mode amplitudes at times. This happens episodically and could be an indication of higher order dynamics related to frontal eddies or Loop Current eddy shedding.

DEDICATION

This thesis is dedicated to my parents, Danny and Kay Cole.

ACKNOWLEDGEMENTS

I owe the completion of this thesis to many individuals. I would like to thank the U.S. Department of the Interior Mineral Management Service, whose funding for the Survey of Currents in the Eastern Gulf of Mexico Study under contract number 1435-01-04-CT-34239 made this research possible. I especially appreciate the support and guidance of Dr. Alexis Lugo-Fernández at MMS. Thanks also goes to the researchers I've met throughout the course of the EGOM project, namely Dr. Robert Leben, whose sea surface height product I've used extensively in this thesis.

I want to thank the chair of my committee, Dr. Steven DiMarco, for his assistance and guidance in the development of my research, and for giving me the chance to go on research cruises. The 26,302 words in this thesis are not enough to say how thankful I am for the challenges and opportunities I've been presented as part of his research group. I want to thank my committee member, Dr. Matt Howard, for his assistance with data acquisition, and for teaching me how to collect an oxygen sample the proper MCH way. I appreciate the insight of my committee member, Dr. Rick Mercier, in writing this manuscript.

Thanks also goes to John Klinck of ODU, who developed the dynamic mode subroutine, and to Christopher Torrence and Gilbert P. Compo, who developed the wavelet codes used in these analyses. Credit must also go to Paul Wessel and Walter H. F. Smith, the creators of the Generic Mapping Tools (GMT) software package, which was used to create some of the maps in this thesis.

I would especially like to thank Xiaoqian Zhang for his constructive comments and advice, and for all of the valuable discussions we've shared in the coffee room, whether about science or eighties sitcoms. I also owe my gratitude to Valeriya Kiselkova and Cathy Yang Feng for making our office an inspiring, fun place to work.

I owe a tremendous debt of gratitude to the faculty, staff, and students of the Texas A&M University Department of Oceanography, especially the professors I've taken classes from and the students I've taken classes with. The friends I've made throughout my graduate studies in oceanography have made the past three years of my life both challenging and enjoyable, and I hope to work with all of them in the future. In particular, I want to thank my roommates Ruth Mullins and Julia O'Hern, and my classmates Laura Rubiano-Gómez and Chrissy Wiederwohl, for their friendship, and for not letting me spend too much time at the O&M.

Above all, I want to thank my family for their encouragement and support of my passions. I am fortunate to have parents, siblings, aunts and uncles, and a grandmother that have always cultivated the artist in me. Their efforts have fostered in me the belief that any problem is solvable, of I'm only creative enough; a conviction invaluable to any scientist. We've truly come so far.

TABLE OF CONTENTS

Page

LIST OF FIGURES

FIGURE Page

LIST OF TABLES

1. INTRODUCTION

This section discusses a brief introduction and background to the physical oceanography of the Gulf of Mexico. Surface circulation in the Gulf is summarized and Loop Current dynamics are discussed. The theories behind the physics of Loop Current ring shedding and Loop Current frontal eddies are introduced. Deep flows in the Yucatan Channel and the effects of topography on Gulf of Mexico circulation is discussed, and studies involving the partitioning of kinetic energy amongst dynamic modes are summarized as well. Scientific questions and hypotheses for this research are presented at the end of this section.

1.1 An overview of the physical oceanography of the Gulf of Mexico

The Gulf of Mexico is a subtropical, semi-enclosed basin rich with complex dynamics and diverse mesoscale circulation features in the near-surface and at depth. It is host to a unique, inspiring physical setting that is at the forefront of contemporary oceanographic research [*Sturges et al.,* 2005]. In the last fifty years, physical understanding of the currents in this region has progressed considerably. Gulf of Mexico circulation is clearly important on a global level because of its position in western boundary flow and transport. Studies on its shelves have a wide range of

---

This thesis follows the style of *Journal of Geophysical Research*.

applications as well, as the basin is incident with the critical latitude, and the resonance effect of the inertial and diurnal wind and tidal forcings on currents is a phenomenon of present interest.

The Loop Current, the portion of the Gulf Stream system that connects the Yucatan and Florida Currents, drives the deepwater circulation throughout the Gulf, and therefore has been the focus of many studies in the region [*Sturges and Leben,* 2000]. Recently, an effort has been made to examine the circulation in the Gulf with a series of projects funded by the U.S. Department of the Interior Minerals Management Service (MMS). In 2003, instruments to measure physical parameters were deployed in the deepwater region of the north central Gulf as part of the Exploratory Study of Deepwater Currents in the Gulf of Mexico [*Donohue et al*., 2006]. In 2004, deep currents in the northwest Gulf were observed in the Survey of Deepwater Currents in the Western Gulf of Mexico Study, and in 2005, the deep northeast Gulf was investigated in the Survey of Deepwater Currents in the Eastern Gulf of Mexico Study (EGOM). This research is focused on the dynamics of the eastern Gulf, and thus all analyses in this thesis use the EGOM dataset.

The primary forcing in the Gulf of Mexico is the Loop Current, which is a portion of the Atlantic western boundary current that flows northward through the Yucatan Channel and makes a sharp 90° clockwise turn at approximately 26°N to exit the Gulf at the Florida Straits [*Leben*, 2005]. Altimeter derived sea surface height anomaly on August 5, 2005 is presented in Figure 1. The Loop Current is observed as the red region in the southeast Gulf extending northwest from Cuba with sea surface height anomaly above 30 cm (can range up to 80 cm). The Loop Current position in the eastern Gulf varies with periods on the order of months between a port-to-port regime, i.e., where the current follows almost a direct path between the Yucatan Channel and the Straits of Florida, and an extended position into the northern Gulf [*Chérubin et al.,* 2005; *Coats,* 1992; *Nowlin and McLellan*, 1967; *Cochrane*, 1972; *Hofmann and Worley,* 1986]. Loop Current eddies (the circular feature with high sea surface height in the north central Gulf in Figure 1), which are large-scale anticyclones up to 400 km in

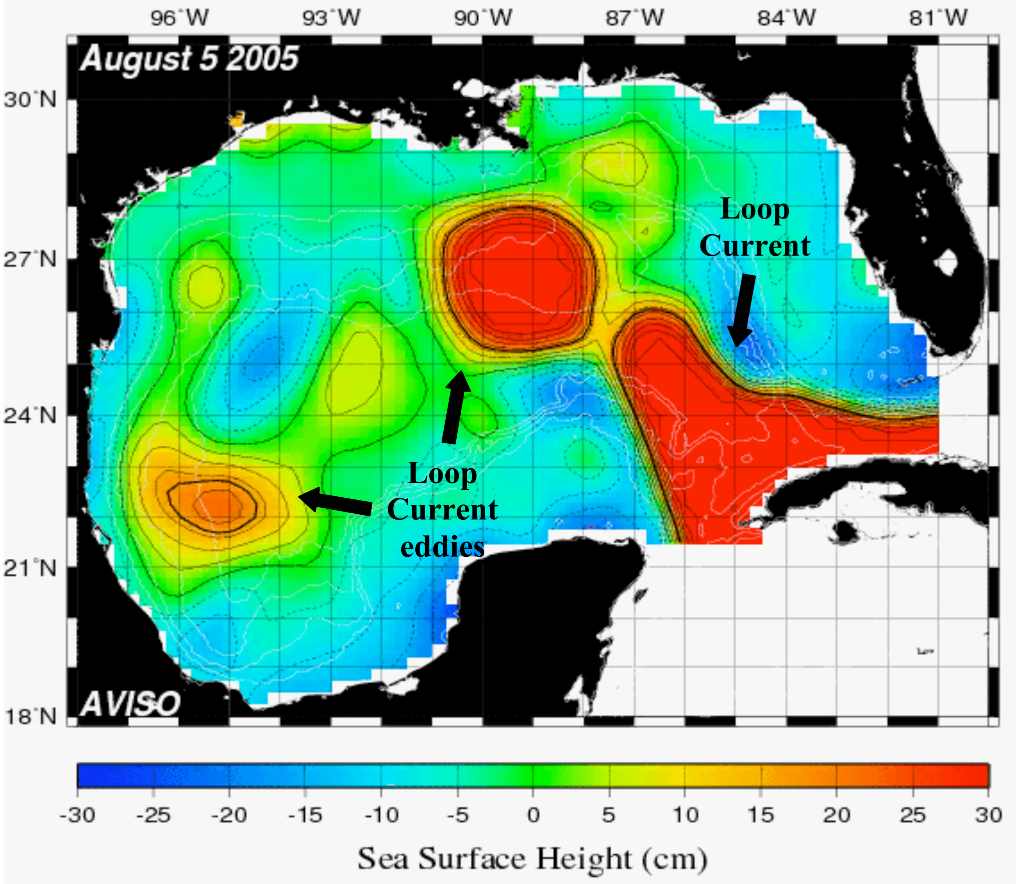

Figure 1. Sea surface height (from R. Leben) in the Gulf of Mexico on August 5, 2005. Contours are 5 cm apart.

diameter, separate from the Loop Current at an average frequency of 11 months and travel westward in the Gulf due to the topographic and planetary beta effects [*Sturges and Leben*, 2000]. These warm core rings have strong current velocities (core speeds up to 2.5 m/s) in the surface layer (depths > 800 m) and demonstrate average translation speeds of 3 - 6 km/day [*Elliot*, 1982; *Hamilton and Lee*, 2005]. Typically, a Loop Current eddy will remain distinguishable for approximately a year, and a large portion of that time is spent decaying near the shelf break in the western Gulf. Some eddies have been observed to interact with the continental slope and move northward impacting circulation on the Texas-Louisiana Shelf, while some eddies lose their energy and dissipate before they reach the western Gulf [*Walker*, 2005; *Lewis and Kirwan*, 1985; *Vidal et al.,* 1992].

1.2 Surface circulation of the Gulf of Mexico

The general surface circulation of the Gulf of Mexico was identified from dynamic height fields by *Dietrich* [1937], in which the Loop Current and the ubiquitous anticyclonic circulation in the western-central Gulf was inferred from very few hydrographic stations [*DiMarco et al*., 2005]. *Ichiye* [1962] first proposed the detachment and westward translation of anticyclonic rings from the Loop Current in the Gulf of Mexico [*Elliott*, 1982]. Since this conjecture was presented, observational studies of the circulation in the eastern Gulf of Mexico, focused on the Loop Current and its associated eddies have been prevalent.

While comparing circulation patterns between summers of 1966 and 1967, *Nowlin and Hubertz* [1972] gave the first account of an anticyclonic ring separated from the Loop Current in the eastern Gulf. They found that the current regimes were distinctly different between the summers of two consecutive years; one summer presented a Loop Current extended far into the northeastern Gulf and the next summer revealed a large detached anticyclone and a Loop Current positioned in the southern portion of the basin. *Cochrane* [1972] reported on the eddy detachment recorded in the same 1967 dataset and determined that cold ridges develop from cyclonic meanders off of the northern Campeche and West Florida Shelves and promote eddy detachment.

Several studies in the Gulf have aimed to quantify the periodicity of the Loop Current's northern penetration and eddy separation. *Maul* [1977] evaluated ocean color sensing satellite data to determine if there was an annual cycle to the currents in the eastern Gulf related to the growth and decay of the Loop Current. He was able to correlate an in-phase relationship between the annual cycle of the extension of the Loop Current into the eastern Gulf and the annual cycle of current speeds and transports of the Gulf Stream, which is in-phase with the annual cycle of trade wind stress [*Fuglister*, 1951]. He also noted that eddy shedding is a vital part of this cycle. *Sturges* [1994], *Vukovich* [1995], and *Sturges and Leben* [2000] have since investigated time scales of separation events based on satellite infrared data and altimetry since 1972, and have found that the shedding cycle is not annual. *Leben* [2005] has given the most complete analysis of the range of shedding periods and has showed it to be from a few weeks up to 18 months using additional satellite data.

Lugo-Fernández [2007] applied a dynamical systems approach to determine if the Loop Current is a chaotic oscillator that demonstrates aperiodic behavior related to transport and vorticity input at the Yucatan channel. He hypothesized that because of its irregular shedding behavior, the Loop Current can be compared to a non-linear, driven, dampened oscillator with an amplitude-dependent period. His study determined that the Loop Current is not a chaotic oscillator, and that the short memory of the current limits forecasting to one cycle in the future, as shedding events are found to be independent of each other.

DiMarco et al. [2005] reports the latest, comprehensive description of the upper ocean circulation from direct velocity estimates in the Gulf of Mexico using 1397 drifters drogued at 50 m between 1989 and 1999. The inflow and outflow of the Loop Current was witnessed in averaged data from all seasons, but only data from winter months revealed a continuous Loop Current. This was attributed to the frequent eddy detachment during other seasons. The spring and fall months presented a central Gulf with significantly variable currents, attributed to the presence of complex eddy systems, and the summer months revealed an energetic Loop Current extended further north than in winter. Furthermore, during the spring and winter, circulation in the eastern and western Gulf is decoupled, i.e., there is not much interaction between the two zones, and during the summer and fall, when eddy shedding is at a maximum, the zones are coupled.

1.3 Loop Current ring shedding

Chérubin et al. [2005] summarized three mechanisms for Loop Current eddy shedding, and hypothesized a combination of all three mechanisms are involved in the shedding process: 1. The ballooning mechanism responsible for the growth of the Loop Current and its northward migration, first described by *Pichevin and Nof* [1997] and *Nof and Pichevin* [2001], states that to conserve momentum, the current balloons northward near its source and forms an anticyclonic bulge followed by the shedding of an a warm core eddy. 2. Cyclonic and anticyclonic circulations beneath the eddy form from the motion of the anticyclone in the upper layer. These deep currents are presented by *Sturges et al*. [1993], *Welsh and Inoue* [2000], and *Cushman-Rosin et al.* [1990]. 3. Baroclinic instability takes place to form a deep modon [*Hurlburt and Thompson*, 1980]. This instability manifests as a deepening and spinning of the base of the Loop Current. The instability-generated cyclone contributes to the separation of the ring but the beta and/or topographic effects remain the control mechanism of the separation [*Chérubin et al.*, 2005]. The dynamical signature of the instability can extend 2000 m, leading to barotropic motion, which has also been observed by *Hamilton* [1990], as well as N. Walker (personal comm.).

Chérubin et al. [2006] used a numerical simulation to study the quasigeostrophic linear and non-linear instability of the Loop Current by modeling a shielded ring, as a vortex with an anticyclonic core, surrounded by a band of cyclonic circulation in the surface layers. A shielded ring is a simple, but reasonable modeling tool for this region, evidenced by *Candela et al.* [2002], who observed a strong potential vorticity anomaly on the western side of Yucatan Current that creates an outer sheared belt around the Loop Current [*Chérubin et al.*, 2005]. Higher, unstable azimuthal modes of the vortex were excited as the width of the cyclonic potential vorticity belt decreased, which increased the horizontal shear. The fourth azimuthal mode of the vortex appeared to be most unstable.

Lewis and Kirwan [1987] studied the evolution of a Loop Current ring using drifters drogued at 100 – 200 m in the Gulf. They hypothesized an alternative means of ring development and separation to the instability theory proposed by *Hurlburt and Thompson* [1980] based on lateral shearing stress the Loop Current encounters off the northwest coast of Cuba. The interaction of the Loop Current with the West Florida Shelf creates negative vorticity in this region because of the direction of the flow in and out of the Gulf. They found an anticyclonic rotational feature, called the Cuban eddy, can form in this region before the previous Loop Current ring is detached, indicating shorter time scales for ring shedding in the Gulf.

1.4 Loop Current frontal eddies

As ring separation has been associated with the steepening of potential vorticity gradients in the eastern Gulf, the importance of cyclonic circulation to the eddy shedding cycle has been evaluated through observations and numerical studies. Cold features observed on the northern edge of the Loop Current travel southward around the west

Florida shelf and form cold tongues or ridges off Dry Tortugas that constrict the northern portion of the Loop, prompting eddy detachment [*Vukovich*, 1986]. Cyclones of 80 – 120 m diameter can form on the eastern side of the Loop and move into the southern Florida Straits, but observations show that they are not advected into the Atlantic [*Vukovich and Maul*, 1985]. *Fratantoni et al.* [1998] hypothesized that these large quasi-stationary cyclonic eddies in the southern Florida Straits, called Tortugas eddies, could be the downstream expression of Loop Current frontal eddies. They used three years of advanced very high-resolution radiometer measurements to show the relationship between the generation of Loop Current rings and the development of Tortugas eddies. Cyclonic frontal eddies on the outer edge of the Loop Current were observed by *Walker et al.* [2003] using GOES-8 high temporal resolution sea surface temperature measurements. They observed four fast-moving frontal eddies travel around the periphery of the Loop Current in May of 1999, which were detected as warm wavelike perturbations. The frontal eddies advect warm water around their centers of circulation but have cold centers below the surface and are usually seen east of the Campeche Bank and grow in diameter as they move clockwise around the Loop Current [*Zavala-Hidalgo et al.*, 2003; *Walker et al.,* 2003].

1.5 Deep flows in the Yucatan Channel

The flow structure and transport of the Yucatan Channel and its influence on the circulation in the Gulf of Mexico has been investigated by *Sheinbaum et al*. [2002].

They found a net transport of ~23 Sv into the Gulf from observations of the channel between September 1999 and June 2000. A somewhat surprising result because it is smaller than the transport out of the Gulf in the Florida current (~30 Sv), and smaller than the transport necessary to close the mass budget of the Caribbean Sea. The reason for this anomaly could be due to transport through smaller passages that were not well monitored and remain less understood, or it could be that summer months were not included in the record. However, it is clear from their study that the dynamics of the circulation in the upper layer of the Gulf is controlled by the deep flow of the channel. Coherency between deep currents in the channel and the rate of change of the surface area of the Loop Current was shown by *Bunge et al*. [2002] based on the same observations.

Using numerical simulations. *Chérubin et al.* [2005] linked the deep transport of the Yucatan Channel to Loop Current ring separation. They found that the outflow into the Caribbean through the channel is in phase with the shift of the Loop Current maximum velocity position and is reflected in transport variations through the channel. *Chérubin et al.* [2005] also affirmed from spectral analysis of Yucatan Channel transport that a dominant period of transport change and the lateral shifting of the Loop Current correspond to the presence of Caribbean eddies in the Yucatan Current.

1.6 The effects of topography on Gulf of Mexico circulation

The steep topography of the West Florida Shelf/Slope contributes to the dynamics of the eastern Gulf of Mexico by affecting the oceanic pressure fields along the shelf break. *Hetland et al.* [2001] employed a series of numerical experiments to investigate the presence of a northward flowing jet just seaward of the West Florida Shelf induced by forcing from the deep ocean (i.e. the Loop Current) and frictional processes on the shelf. They found that the structure and decay of the high-pressure tongue along the shelf break was dependent on the modeling of the West Florida Slope as a wall or a slope, and that this slight difference resulted in a change of the nature of eddy shedding in the Gulf of Mexico. Essentially, when the slope was modeled as a wall, a jet formed and transported mass from the Loop Current, effectively halting eddy shedding, but when the slope was modeled realistically, the jet formed such that mass was leaked onto the shelf to join a southward flow in response to the jet, and possibly return to the Loop Current.

Observations of high-speed deep currents in the northern Gulf of Mexico by *Hamilton* [1990], *Hamilton and Lugo-Fernández* [2001], and *Hamilton* [2007] indicate the presence of low-frequency topographic Rossby waves. At the base of the Sigsbee Escarpment and in the western Gulf, large amplitude wave trains of varying periods (~10 – 25 days) appear and decay over a period of 2 – 3 months. Ray tracing shows the source to be on the western side of an extended Loop Current, and could be caused by the interaction of Loop Current rings with shoaling topography or the ring shedding process itself, as two of the three wave trains observed at the escarpment were concurrent with the shedding and westward passage of anticyclones. *Hamilton* [2007] observed coherent currents at the escarpment, decaying away from the bottom, up to 300 m from the surface in a 2000 m water column; evidence that topographic waves can be nearly full depth. In support of the idea the deep disturbances are linked to the upper layer dynamics associated with the Loop Current, *Hamilton and Lugo-Fernández* [2001] related observed deep currents to the coupling of the upper and lower layers of the water column during the passage of two cyclonic frontal eddies near the mooring site in the central Gulf.

The underlying conclusion of all previous studies in the eastern Gulf is that mesoscale circulation in this region varies rapidly and seemingly aperiodically. The ubiquitous Loop Current, Loop Current eddies, Loop Current frontal eddies, and other cold and warm core eddies reshape the currents on the order of days. This study examines the role of these energetic and highly time fluctuating features on the horizontal current velocity field.

1.7 Partitioning of kinetic energy amongst dynamic modes

Eddy motion is generated in regions with strong mean shear flow, which makes the eastern Gulf of Mexico a prime area to study eddy energy [*Wyrtki et al.*, 1976]. The research presented here is designed to investigate the roles of the Loop Current, Loop Current eddies, Loop Current frontal eddies, and anticyclonic and cyclonic eddies derived therefrom, on the upper and lower layer circulation. These energetic features will be investigated based on an EOF and dynamic normal mode decomposition of the horizontal current velocity time-series. Decomposition into theoretical modes allows the separation of low frequency currents into barotropic and baroclinic components, which represent net transport and current shear respectively [*Inoue*, 1985]. Eddy motion in the eastern Gulf is important to the energy transfer processes related to circulation, and the partition of horizontal velocity components into vertical modes is an effective way to study the vertical partition of kinetic energy [*Wyrtki et al*., 1976]. This research expands the work of *Wunsch* [1997] in the vertical partitioning of oceanic horizontal kinetic energy to three full water column moorings in the eastern Gulf of Mexico.

Dominant vertical EOF modes can often be represented as a superposition of the first few theoretical dynamic modes, and thus it is reasonable to assume that the vertical structure of horizontal quasigeostrophic velocity can be well represented by a linear combination of theoretical modes. *McWilliams and Shen* [1980] have affirmed that mid-ocean mesoscale currents can be represented by a few vertical empirical modes and these modes are similar to theoretical modes for linear quasigeostrophic waves.

EOF analyses on widespread historic current data collected in the Gulf indicate that most current variance is explained by a surface-trapped mode that decays with depth, and higher modes explain a smaller fraction of variance relative to this mode [*Nowlin et al*., 2001]. This surface-intensified mode appears to be an arrangement of the barotropic and first baroclinic modes. The east Gulf has been hypothesized as a potential source region for topographic Rossby waves [*Oey and Lee*, 2002; *Hamilton*, 1990], whose presence would give rise to a bottom-trapped mode explaining a good portion of current variance as well, particularly in areas with sloping bathymetry.

McWilliams and Flierl [1975] hypothesized that the barotropic and first baroclinic components are often correlated rather than independent, as evidenced by the linear relationship of the leading theoretical modes for a flat bottom ocean representative of the first EOF modes. *McWilliams and Shen* [1980] found that the barotropic and first baroclinic modes covary with greatest spatial correlation at lags of approximately an eddy radius. One motivation for this research is to investigate whether this coupling phenomenon is present in the eastern Gulf of Mexico as well.

Wunsch [1997] performed a similar deep ocean investigation in which he partitioned the oceanic kinetic energy into barotropic and baroclinic components using vertically well-resolved current meter moorings and altimeter data. Both the partition of kinetic energy throughout the water column and in the surface layer amongst the buoyancy modes was considered. He showed that in the Gulf Stream region, the barotropic motions are amplified, but the first baroclinic mode is maximum over the mid-Atlantic Ridge. The modal decomposition of the surface kinetic energy, which reflects the motion of the thermocline layer, revealed that globally, the barotropic mode was significantly reduced relative to the first baroclinic mode, with the exception of the Gulf Stream region, where the energy was found to be 40% barotropic. Although Wunsch did not use the same method of mode amplitude computation used here (he used *a priori* assumptions about the fraction of energy amongst the modes instead of a least-squares sense), and fit 5 modes to data in most cases, it is expected that the eastern Gulf of Mexico will yield similar results.

1.8 Scientific questions and hypotheses

The following questions and hypotheses will be assessed in this study:

1. What is the vertical structure and temporal variability of the most energetic dynamic modes? What is the horizontal spatial variability of dynamic modes in the northeast Gulf of Mexico?

Hypothesis 1: *Lower order modes exhibit predominantly low frequency temporal variability and higher order modes exhibit higher frequency variability. Time scales of the dynamic modes increase southward towards mooring M3.*

Most of the current energy in the EGOM study region can be explained in two modes or less, especially given the surface intensified flow that dominates the region, which is strongest at the mooring closest to the Loop Current. Time scales of the modes are hypothesized to increase southward towards mooring M3, as the currents there are exposed to more variability at mesoscale (dimensions on the order of the Rossby radius – around 100 km and time scales of a few months to a year) and longer periods. It is probable that the lower order theoretical modes (barotropic and first baroclinic) will possess low frequency variability on mesoscale eddy and secular (low- frequency mesoscale variability termed by *Schmitz* [1978]) time scales, while higher order modes will exhibit higher frequency variability of an episodic nature. Lower order modes will likely be prevalent throughout the deployment, with the first baroclinic mode amplified when the Loop Current is in the study area. Atmospheric tropical storms might also excite higher order modes in the water column.

2. How do anticyclones and cyclones on the periphery of the Loop Current and the Loop Current itself affect the barotropic and baroclinic mode amplitudes?

Hypothesis 2: *The first baroclinic mode amplitudes will be affected by the surface intensification of the eddy field. The barotropic mode becomes significant in the vicinity of deep eddies. Higher order modes become significant during eddy shedding.*

The first baroclinic mode will be strongest at the region of largest sea surface height gradient, i.e., near the edge of the Loop Current, anticyclones, and cyclones, and not directly in these features. *Chérubin et al.* [2005] noted that Loop Current instabilities that lead to ring detachment could reach 2000 m, leading to barotropic velocities, which might cause considerable variability in the barotropic mode. Also, eddies are surface intensified, but can affect the abyssal circulation as well. Thermal signatures of some rings are seen as deep as 1000 m [*Kuznetsov et al.*, 2002]. Eddies that affect the circulation this deep would alter the barotropic mode amplitude by accelerating mean flow over the water column. Higher order baroclinic modes (modes 2 and up) will most likely become significant during eddy shedding (with a lag since the study region is north of the separation region), as vertical shear plays an important role in the separation instability process.

3. Are temporal amplitudes of lower order modes correlated?

Hypothesis 3: *Barotropic and first baroclinic modes are coupled, while higher order baroclinic modes are not correlated to other modes.*

The barotropic and first baroclinic modes will be coherent at low frequencies during mesoscale processes and obtain the largest correlation at lag distances of approximately an eddy radius, consistent with previous studies by *McWilliams and Shen* [1980].

At present, the ultimate goal of all deep Gulf of Mexico physical research is to make progress in understanding three phenomena: 1.) quantifying processes responsible for Loop Current eddy detachment, 2.) generation, propagation, and dissipation of topographic Rossby waves, and 3.) quantifying the variability of the transport in and out of the Gulf through the Yucatan Channel and Florida Straits. This effort is focused on better understanding the current regime in the eastern Gulf of Mexico, as all of these can be better explained by further study of this region. While all of these phenomena are not directly addressed in this thesis, the results of the research herein will help explain the importance of eastern Gulf circulation to these processes.

In this study, an investigation of the dynamics of the eastern Gulf of Mexico is employed by means of an empirical orthogonal function (EOF) and dynamic mode decomposition of horizontal currents measured from three full water column instrumented mooring arrays. All data used in this analysis, data processing methods, statistics for EOF analysis, and the dynamic mode calculation are explained in the data and methods section (section 2). Results of the analysis are presented in the results section (section 3) and their implications for our understanding of the circulation in the eastern Gulf of Mexico and goals for future research in this region are addressed in the discussion and conclusions section (section 4).

2. DATA AND METHODS

This section summarizes the EGOM mooring and hydrographic studies. Historical hydrographic data, altimetry derived sea surface height, and the gridded wind product used in the analyses in this thesis are presented. EGOM data return and data processing methods for this study are discussed. The theory of empirical orthogonal function (EOF) analysis and dynamic mode decomposition of current velocity is briefly summarized as well as the calculations involved in these methods.

2.1 EGOM mooring study and hydrographic cruises

In January of 2005, three tall moorings, henceforth referred to as M1, M2, and M3 in this text, and one short mooring, M4, were deployed in the eastern Gulf of Mexico by Evans Hamilton Inc. (EHI), an oceanographic services company, aboard the *R/V Pelican*. A summary of moored instruments, parameters measured, sample intervals, and start and stop times, separated by mooring is given in Table 1. A schematic of the mooring M1 instrument array during deployment 1 is presented in Figure 2. The other two tall moorings were configured similarly. M1, M2, and M3 were equipped with one Rowe-Deines Instruments (RDI) Broadband 75 kHz Long-Ranger Acoustic Doppler Current Profiler (ADCP) with 8 meter bin spacing to measure current velocity components in the upper 500 meters of the water column. A string of six S4 and Aanderaa RCM current meters spaced ~ 250 meters apart were used to measure horizontal current velocity of the lower water column, as well as pressure, temperature, and conductivity when available. Moored current meter and ADCP data were recorded hourly. Tall moorings were also outfitted with three Sea-Bird MicroCAT 37SM conductivity-temperature-depth (CTD) sensors at ~ 75 m, ~ 150 m, and ~ 225 m to measure pressure, temperature, and conductivity in the thermocline layer, and four Hugrun temperature sensors positioned ~ 100 m apart in the upper 500 m of the water column. These instruments collected data every 30 minutes, but will not be used in the analyses presented in this thesis.

The short mooring, M4, was instrumented with Aanderaa RCM8 and RCM8s current meters at approximately 2530 m (200 m from the bottom) and 2630 m (100 m from the bottom) depth. These instruments collected hourly velocity data as well.

The instruments were deployed for one year with a servicing and maintenance recovery after seven months. The servicing therefore divides the total deployment into two shorter deployments: D1 and D2. The first deployment, D1, was from January 21, 2005 to August 20, 2005, and the second deployment, D2, was from August 22, 2005 to January 24, 2006. Three hydrographic cruises for this project took place in the study area, during which numerous Sea-Bird SBE 9 CTD and XBT casts took place. CTD casts were averaged into half-meter bins during post-collection processing. Vertical profiles of temperature from the XBT casts were spaced approximately 0.6 meters apart. The first cruise, HC1, occurred January 19 – 23, 2005, during the mooring deployment, the second cruise, HC2, occurred August 19 – 25, 2005, during the servicing and maintenance of the moorings, and the last cruise, HC3, occurred January 21 – 28, 2006, during the mooring recovery. Detailed analysis of CTD data is used in this thesis as the basis for the modal analysis described in section 2.6.

2.2 Historical hydrography, wind, and sea surface height data

This research is based on ADCP and current meter velocity data from M1, M2, and M3 from both deployments and CTD cast data from HC1, HC2, and HC3 at each of the mooring sites, as well as CTD, XBT, and Nansen and Niskin bottle data analyzed in the MMS Deepwater Physical Oceanography Reanalysis and Synthesis of Historical Data (DW) Report [*Nowlin et al.,* 2001]. These historic data include all good quality hydrographic data collected in the Gulf of Mexico since the early 1900s. Approximately 280 historic datasets from the eastern Gulf of Mexico (east of 89°W) are included in the analyses in this thesis.

Sea surface height (SSH) anomaly is obtained from Jason, TOPEX/Poseidon (T/P), Geosat Follow-On(GFO), ERS-2 and Envisat altimeter data processed by the Colorado Center for Astrodynamics Research (data courtesy of R. Leben). SSH data ranging from January 1, 2005 to January 31, 2006 were interpolated to a Gulf-wide grid of quarter-degree resolution and averaged to daily values. Wind velocity data for the full years of 2005 and 2006 is provided by the National Centers for Environmental Prediction (NCEP) at the nearest Eta grid point to each mooring at 3-hour intervals.

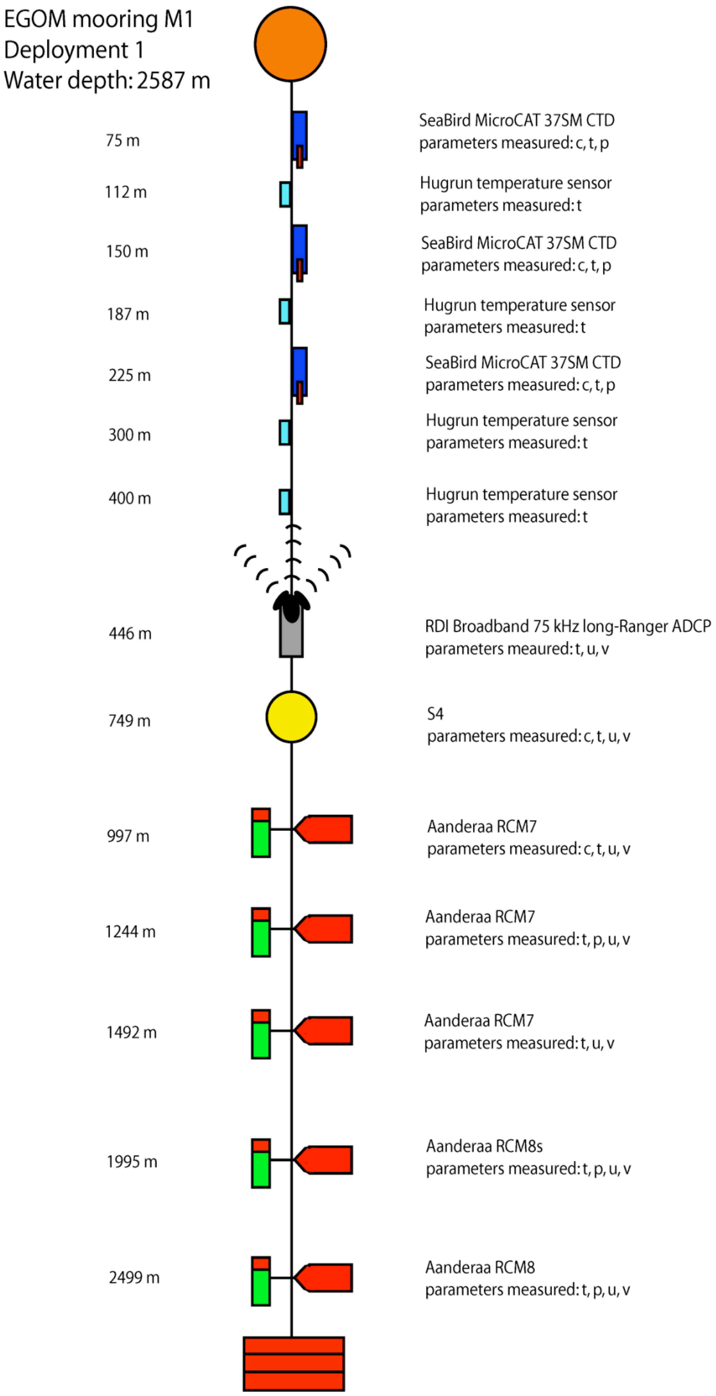

Figure 2. Schematic diagram of MMS Eastern Gulf of Mexico Circulation Study mooring M1 configuration during deployment 1.

Table 1. MMS Eastern Gulf of Mexico Circulation Study mooring instruments (based on information provided by EHI). Columns give parameters measured, sample intervals, start times, and stop times. Deployment 1 and deployment 2 information are separated by a slash as such: deployment1/deployment2.

mooring	depth	instrument	serial number	measured parameters	sampling interval (hr:min:sec)	deployment 1 start time (mo.day.yr hr:min)	deployment 1 stop time (mo.day.yr hr:min)	deployment 2 start time (mo.day.yr hr:min)	deployment 2 stop time (mo.day.yr hr:min)
M1 total water depth: 2587m/2600m	75m	SeaBird	59	c,t,p	0:30:00	1.21.05 22:00	8.20.05 13:00	8.22.05 2:00	1.24.06 13:00
	112m	Hugrun	c919	t	0:30:00	1.21.05 22:00	8.20.05 13:00	8.22.05 2:00	1.24.06 13:00
	150m	SeaBird	2697	c,t,p	0:30:00	1.21.05 22:00	8.20.05 13:00	8.22.05 2:00	1.24.06 13:00
	187m	Hugrun	c926	t	0:30:00	1.21.05 22:00	8.20.05 13:00	8.22.05 2:00	1.24.06 13:00
	225m	SeaBird	2698	c,t,p	0:30:00	1.21.05 22:00	8.20.05 13:00	8.22.05 2:00	1.24.06 13:00
	300m	Hugrun	c932	t	0:30:00	1.21.05 22:00	8.20.05 13:00	8.22.05 2:00	1.24.06 13:00
	400m	Hugrun	c933	t	0:30:00	1.21.05 22:00	8.20.05 13:00	8.22.05 2:00	1.24.06 13:00
	446m/509m	ADCP	4487	t,u,v	1:00:00	1.21.05 21:00	8.20.05 13:00	8.22.05 1:00	1.24.06 12:00
	749m	S4	7801745	c,t,u,v	1:00:00	1.21.05 22:00	8.20.05 13:00	8.22.05 2:00	1.24.06 13:00
	997m	Aanderaa	7223/12805	c,t,u,v	1:00:00	1.21.05 21:59	8.20.05 12:57	8.22.05 1:59	1.24.06 13:00
	1244m	Aanderaa	7692	t,p,u,v	1:00:00	1.21.05 21:59	8.20.05 12:59	8.22.05 1:59	1.24.06 12:59
	1492m	Aanderaa	9722	t,u,v	1:00:00	1.21.05 21:59	8.20.05 12:59	8.22.05 1:59	1.24.06 12:59
	1995m	Aanderaa	10053	t,p,u,v	1:00:00	1.21.05 21:59	8.20.05 12:55	8.22.05 1:59	1.24.06 12:56
	2499m	Aanderaa	12085	t,p,u,v	1:00:00	1.21.05 21:59	8.20.05 12:54	8.22.05 1:40	1.24.06 12:35
M2 total water depth: 2559m/2570m	75m	SeaBird	57/2693	c,t,p	0:30:00	1.20.05 22:00	5.1.05 8:30	8.25.05 17:00	1.23.06 18:00
	112m	Hugrun	c937	t	0:30:00	1.20.05 22:00	5.1.05 8:30	8.25.05 17:00	1.23.06 18:00
	150m	SeaBird	2699	c,t,p	0:30:00	1.20.05 22:00	8.24.05 11:00	8.25.05 17:00	1.23.06 18:00
	187m	Hugrun	c939	t	0:30:00	1.20.05 22:00	5.1.05 8:30	8.25.05 17:00	1.23.06 18:00
	225m	SeaBird	2700	c,t,p	0:30:00	1.20.05 22:00	8.24.05 11:00	8.25.05 17:00	1.23.06 18:00
	300m	Hugrun	c940	t	0:30:00	1.20.05 22:00	5.1.05 8:30	8.25.05 17:00	1.23.06 18:00
	400m	Hugrun	c944	t	0:30:00	1.20.05 22:00	5.1.05 8:30	8.25.05 17:00	1.23.06 18:00
	435m/520m	ADCP	5165	t,u,v	1:00:00	1.20.05 21:00	8.24.05 10:00	8.25.05 17:00	1.23.06 18:00
	749m	S4	8161753	c,t,u,v	1:00:00	1.20.05 22:00	8.24.05 11:00	8.25.05 17:00	1.23.06 18:00
	997m	Aanderaa	7507	c,t,u,v	1:00:00	1.20.05 21:59	8.24.05 10:59	8.25.05 16:59	1.23.06 17:59
	1244m	Aanderaa	7771	t,p,u,v	1:00:00	1.20.05 22:00	8.24.05 10:59	8.25.05 16:59	1.23.06 17:59
	1492m	Aanderaa	12803	t,u,v	1:00:00	1.20.05 22:00	8.24.05 11:02	8.25.05 16:59	1.23.06 18:01
	1995m	Aanderaa	9807	t,p,u,v	1:00:00	1.20.05 21:59	8.24.05 10:57	8.25.05 16:59	1.23.06 17:58
	2499m	Aanderaa	12807	t,u,v	1:00:00	1.20.05 21:59	8.24.05 10:57	8.25.05 16:59	1.23.06 17:58
M3 total water depth: 2815m/2812m	76m	SeaBird	2701	c,t,p	0:30:00	1.20.05 0:00	8.22.05 11:00	8.23.05 19:00	1.24.06 19:00
	113m	Hugrun	c946	t	0:30:00	1.20.05 0:00	8.22.05 11:00	8.23.05 19:00	1.24.06 19:00
	151m	SeaBird	2702	c,t,p	0:30:00	1.20.05 0:00	8.22.05 11:00	8.23.05 19:00	1.24.06 19:00
	188m	Hugrun	c950	t	0:30:00	1.20.05 0:00	8.22.05 11:00	8.23.05 19:00	1.24.06 19:00
	226m	SeaBird	2703	c,t,p	0:30:00	1.20.05 0:00	8.22.05 11:00	8.23.05 19:00	1.24.06 19:00
	301m	Hugrun	c959	t	0:30:00	1.20.05 0:00	8.22.05 11:00	8.23.05 19:00	1.24.06 19:00
	401m	Hugrun	c960	t	0:30:00	1.20.05 0:00	8.22.05 11:00	8.23.05 19:00	1.24.06 19:00
	479m/487m	ADCP	5699	t,u,v	1:00:00	1.19.05 23:00	8.22.05 11:00	8.23.05 18:00	1.24.06 19:00
	750m	S4	2129	c,t,u,v	1:00:00	1.20.05 0:00	8.22.05 11:00	8.23.05 19:00	1.24.06 19:00
	998m/997m	Aanderaa	12084	c,t,u,v	1:00:00	1.19.05 23:59	8.22.05 10:58	8.23.05 18:59	1.24.06 18:58
	1245m	Aanderaa	10643	t,p,u,v	1:00:00	1.19.05 23:59	8.22.05 10:57	8.23.05 18:59	1.24.06 18:57
	1492m	Aanderaa	9480	c,u,v	1:00:00	1.19.05 23:59	8.22.05 10:57	8.23.05 18:59	1.24.06 18:58
	1996m	Aanderaa	9809	t,p,u,v	1:00:00	1.19.05 23:59	8.22.05 10:59	8.23.05 19:00	1.24.06 19:00
	2499m	Aanderaa	12808	t,u,v	1:00:00	1.20.05 0:00	8.22.05 11:01	8.23.05 19:00	1.24.06 19:01
	2699m	Aanderaa	12809	t,u,v	1:00:00	1.20.05 0:00	8.22.05 11:02	8.23.05 19:00	1.24.06 19:01
M4 total water depth: 2726m/2731m	2530m	Aanderaa	10112	t,p,u,v	1:00:00	1.19.05 2:59	8.19.05 12:56	8.19.05 23:00	1.23.06 15:57
	2630m	Aanderaa	12810	t,u,v	1:00:00	1.19.05 3:00	8.19.05 13:01	8.19.05 23:00	1.23.06 16:00

2.3 EGOM data

The moorings of the EGOM study are depicted in Figure 3 by pink triangles; blue dots indicate stations in the eastern Gulf (east of 89°W) where CTD, XBT, and bottle data were collected on various cruises between 1915 and 2000, and evaluated in the DW Report [*Nowlin et al.,* 2001]. A typical position of the Loop Current (estimated from sea surface height fields from the Gulf of Mexico in January 2005) is delineated by the orange line. The inertial period in this region is close to one day: 0.9496 cpd at mooring M1, 0.9389 cpd at mooring M2, and 0.9268 cpd at mooring M3. Also note that the eastern Gulf is bordered by two broad, shallow shelves, with steep escarpments: the West Florida Shelf and the Campeche Shelf, north of the Yucatan Peninsula [*Maul,* 1977]. The EGOM moorings were deployed in approximately 2700 m of water, in a flat-bottomed region, with M3 nearest to the Loop Current, and M1 closest to the steep Florida Slope.

EHI was responsible for initial data quality control and processing. Generally, current velocity data for the mooring study was good. Suspect and bad data were flagged and excluded from further analysis. During the first deployment, the ADCP on M2 suffered interference from the mooring cable after the surface flotation was lost. This resulted in some low, atypical velocity measurements and these data were excluded from the analysis. The Aanderaa RCM7 and Aanderaa RCM8 current meter rotors stall at 1.1 cm/s, and the Aanderaa RCM8s stalls at 1.5 cm/s, thus below these thresholds,

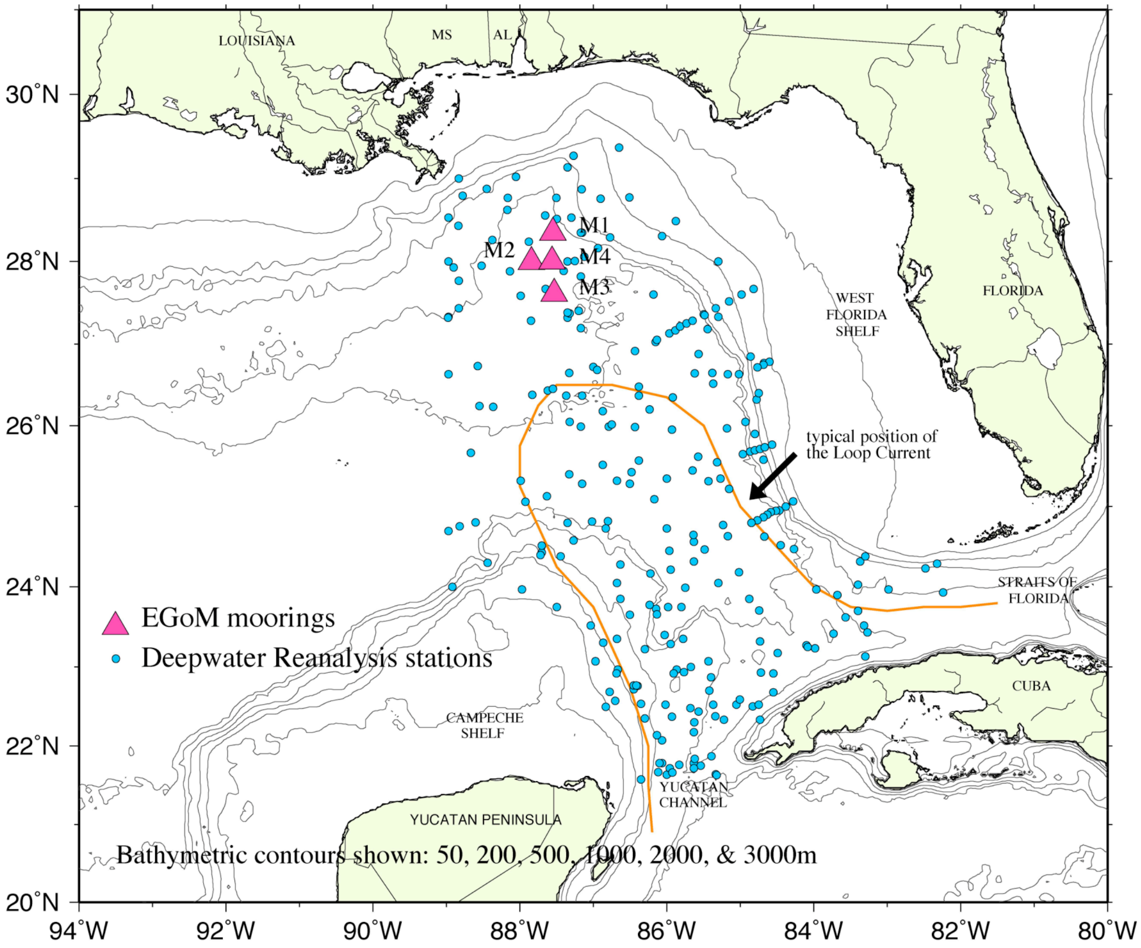

Figure 3. MMS Eastern Gulf of Mexico Circulation Study site and MMS Deepwater Physical Oceanography Reanalysis and Synthesis of Historical Data stations in the eastern Gulf of Mexico (east of 89°W). Triangles represent the EGOM mooring locations, blue dots indicate the Deepwater Reanalysis (DW) sites. The orange line signifies the nominal position of the Loop Current.

velocity is recorded as zero. There were three cases of current meter rotors being lost, but direction was unaffected.

Figure 4 shows the temperature-salinity (T-S) relationship of the hydrographic data collected from years 1915 – 2000 analyzed in the DW report and CTD data from all three EGOM cruises at each of the tall mooring sites. The temperature-salinity relations characteristic of Caribbean near surface water (Subtropical Underwater, or SUW, characterized by salinity > 36.5 at ~22.5 °C) and Gulf Common Water (salinity of ~36.4

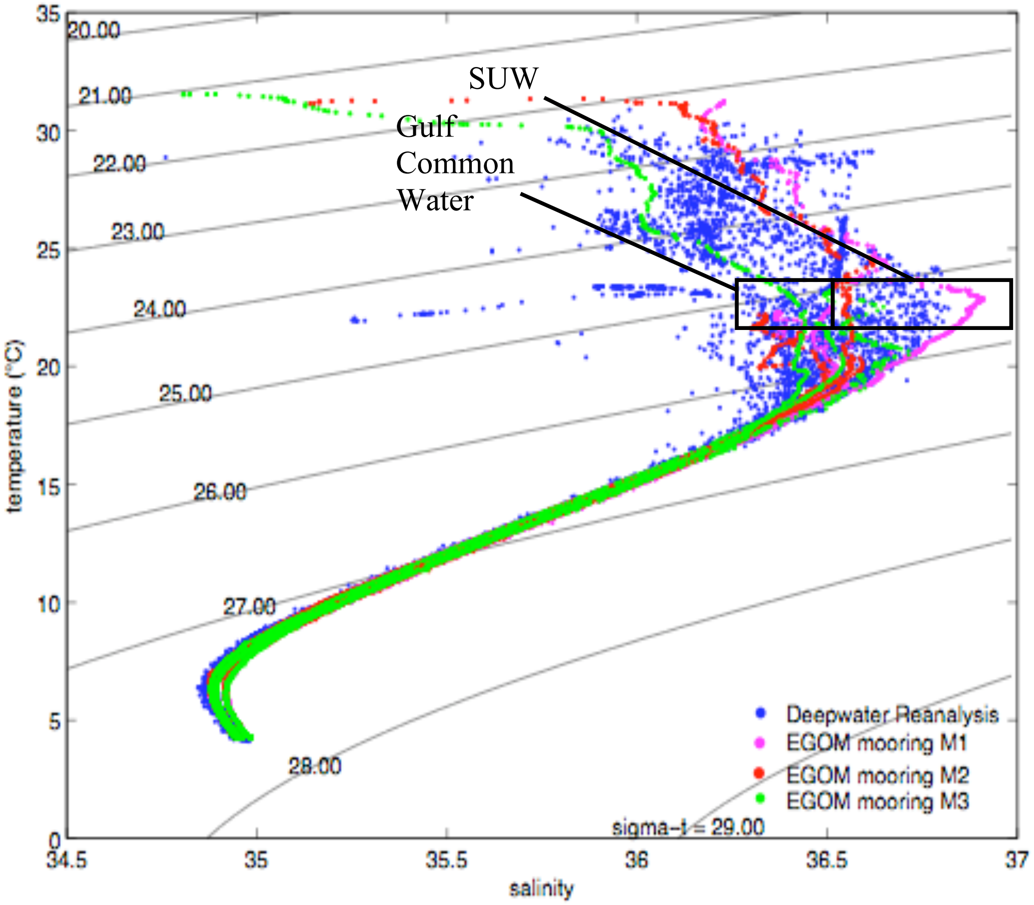

Figure 4. Temperature-salinity relations in the Eastern Gulf of Mexico. Temperature versus salinity from MMS Eastern Gulf of Mexico Circulation Study CTD casts (red, pink, and green dots) and MMS Deepwater Physical Oceanography Reanalysis and Synthesis of Historical Data casts (blue dots) in the eastern Gulf of Mexico (east of 89°W). Contours are of density (sigma-theta).

at 22 – 23.3 °C) at 0 – 250 m depth are clearly identified [*Morrison and Nowlin*, 1982; *Morrison et al.,* 1983]. Typically, the T-S relationship in the upper ocean (at densities above sigma-theta of ~27) is scattered, while in the deep ocean there is very little variance in the T-S relationship. At depth there is a discrepancy between the EGOMcast data and the DW data, as the deep salinity and temperature data for the different projects are not incident with each other. This is likely a calibration problem, and will have very little affect the analyses herein.

2.4 Data processing

During the spring and summer of 2005, there were at least three separation and three reattachment events of the northern lobe of the Loop Current, which culminated in the permanent detachment of Eddy Vortex in September 2005. The passage of the northern extension of the Loop Current and the nascent anticyclone over the study area caused the portion of the mooring above 500 m to become drawn down in the water column; a result of the convergence of water in these features. Mooring draw down caused the instruments on the upper portion of the mooring to record at varying depths. Depth displacements of the instruments ranged up to 50 m at times, especially during spring, when the Loop Current was at its maximum penetration into the northeast Gulf.

Prior to analysis of the ADCP current data, mooring draw down was corrected for by fitting east-west and north-south component time series to a regular grid such that data recorded in an 8 m depth range were assimilated into a single time series. Because the ADCP was originally set to 8 m bins, this method assures there is only one measurement for any sample time. A consequence of this method is gaps in the surface velocity data when the mooring was drawn down, as the uppermost instruments and bins were pushed downward at this time. Gaps over a period of less than 2 weeks and more than 1 day were filled using the spectral Method of Maximum Likelihood, a method which utilizes data before and after the gap to predict values in the gap [*Press et al.,* 1986; *DiMarco et al.*, 1997]. All remaining gaps less than one day were linearly interpolated. The same gap filling procedure was performed on the single point current meter data. Most analyses outlined here require regularly spaced, gapless time series, and due to the gaps caused by the gridding procedure, time series above ~ 60 m were eliminated from further analysis. This also eliminates the portion of the water column that is contaminated by direct Ekman pumping (upper 50 m). For the study of low frequency circulation, all time series were filtered using a 96+1+96 point 40-hour low pass Lanczos-Cosine kernel [*Emery and Thompson*, 2001], which eliminates tidal and inertial signals form the data [*DiMarco et al.*, 1997]. For correlation between sea surface height (SSH) anomaly and current, and wind and current, current data was 40-hour low pass filtered and resampled at 24-hour intervals and 3-hour intervals respectively.

2.5 EOF analysis

Empirical orthogonal function (EOF) analysis, is useful in the interpretation of oceanographic time series because it condenses the variability in a collection of datasets into a countable set of orthogonal modes [*Emery and Thompson*, 2001; *Preisendorfer*, 1988; *Kundu et al.*, 1975]. A linear combination of these modes multiplied by their spatial amplitudes should restore the total variance of a time-series, reconstituting the original data. Stationary patterns in the temporal or spatial domains can be identified as well as propagating features. The objective of EOF analysis, as described by *Emery and Thompson* [2001], is to write a single time series $\psi_m(t)$, $t = 1,2,...,N$, of a collection of M time series ($1 \leq m \leq M$) from different locations in the form:

$$\psi_m(t) = \sum_{i=1}^{M} a_{im}\phi_i(t) \ , \tag{1}$$

where a_{im} is the amplitude of the i^{th} mode at the m^{th} location and $\phi_i(t)$ is the i^{th} principal component (PC) time-series, or mode. Modes are found by casting the data series as a matrix, **D**, and solving the eigensystem:

$$\mathbf{C\Phi} = \lambda\mathbf{\Phi} \ , \tag{2}$$

where $\mathbf{C} = (N-1)^{-1}\,\mathbf{D}\mathbf{D}^{\mathrm{T}}$ is the covariance matrix of the data series, $\mathbf{\Phi}$ is the matrix of eigenvectors, which are the spatial modes, and λ are the eigenvalues, which are equal to the variance of each mode [*Emery and Thompson*, 2001].

2.6 Dynamic mode decomposition

A complete set of linear vertical structure dynamic normal modes, F_n, for $n = 1,2,3,...$, for a flat-bottomed, resting ocean can be evaluated using the Taylor-Goldstein equation:

$$\frac{1}{N^2(z)}\frac{d^2F_n}{dz^2} + \gamma_n{}^2 F_n(z) = 0 \ , \tag{3}$$

where $N(z)$ is the Brunt-Väisälä frequency and γ_n is related to the phase speed of the growing waves of normal modes [*Wunsch*, 1997]. Boundary conditions require $F_n(z) = 0$ for $z = 0,-H$ (surface and bottom). F_n is related to horizontal velocity structure modes, ψ_n, for $n = 1,2,3,...$, by:

$$\psi_n(z) = \frac{\partial F_n}{\partial z}\rho\frac{1}{\gamma_n{}^2} \ , \tag{4}$$

where ρ is the mean water column density; taken to be ~ 1028 kg/m^3 in this analysis.

The second derivative in Equation 3 is cast as a matrix and solved numerically for the eigenvalues and eigenvectors, γ_n^{2} and F_n, respectively.

Horizontal velocity modes can be fit to the moored current data using a least squares multiple regression described by *Inoue* [1982]. The following residual is minimized:

$$\Pi = \sum_{m=1}^{M} [v(z_m,t) - \sum_{n=0}^{N} D_n(t)\psi_n(z_m)]^2 \ , \tag{5}$$

where $v(z_m,t)$ is the observed velocity at depth m and time t, $D_n(t)$ (unknown) is the amplitude of mode n at time t, and $\psi_n(z_m)$ is the n^{th} mode value at depth m. We minimize the error to find the temporal amplitudes of the k^{th} mode by taking the partial derivative with respect to D_k and setting it equal to zero as such:

$$\frac{\partial \Pi}{\partial D_k} = 2\sum_{m=1}^{M} \psi_k(z_m)[v(z_m,t) - \sum_{n=0}^{N} D_n(t)\psi_n(z_m)] = 0 \ , \tag{6}$$

The set of these equations for all modes included in the least squares fit form a square matrix system and D_0, D_1, D_2, … can be solved for at every sample time t using simple inverse methods.

3. RESULTS

This section begins by obtaining an initial impression of the physical processes recorded in the data through examination of the time-series, basic statistics, and spectra of velocity components at various depths in the water column from the EGOM array. Current-wind coherence and current-current coherence is investigated for each velocity component. The vertical structure of low frequency variability is examined through EOF analysis and by a dynamic mode decomposition of the EGOM moored current velocity data, then these two methods are compared. The first baroclinic mode is assessed and related to the sea surface height gradient and spectra and time scales of the first three theoretical modes are evaluated. Next, the kinetic energy in the first three theoretical modes by depth and temporal modal correlation is calculated. Lastly, the results from EGOM data are compared to results from historical data.

3.1 Velocity record length time-series

An initial impression of the nature of the physical processes under examination can be obtained by simple visual inspection of the moored time-series data plotted in composite form at several depths that span the entire water column. Gridded, interpolated current velocity at five ADCP depths and all single point current meters for each mooring deployment at M3 are illustrated in Figure 5 (Figures A-1 and A-2 in Appendix A give velocity time-series at M1 and M2). Tick marks along the y-axis are spaced at 70 cm/s intervals; tick labels indicate record depth. Clearly, currents during both deployments in this region show a high degree of coherency at water depths above 500 m. High-speed current events (near surface speeds exceeding 100 cm/s) are more frequent as observations approach the Loop Current from mooring M1 to M3.

Occasionally, the observations indicate a strong barotropic component to the flow structure. For example, in mid-August 2005, at mooring M3, there is a barotropic event associated with the detachment and reattachment of a eddy Vortex. The feature is coherent throughout the water column, and peaks in the upper ocean with only gradual diminishment with depth. In mid-December 2005, there is a second barotropic current event that is seen in the velocity data collected at M2 and M3. During this second event, the increase in current speed is associated with a Loop Current meander into the study area.

Large-amplitude inertial oscillations excited immediately after the passages of Hurricanes Katrina, in late August 2005, and Rita, late September 2005, are easily identified in the time-series. The current oscillations persist for at least two weeks after the passage of the storms. Inertial motions are strongest at M3 and penetrate down to at least 500 m. Inertial oscillations after the storms are present in the deep ocean as well, but these motions are present throughout deployment and might not be caused by the storms; the phase of these motions would have to be examined to attribute them to the hurricanes. Hurricane Dennis, which entered the Gulf on July 9th, and later passed very close to the study area, is evidenced in the less intense inertial oscillations at M1 around this time. Note also in figure 5, the periods of uncharacteristically linear data collected

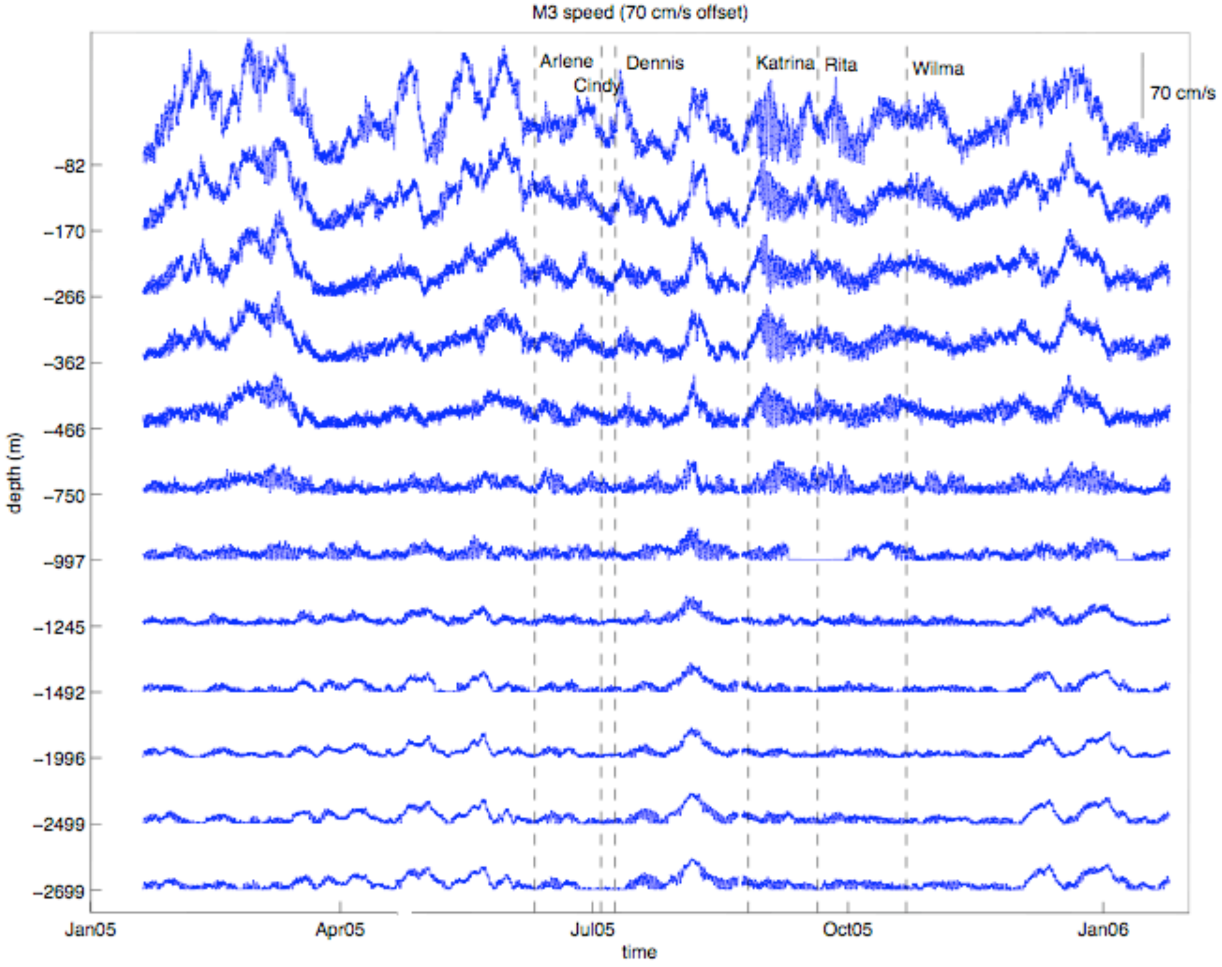

Figure 5. Gap-filled, gridded current speed from five moored ADCP depths and moored current meters for deployments 1 and 2 at mooring M3. Time periods when tropical storms traversed the Gulf are indicated by vertical dotted lines.

at mooring M3 during deployment 2 by the current meter at 997 m, which indicates a malfunction with this instrument.

3.2 Basic statistics

Figure 6 shows vertical profiles of summary statistics of record-length mean, mean plus and minus one standard deviation, minimum, and maximum values for *u* (east-west) and *v* (north-south) velocity components for all instruments and ADCP depth bins on mooring M3 (Figures A-3 and A-4 in appendix A give basic statistics for instruments on M1 and M2). The basic pattern revealed in this series of figures is that current velocity is generally greatest near-surface and decreases with depth. The statistics below depths of 1000 m are typically constant to the bottom. Some of the profiles show that for the uppermost surface velocity bins the record-length mean, standard deviation, and minimum/maximum envelopes tend to have a slightly different character with smaller or slightly shifted statistics compared to measurements at deeper bins, i.e., around 100 m. This may be due to fewer observations associated with surface bins due to instrument drawdown and the effects of gridding the data to non-overlapping depth bins. This effect is particularly relevant since most data dropout at these levels occurs during strong storms or eddy events.

Current velocity at mooring M3 (Figure 6) is predominantly to the southeast during deployment 1 and eastward during deployment 2. This is attributed to the relative location of the mooring to the northern limb of the Loop Current and the developing

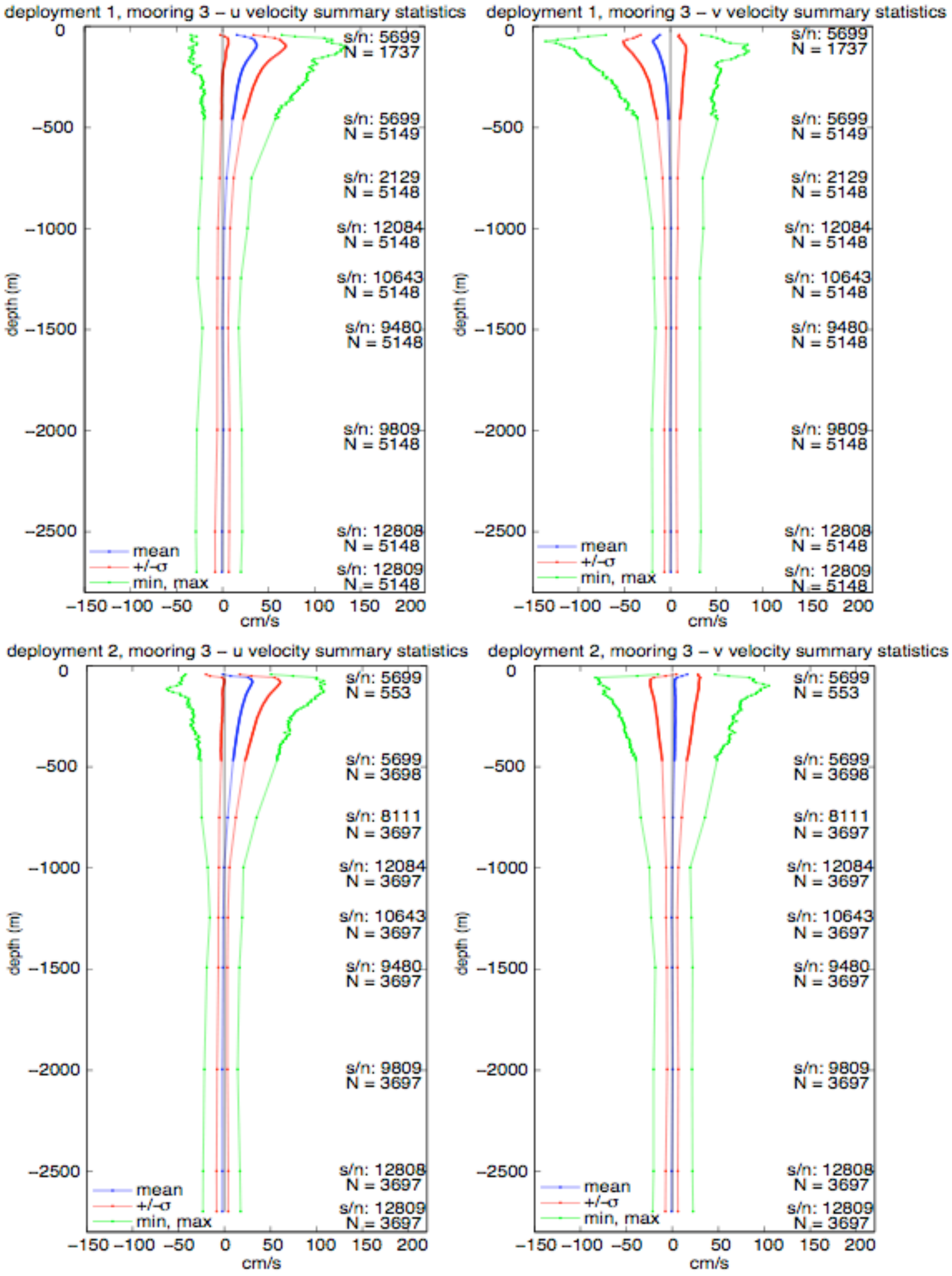
deployment 1, mooring 3 – u velocity summary statistics

deployment 1, mooring 3 – v velocity summary statistics

deployment 2, mooring 3 – u velocity summary statistics

deployment 2, mooring 3 – v velocity summary statistics

Figure 6. Vertical profiles of record-length mean, standard deviation, minimum, and maximum velocity components for mooring M3 (left: east-west component; right: north-south component). Top row: Deployment 1. Bottom row: Deployment 2.

anticyclonic eddy during the early months of 2005. The southern limb of a cyclonic eddy passed over this region during a large period of deployment 2 producing mostly eastward-directed currents. Sea surface height in the Gulf is given in Figure 7, and the cyclone is clearly seen in the study region. The southward velocity at M3 is attributed to the position of the Loop Current relative to the mooring in early April 2005. In May, the northeastern limb of the Loop Current moves into the study area, producing large southward current velocities. During the second deployment, the mean north-south velocity component at M3 is close to zero.

Indications of energetic current events near the ocean surface are present at moorings M1 (Figure A-3) and M2 (Figure A-4) as well. During deployment 1, current velocity is primarily southeastward at mooring M2, and to the east at mooring M1. However, during the second deployment, currents are dominated by various cold core eddies moving in and out of the study area and the result is relatively small mean current velocities.

At mid-water depths, i.e., around 750 m, the magnitude of the minimum and maximum currents for deployment 2 at mooring M1 is a maximum. An examination of the time series show that the large currents associated with this peak occurred in early September 2005 as a long period oscillation with inertial motions superimposed. Comparison with records above and below show little phase-locked or lagged correlation to any one particular event. The timing of these inertial oscillations at this depth are consistent with the interpretation that they were initiated at the surface by Hurricane

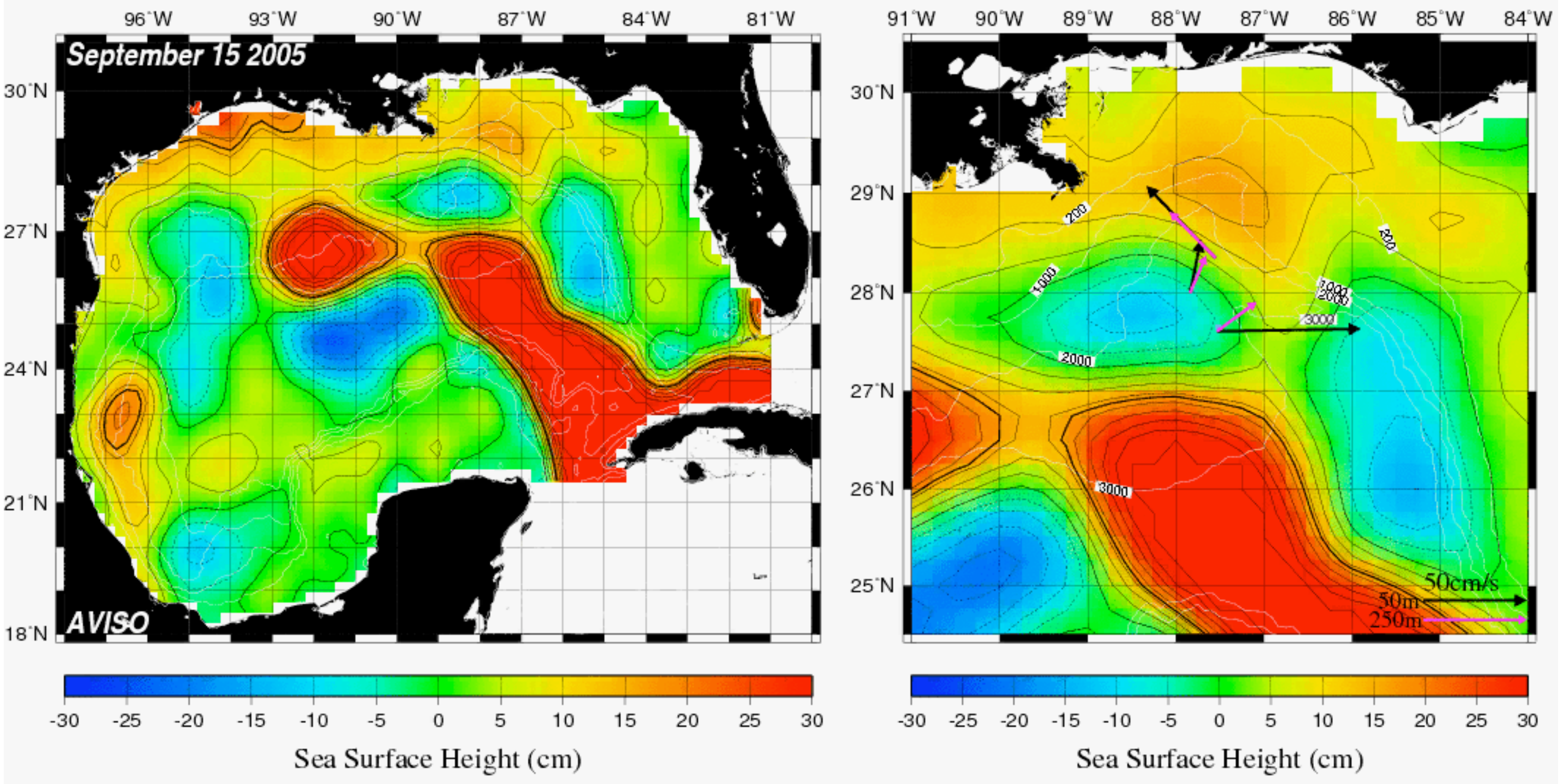

Figure 7. Sea surface height (from R. Leben) in the Gulf of Mexico on September 15, 2005. (Left) Sea surface height over the entire Gulf from several satellites. (Right) Sea surface height in the EGOM study region. Arrows represent velocity at 50 m and 250 m depth at M1, M2, and M3. Contours are 5 cm apart.

Katrina on August 26 and propagated downward in the water column. However, the forcing of the longer period oscillation is not certain. Inertial band energy is seen at these depths at Moorings M2 and M3, however, there are no low-frequency motions and therefore no mid-water peak in basic statistics.

Near-bottom (~2500 m) statistics from deployment 2 at mooring M1 show slightly larger extreme values than values 500 m above bottom. This is the only deployment showing evidence of bottom intensification. We note that at M1 there is no indication of low-frequency oscillations that extend throughout the water column and that bottom motions are not coherent with surface motions.

Basic statistics for M4 are not plotted, however, record-length mean and standard deviation at M4 are near zero for both deployments and are consistent with values at similar depths at other moorings.

Sea surface height is used in some of the analyses within this document, and therefore it is necessary to report basic statistics on those data as well. Mean standard deviation, maximum, and minimum of altimeter derived sea surface height anomaly are presented in Figure A-5 in appendix A. The mean profile of the Gulf shows a Loop Current extended into the north central Gulf, which can be attributed to the Loop Currents extended position during most of the spring and summer; a time of heavy eddy formation and shedding activity. Most importantly, observe that eddy separation introduces the highest sea surface height variance south of the study area, and therefore the currents at mooring M3 are more affected by Loop Current variability than the currents at the other moorings.

3.3 Velocity spectra

Power spectral density profiles for velocity components at all depth levels, for both mooring deployments, were generated using Fast Fourier Transform (FFT) methods. Following Welch's Method, the velocity time series were subsampled into overlapping segments of 512 points. Segments were preconditioned using a 512-point Kaiser-Bessel window; segments overlapped by 50%. The periodogram for each segment was computed using the FFT and then all periodograms for a given record were averaged to produce the spectra shown in this section. A convenient property of the Kaiser-Bessel window is that it allows each 512-segment to be treated as statistically independent. This technique significantly increases the degrees of freedom and, therefore, the statistical confidence of each spectra estimate. If the size of the longest, gapless segment of the time series was less than 512 points, which was the case for some records at the surface, the data were sub-sampled, and a Kaiser-Bessel window the size of the sub-sample was used for preconditioning. As previously stated, records were corrected for mooring draw down, interpolated, and eight tidal constituents were removed using the method of cyclic descent before analysis. Tidal amplitudes were small (~1 cm/s) during this study; common for this region. Spectra (non-variance preserving) estimates for mooring M3 east-west and north-south velocity components are presented at selected depths throughout the water column in loglog form for each deployment in Figure 8 (Figures A-6 and A-7 in appendix A illustrate velocity spectra from M1 and M2). The purpose of these figures is to investigate how the spectral

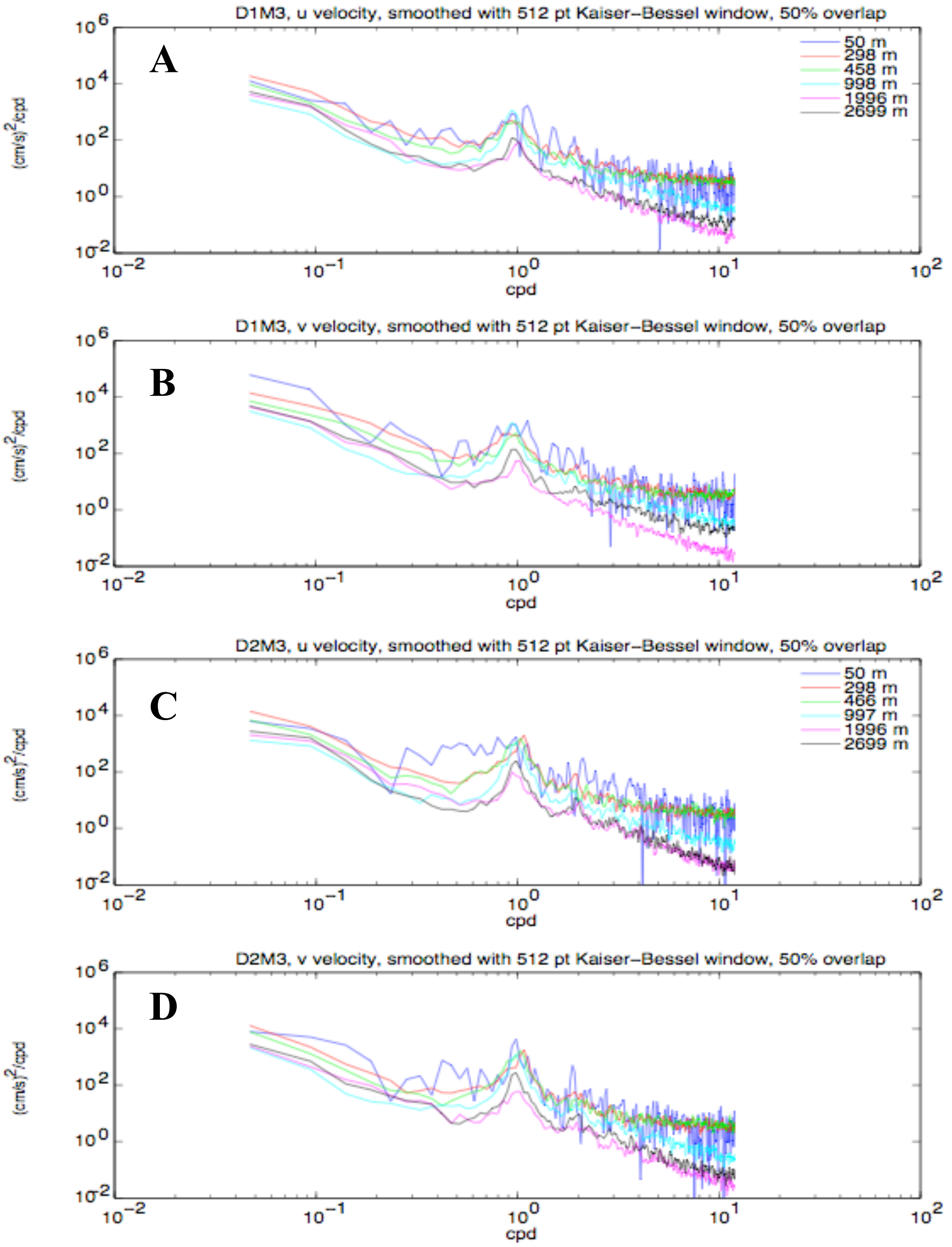

Figure 8. Power spectra at mooring M3. Panels A and B give power spectral density of detided, gap-filled *u* and *v*-velocity respectively at 6 depths at mooring M3 from deployment 1. Panels C and D give power spectral density of *u* and *v*-velocity respectively at 6 depths at mooring M3 from deployment 2.

character of current velocity at each mooring location changes with depth. A typical velocity spectrum derived from a time series from the Gulf of Mexico displays a red energy distribution (weighted to low frequencies), with a distinct peak centered near the inertial frequency (i.e., close to 1 cpd). There is an energy minimum commonly seen in the 3-5 cpd range as well. Near-surface motions having periods ranging from 2-15 days are usually attributable to atmospheric weather conditions. Velocity spectra from the EGOM project support this energy partition.

3.3.1 Upper ocean spectra

In general, spectral energy throughout the frequency domain shown in Figure 8 is greatest in the shallow ocean (< 300 m depth). As expected, surface records (~ 50 m) contain larger weather-band variance than deeper records since the influence of winds on currents generally diminishes with depth. This is especially true at moorings M2 and M3, where the variance steadily increases between 0.9 cpd and 0.1 cpd. Inertial band energy is present throughout the water column, however, the amplitude of the inertial peak tends to narrow and decrease with depth. During the first deployment, the moorings each had similar inertial energy amplitudes. Spectral estimates based on data from the second deployment show moorings M2 and M3 had significantly more energy in the inertial band than mooring M1, owing to the closer proximity of this mooring to the centers of Hurricanes Katrina and Rita.

Near-surface spectral variance associated with periods of ~20 days are typically associated with mesoscale processes such as the Loop Current and it’s eddies. Low-frequency spectral estimates in the upper ocean at moorings M1, M2, and M3, are roughly equal. There is slightly more sub-inertial energy present during deployment 1, especially at the 10 - 20 day period. As this is in the range of an eddy time scale, it is consistent with increased eddy presence observed in other analyses.

The super-inertial domain, i.e., frequencies greater than 1 cpd, generally decreases with increasing frequencies. There is some evidence of semi-diurnal variance, likely associated with residual semi-diurnal tides. However, the variance associated with the semi-diurnal tides rarely rises above background levels.

3.3.2 Deep ocean spectra

Relative to the surface, spectral estimates found in deeper records of the eastern Gulf of Mexico are less energetic. However, the overall shapes of the trends of the spectral estimates of the deeper records closely resemble those estimated from records of the upper ocean. Generally, estimates at super-inertial frequencies tend to decrease faster with increasing frequency in the deeper records. Sub-inertial variability, particularly in the lowest bands shown, decreases from south to north, i.e., from mooring M3 to M1, This may be attributed to the motions associated with the Loop Current and eddy events at each mooring. There are some cases where low frequency variance (10 - 20 day period band) in the deepest record (usually 2500 m) is greater than the energy in the record at ~ 1000 m, which could be evidence of topographic Rossby waves. This is consistent with findings from the DW report, in which it was concluded that there is an energy minimum at ~700 - 1000 m in the Gulf of Mexico due to the sill depth of the Florida Straits.

3.4 Coherency spectra

3.4.1 Current – wind coherence

Coherency, coherence of spectral estimates of independent records, was estimated for all combinations of *u* and *v* wind velocity and *u* and *v* current velocity at all ADCP depths with gapless time-series. In general, no statistical coherency of currents with wind was observed, except for incidental coherency near the inertial frequency. The coherency at this frequency is associated with random phase and are not seen deeper than the shallowest two or three velocity time-series for each mooring. The coherency near the inertial frequency was present at all moorings from data collected during deployment 2. This is likely related to the occurrences of Hurricanes Katrina and Rita, which caused high amplitude inertial currents in the study region for weeks after their passage through the Gulf.

At mooring M1, during deployment 1, there is a weak low frequency correlation between current and wind. The coherency between north-south current velocity and north-south wind velocity shows a significant peak at ~ 20 - 50 day period. The coherency penetrates downward into the water column to 300 m with constant phase. Coherency, phase, admittance, and power spectra for the wind and M1 current north-south velocity records at 100 m during deployment 1 are given in Figure 9. Note that there is no diurnal peak in the wind data.

3.4.2 Vertical current – current coherence

The coherency spectrum was estimated for current velocity components at different depths, i.e., vertically relative to the uppermost time-series at each mooring and

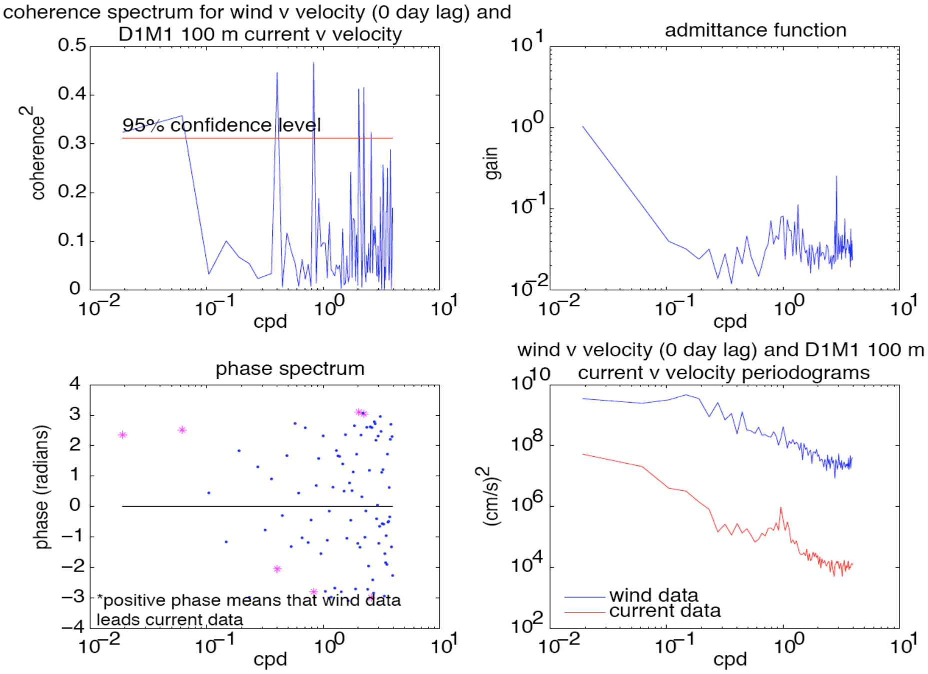

Figure 9. (Clockwise from top left) Coherence, admittance, power, and phase spectra between current and wind *v*-velocity components at 100 m at mooring M1 during deployment 1. Magenta asterisks in the phase spectrum indicate significant coherency at the corresponding frequency.

horizontally between velocity components at similar depths at different moorings. To increase statistical reliability, the coherency spectra were smoothed in the frequency domain over 9 points. Summary plots of significant vertical coherency and horizontal coherency are given in Figures A-8 – A-19 and Figures A-20 – A-25 respectively in appendix A. Phase information is not included in these plots for figure clarity purposes, but is briefly addressed in the following text. Super-inertial coherencies are mostly noisy signals, evidenced by their random phase. Significant coherent current patterns are demonstrated by solid vertical columns of dots penetrating deep into the water column at near and sub-inertial frequencies. These coherent structures are for the most part phase locked (sub-inertial motions) or exhibit propagating phase (near-inertial motions) with depth. It is also interesting to observe the shifting of inertial motions to neighboring frequencies throughout the water column.

The vertical coherence at low frequencies (< 0.5 cpd) between velocity time-series at ~100 m and records to depths of ~500 m were mostly significant for every mooring deployment. Coherency was also observed at near-inertial frequencies. Coherency in the inertial band between near-surface velocity and records between 100 – 200 m diminished owing to the location of the pycnocline at these depths. Below this depth, inertial motions may be attributable to other forcing processes such as eddy features. Inertial oscillations at the surface and at depth therefore would not be expected to be coincident or phase locked. The exception to this is when a powerful hurricane is able to affect layers below the pycnocline.

At mooring M1, deployment 1, there is significant low frequency coherency between current velocity at 100 and 428 m depth at periods above five to six days as evidenced by a comparison of the individual time series (Figure 10). The coherency spectrum (Figure 11, upper left) further indicates significant coherency at the low frequencies (<0.2 cpd). The coherency phase spectrum (Figure 11, lower left) shows the phase between the low frequency components being close to zero indicating in-phase oscillations. The admittance spectrum (Figure 11, upper right) shows the gain between the spectral components of the two series and indicates that the variance in the 428 m record is about 10% of that of the record at 100 m. The admittance at super-inertial

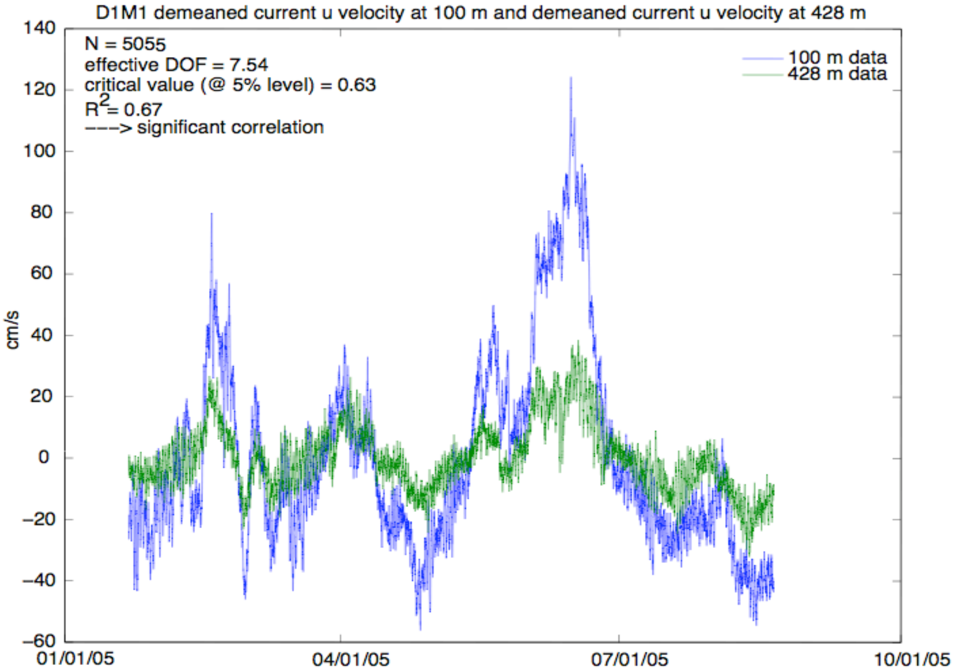

Figure 10. Detided, gap-filled, gridded u-velocity time-series at mooring M1 during deployment 1 at 100 m and 428 m. Strong low frequency in phase coherency indicates significant correlations between currents at these two depths.

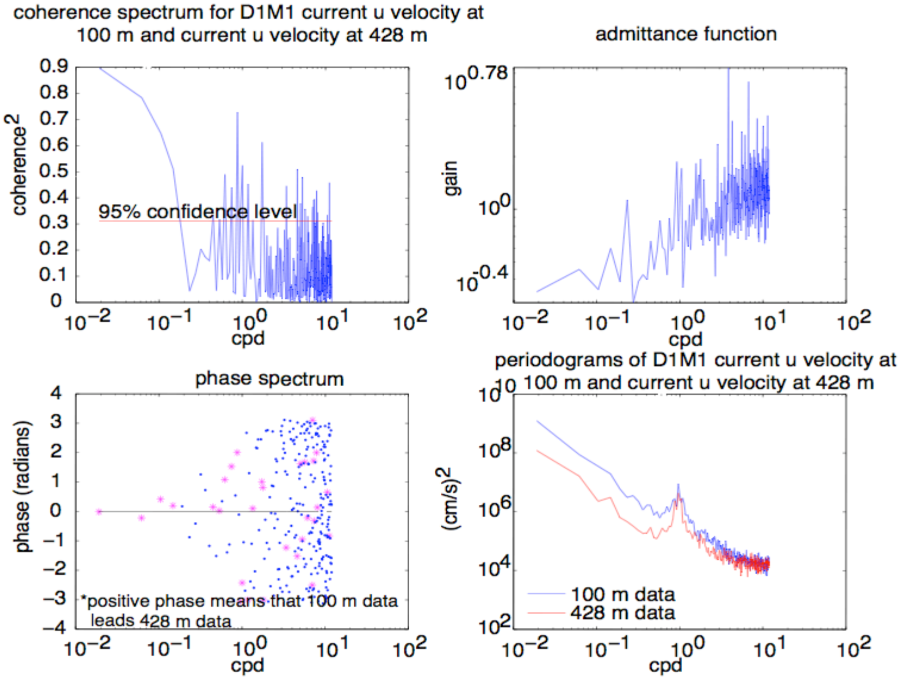

Figure 11. (Clockwise from top left) Coherence, admittance, power, and phase spectra of east-west (*u*) velocity components at 100 m and 428 m at mooring 1 during deployment 1. Magenta asterisks in the phase spectrum indicate significant coherency and phase at the corresponding frequency.

frequencies is close to one, indicating nearly equal variances.

At mooring M2, deployment 1, significant coherency is distributed similar to that seen at mooring M1. In the upper layer, low frequency coherency is seen at periods longer than about eight days and at near inertial peaks. However, this coherency extends deeper than at mooring M1. For example, north-south velocity is coherent with the surface at depths reaching 1244 m and east-west velocity is coherent with surface east-west velocity down to 750 m. For the second deployment, north-south velocity at mooring M2 is coherent throughout the upper water column (to about 500 m depth) at low frequencies with zero phase lag, as seen in Figure 12. This is not the case for the east-west velocity component, as it is only correlated at the lowest frequency estimate (~40 day period). The near-inertial correlation in both velocity components between the surface and at depth diminished around 120 m at mooring M2 during deployment 2.

Vertical coherency at mooring M3 during deployment 1 presents a similar picture to moorings M1 and M2, with significant zero lag low frequency correlation throughout the upper water column (to ~500 m) for east-west velocity component, but only to 350 m for the north-south velocity component. Data at mooring M3 from deployment 2 are

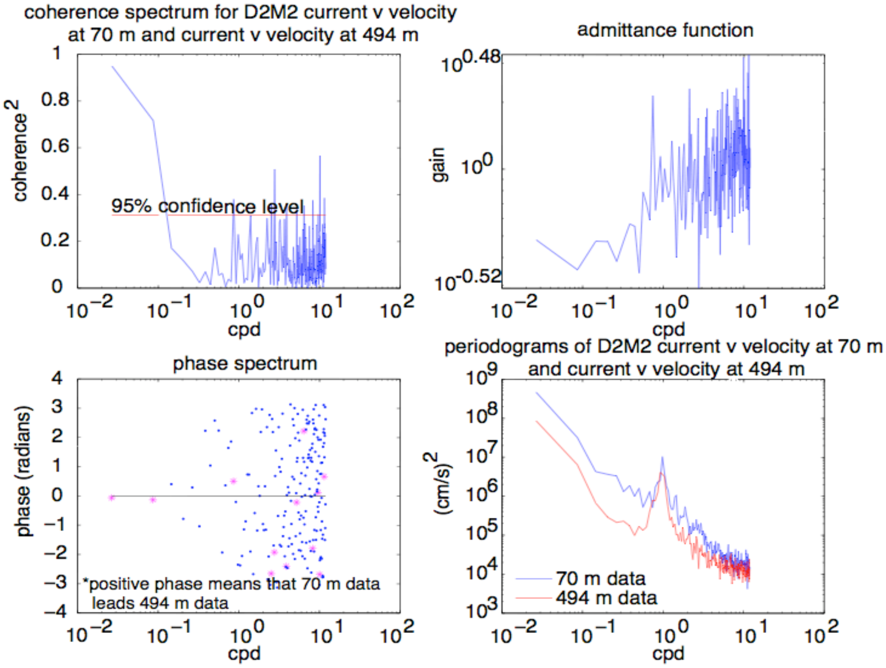

Figure 12. (Clockwise from top left) Coherence, admittance, power, and phase spectra of north-south (*v*) velocity components at 70 m and 494 m at mooring M2 during deployment 2. Magenta asterisks in the phase spectrum indicate significant coherency and phase at the corresponding frequency.

only significantly correlated to 300 m for the east-west velocity component and 100 m for the north-south velocity component.

3.4.3 Horizontal current – current coherence

Estimates of the coherency spectra for horizontal separations were calculated between moorings for all velocity component combinations at the same depth. East-west velocity at moorings M1 and M2 were coherent at the lowest frequency band (~50 day period) and with zero phase lag. Near the inertial frequency in the upper water column, coherency was found at 750 m, 1244 m, and 1492 m. The phase of the correlation at the near inertial peak is variable with depth. The east-west velocity component at mooring M1 and north-south velocity component at mooring M2 are also coherent at low frequencies, but with phase difference of about 1 radian (~90°) at the lowest frequency, which indicates that M1 velocity leads M2 velocity. Coherency between M1 *v*-velocity and M2 *u*-velocity, as well as coherency between *v*-velocity at both moorings indicate coherency at low frequency with phase of ~ -1.0 radian, which means that M2 leads M1. Deeper current meter records, except for the records at 1995 m, are only significantly correlated between north-south velocity components at both moorings in the inertial band and at low frequencies (> 10 day period), as seen in Figure 13. This may be an indication of topographic steering along the bathymetry.

Mooring M1 and mooring M3 east-west velocities are coherent at near-inertial frequencies at every depth in the upper layers. M1 *u*-velocity and M3 *v*-velocity are

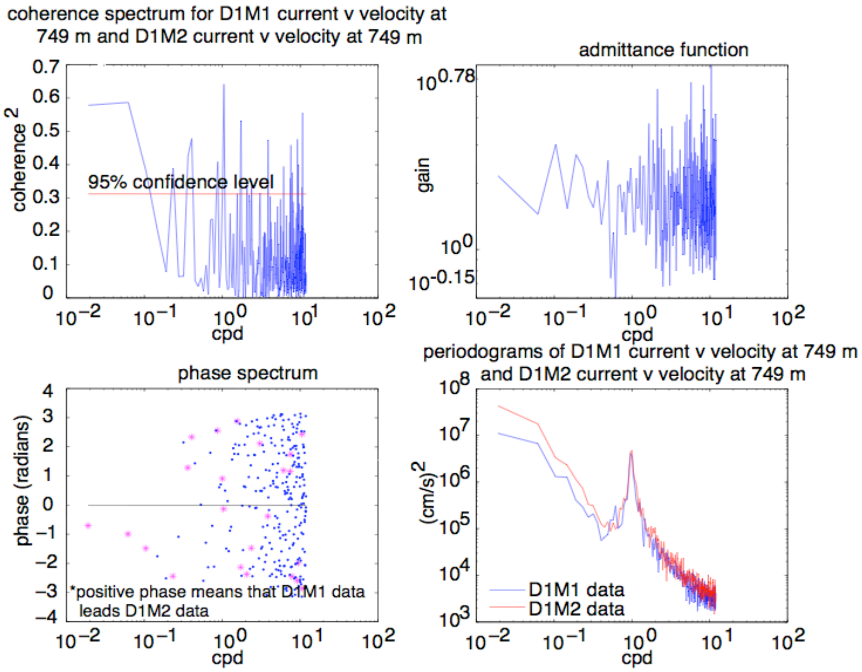

Figure 13. (Clockwise from top left) Coherence, admittance, power, and phase spectra between *v*-velocity components at 749 m at mooring M1 and mooring M2 during deployment 1. Magenta asterisks in the phase spectrum indicate significant coherency at the corresponding frequency.

correlated at the fundamental frequency at a phase of ~2 radians (180°) throughout the water column and near inertial peaks were present down to 998 m. North-south velocity at M1 and M3 were correlated at low frequencies down to 998 m with zero phase difference. Only near-inertial correlation was present between M1 *v*-velocity and M3 *u*-velocity.

East-west velocity at moorings M2 and M3 illustrate very little significant coherency beyond some intermittent near-inertial correlations in the upper water column. However, the east-west velocity was coherent between moorings M2 and M3 in all current meter records in the deep ocean at periods of about 20 days (Figures 14 and 15).

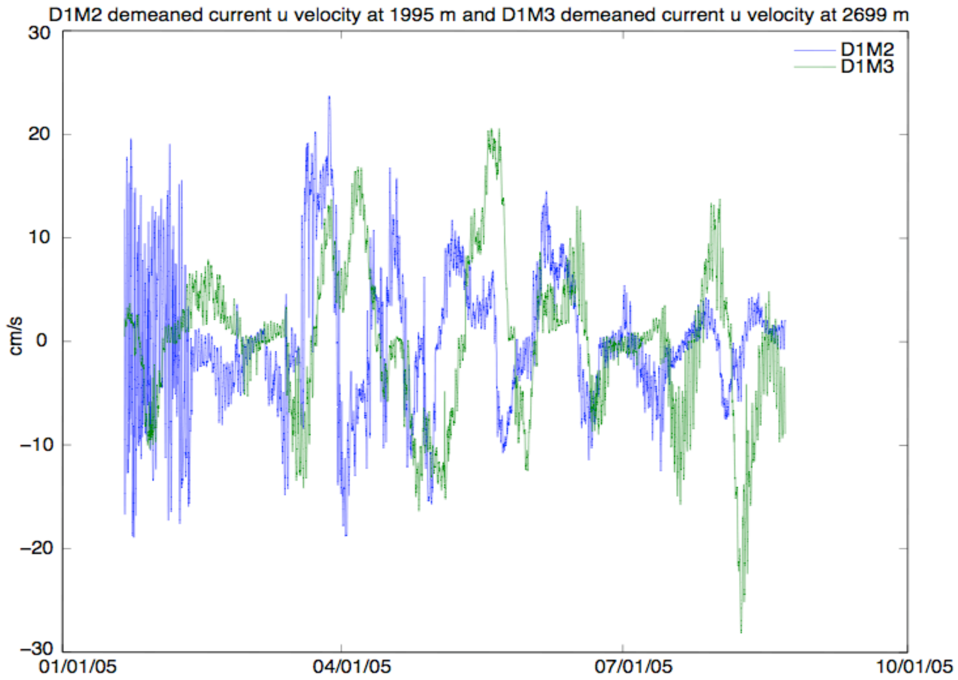

Figure 14. Detided, gap-filled, gridded east-west velocity time-series at mooring M2 and mooring M3 during deployment 1 at 1995 m and 2699 m respectively.

3.5 Vertical structure of low-frequency variability

3.5.1 Empirical orthogonal function (EOF) analysis

Empirical orthogonal function (EOF) analysis, also known as principal component analysis is an accepted tool to quantify patterns of variability in large sets of time-series data that are of sufficient spatial distribution [*Emery and Thomson*, 2001; *Preisendorfer*, 1988]. We employed an EOF analysis to the EGOM current meter data in a manner consistent with previous studies in the Gulf of Mexico [*Nowlin et al.,* 2001]. In those previous studies, mooring locations that had at least 5 depth levels distributed

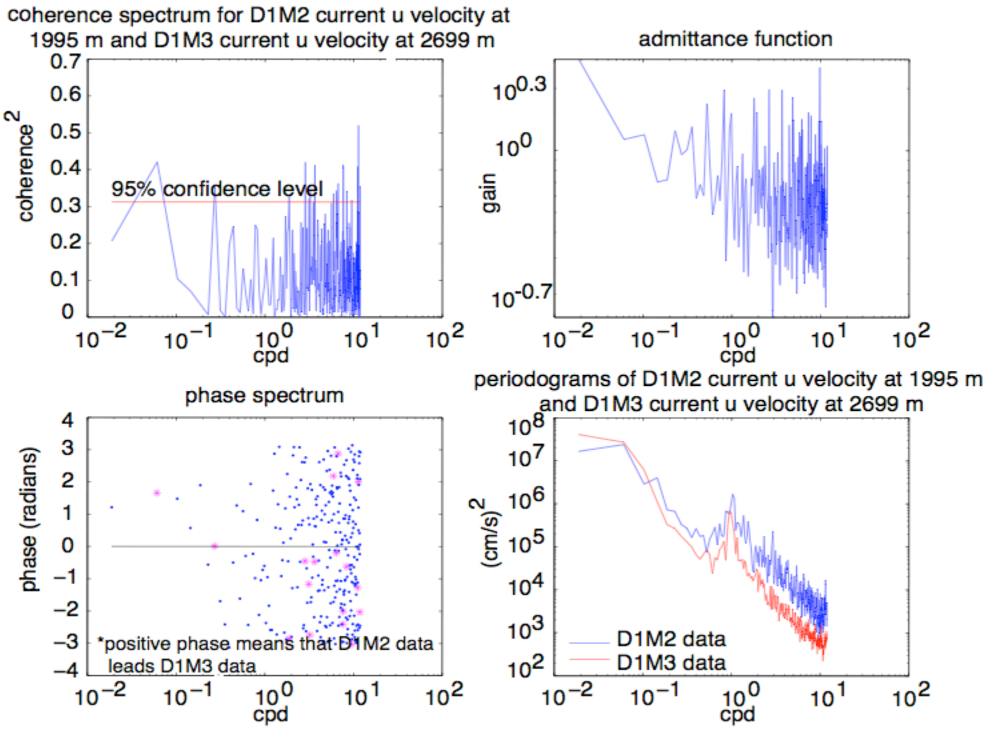

Figure 15. (Clockwise from top left) Coherence, admittance, power, and phase spectra between *u*-velocity components at mooring M2 and mooring M3 during deployment 1 at 1995 m and 2699 m respectively. Magenta asterisks in the phase spectrum indicate significant coherency at the corresponding frequency.

in a manner consistent with previous studies in the Gulf of Mexico [*Nowlin et al.,* 2001]. In those previous studies, mooring locations that had at least 5 depth levels distributed throughout the water column were chosen for analysis. At the time, only one mooring contained high vertical resolution from moored current profilers that were publicly available. EOF analysis was also performed on current output from a three-dimensional general circulation model of the full Gulf of Mexico basin [*Kantha*, 2005]. The general conclusion of the previous studies showed consistent vertical modal structure at several locations across the northern slopes of the Gulf of Mexico. The structure was consistent for course and fine vertically resolved current observations.

Nowlin et al. [2001] found that the first mode, Mode 1, defined as the mode with the greatest percentage of variance, has a surface maximum that decreased exponentially with depth. Mode 2, containing the second largest percentage of variance, is bottom intensified with a zero-crossing or minimum in the upper 500 meters and barotropic (nearly constant) at depth. The interpretation of these previous results concluded that the dynamics of the low-frequency variability of the Gulf of Mexico can be interpreted as a two-layer system; the dynamics of the upper layer associated with the exponentially decaying with depth motions of the Loop Current and Loop Current eddies, and the depth defining the transition to the lower layer being coincident with the sill depth of the Florida Straits. The bottom intensification for this analysis was attributed to the influence of the sloping topography on available normal dynamic modes estimated from stability theory [*Charney and Flierl*, 1981].

It is important to recall, however, that EOF modes are purely statistical constructs and in themselves do not represent physical processes. Therefore, the decomposition of statistically derived EOF modes are typically regressed onto dynamic modes to refine their interpretation and provide physical basis.

The vertical EOF decomposition of east-west and north-south velocity component data was performed at each mooring, for each deployment, using data at approximately 12 depth levels that were distributed though out the water column. Due to computational considerations of computer memory and computing time, data from each gap-filled single point current meter and five depth levels of the ADCP data were used in the calculation. All current data were 40-hr low-passed filtered to remove tidal, inertial, and other high frequency motions.

Figure 16 (EOF of M3 *u* and *v*-velocity during deployment 1) and the sequence of plots shown in Figures A-26 – A-30 in appendix A shows the results of the EOF analyses. These plots affirm that the horizontal current structure in this region of the Gulf resembles a 2-layer system. The eddy field causes intensification of the surface currents, which exponentially decay in magnitude with depth to ~ 800 m. This structure is observed in the Mode 1 amplitudes, which contain the largest percentage of variance (~ 80 - 95 %). This mode shows maximum amplitudes at the surface that decrease with depth to nearly zero below 1000 m. The dynamic effect of eddies are rarely seen below 800 m; the sill depth of the Florida Straits.

The second mode, Mode 2, explains the second largest percentage of variance. In general, the amplitude crosses zero near 200 meters depth and is nearly constant or gradually increasing with increasing depth. During deployment 1, the amplitudes of Mode 2 at mooring M1 shows a mid-water maximum at 300 m and barotropic amplitudes below1000 m. The structure of this mode, however, is more similar to the vertical structure found in Mode 3 at moorings M2 and M3. Furthermore, the percentage of variance in the second and third modes increases from M1 to M3, indicating more variance in the higher order modes closer to the Loop Current. During the second deployment, Mode 2 at mooring M1 again resembles higher order modes at M2 and M3.

The vertical structure of Mode 3 is more complex with two zero crossings

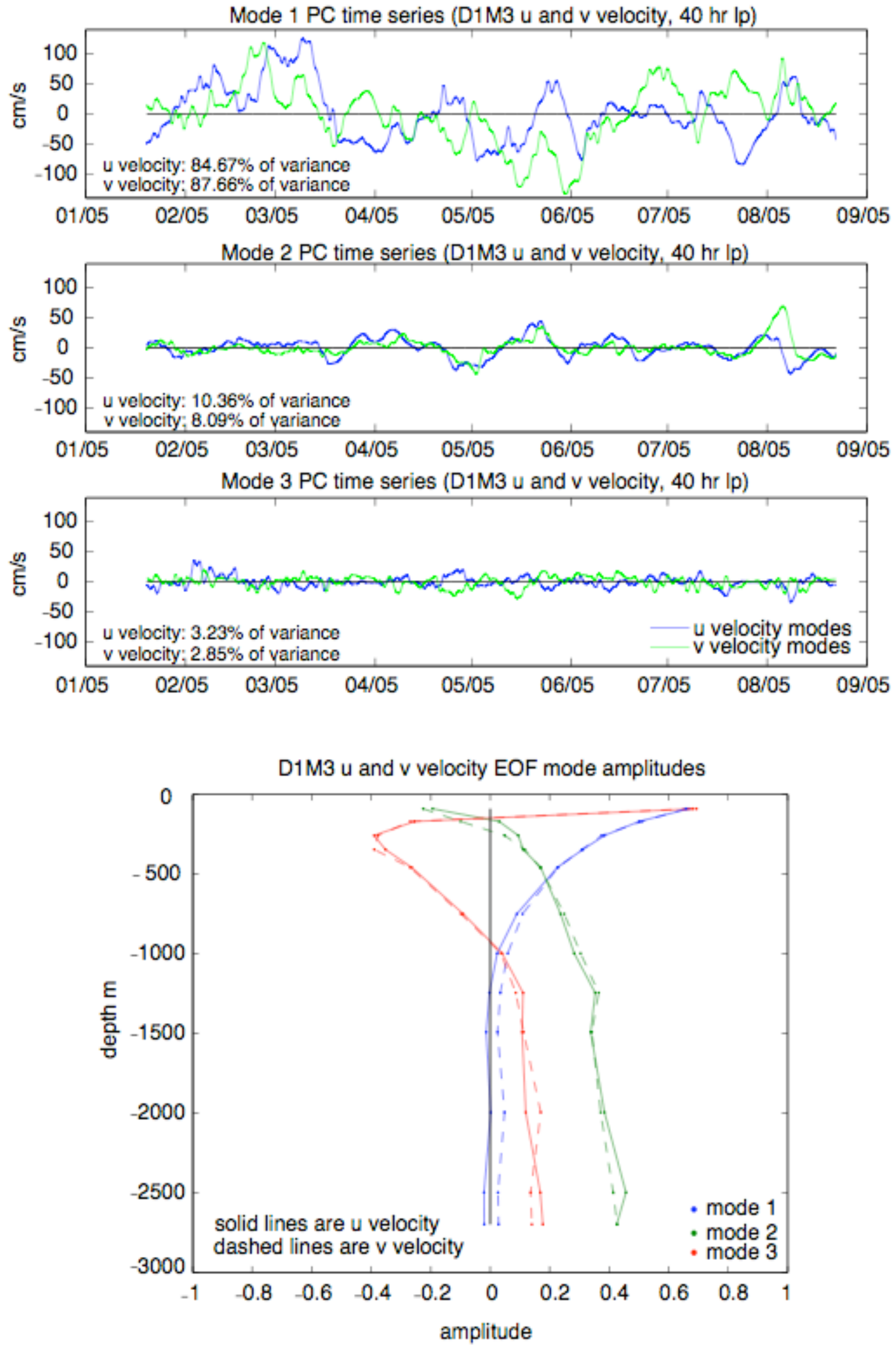

Figure 16. Vertical EOFs of east-west and north-south current velocity at mooring M3 during deployment 1. Top three panels: Principal component (PC) time-series of first three empirical modes. Bottom panel: Amplitudes of empirical modes corresponding to PC time-series.

typically in the upper 1000 m and relatively constant in water depths below 1000. The amount of variance contained in this mode is a small fraction of the current variance (< 4 %). A summary table of the percentage of variance explained by the first three modes for *u* and *v*-velocity EOFs at each mooring is presented in Table 2.

3.5.2 Dynamical mode analysis

The estimation of dynamic modes is motivated by the desire to identify horizontally propagating wave solutions under the Boussinesq approximation for a

Table 2. Percentage of variance in EOF Modes 1, 2, and 3 for moorings M1, M2, and M3 for horizontal velocity components during deployment 1 and deployment 2 (in parentheses).

	Mode 1	Mode 2	Mode3
M1			
u-component	96.51 (88.12)	2.33 (6.38)	0.47 (2.62)
v-component	95.43 (88.37)	2.80 (6.44)	0.72 (2.21)
M2			
u-component	93.53 (79.48)	3.24 (12.77)	1.81 (5.82)
v-component	95.58 (96.06)	2.52 (1.98)	0.86 (1.24)
M3			
u-component	84.67 (88.47)	10.36 (6.83)	3.23 (3.18)
v-component	87.66 (85.96)	8.09 (11.49)	2.85 (1.43)

rotating fluid [*LeBlond and Mysak*, 1978]. The method solves an eigenvalue equation for a prescribed stability profile, *N*(*z*). The resulting vertical eigenfunctions are the allowable structures for that stability. "The eigenfunctions are real, orthogonal with real eigenvalues. The gravest mode is identified as the barotropic mode, and the modes n=1,2,3,… are the sequence of baroclinic modes [*LeBlond and Mysak*, 1978]". The calculations that follow presume a flat ocean bottom. A sloping bottom yields a bottom trapped gravest (barotropic) mode

Stability profiles were derived from temperature and salinity (CTD) data from hyodrographic data collected during the EGOM study. CTD data at mooring locations on HC1, HC2, and HC3 were used to calculate vertical buoyancy modes that represent the mean horizontal current structure at the three mooring locations. Note that the modes were calculated using a discretized version of the Taylor-Goldstein equation for a linear, flat-bottomed ocean [*Klinck,* 2004]. Temporal and spatial means were not removed from the CTD data prior to mode calculation. Although the theoretical modes are based on a resting ocean, neutral modes of an ocean with a surface-intensified mean flow are important for studies of baroclinic instability. The results should vary significantly when mean flow is included in the model, as the modes in this case become dependent on lateral scales of motion [*Gill et al.*, 1974, *Wunsch*, 1997]. The density field in the upper 500 m is vital to the determination of mode structure [*Wunsch*, 1997]. Because hydrographic data was only available from three EGOM cruises at two different times of year in a region where the Loop Current is constantly altering the density field, hydrographic cruise data evaluated in the DW Study [*Nowlin et al.,* 2001] were also analyzed for comparison, and yielded similar results.

Vertical profiles of Brunt-Väisälä frequency (N^2), shown in Figure 17, were found to be maximum between 100 - 200 m during the winter and near surface (< 20 m depth) during the summer. Dynamic modes calculated from CTD casts at (or closest to) the mooring sites during deployment, maintenance, and recovery cruises were used to create an average set of modes to fit to the velocity data collected during mooring deployment. Some features of the N^2 profile might be smeared out because of averaging dynamic modes.

Figure 18 in this section (normalized dynamic modes at M3 from profiles in January 2005 and August 2005) and Figures A-31 – A-35 in appendix A give the first three normalized dynamic modes constructed from the averaged casts at each mooring. The barotropic mode is simply equal to one throughout the water column. First and second baroclinic modes have similar shapes at each mooring. The first mode crosses zero around 600 m; the second mode crosses zero twice, around 200 and 900 m. Below 1200 m all modes are barotropic, i.e., nearly constant with increasing depth. As can be seen, the general shape of these modes is the same for each mooring deployment. The relative amplitudes are nearly identical; the principal difference between casts is the depth of zero-crossing of the modes. Please note that the normalized modes in these figures are not the dynamic modes fit to the observed velocity. The baroclinic modes have much smaller magnitude than the barotropic mode, and normalization was

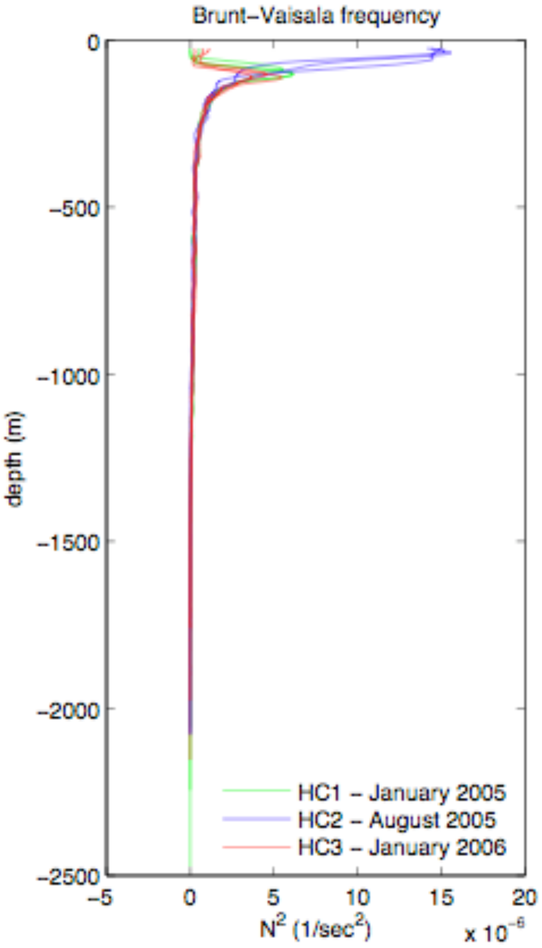

Figure 17. Vertical profiles of Brunt-Väisälä frequency at or nearest to each mooring site. Casts from three EGOM hydrographic cruises in January 2005, August 2005, and January 2006.

performed to put the barotropic and baroclinic components on the same scale, while still maintaining the character of the curves.

The temporal variation of the barotropic and first two baroclinic modes were estimated using a least squares minimization that fits the calculated set of vertical modes to synoptic vertical profiles of the moored ADCP and single-point current meter data. Three modes were used in the least squares fit. The modes were not normalized prior to

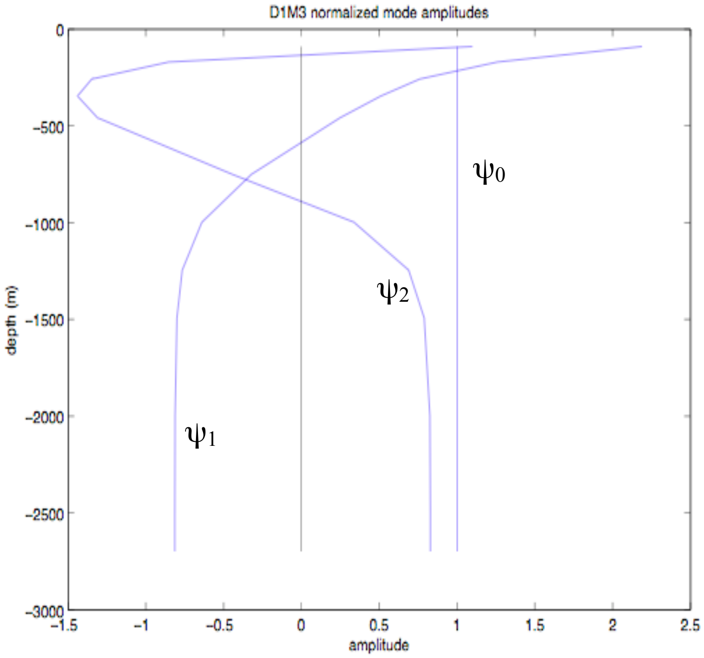

Figure 18. Normalized barotropic and first two baroclinic modes calculated with averaged casts at M3 from cruises in January and August of 2005.

fit. Figures 19 and 20 show a three-panel representation of the results of the least squares fit of the first three dynamic modes to the current profiles at M3. The sequence of Figures A-36 – A-45 in appendix A show the results of the least squares fit of the dynamic modes to velocity components at the other moorings. Each tri-plot corresponds to a single deployment, mooring, and velocity component. The top panel represents the spatial (vertical) correlation of the fit with the observed profile. Correlation of one indicates a perfect fit with no residual error, less than one indicates higher order ($n > 2$) modal variability. The bottom panel shows the time-series of the first three dynamic mode amplitudes resulting from the fitting procedure. The right panel shows the time correlation between the observed and modeled time series at a particular depth. This is

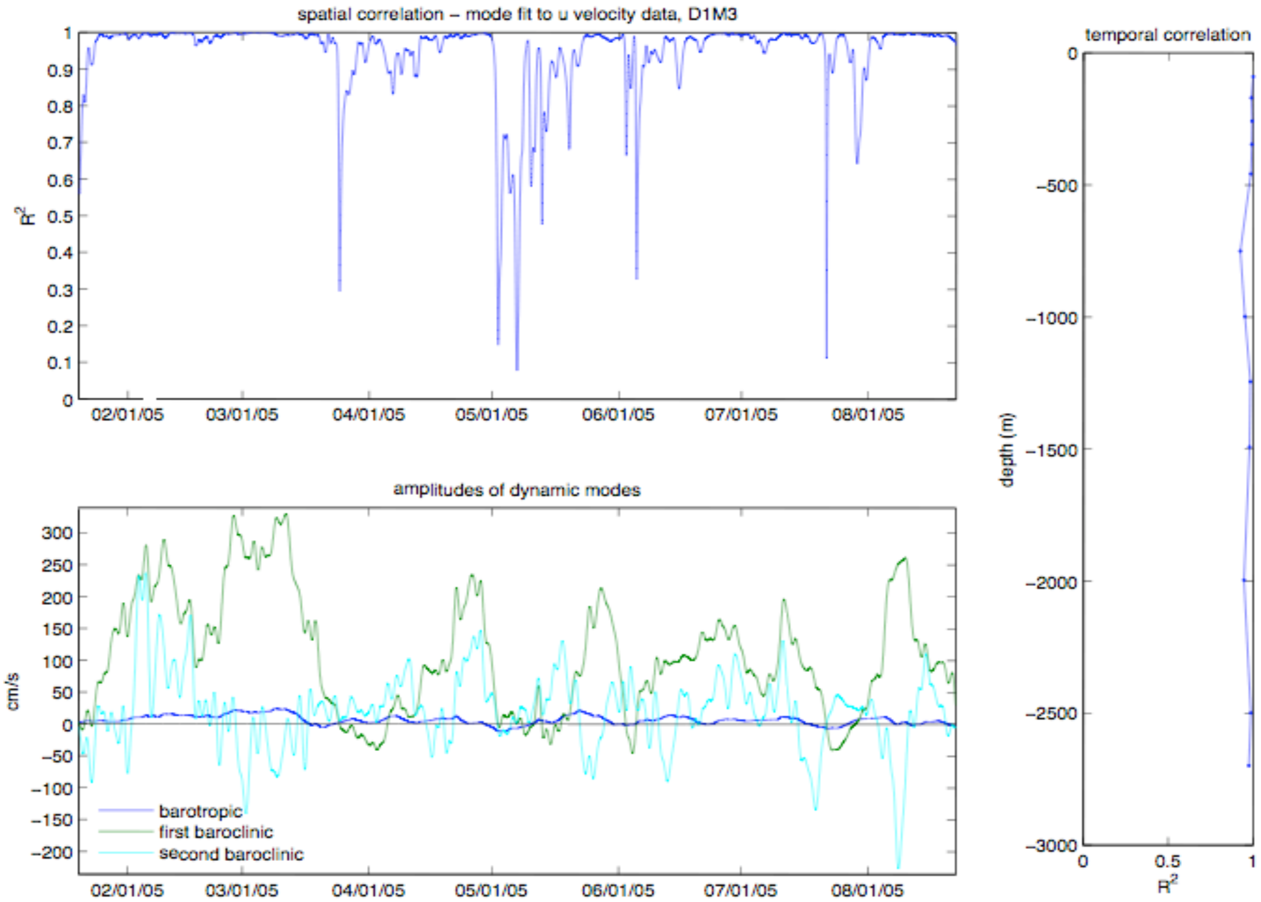

Figure 19. Modal fit to mooring M3 *u*-velocity data. (Top) Spatial correlation between observed *u*-velocity at mooring M3 from deployment 1 and the modeled *u*-velocity from CTD cast data on the EGOM hydrographic cruises. (Bottom) Amplitudes of the first three theoretical modes based on the least squares regression. (Right) Temporal correlation between the modeled and observed velocity.

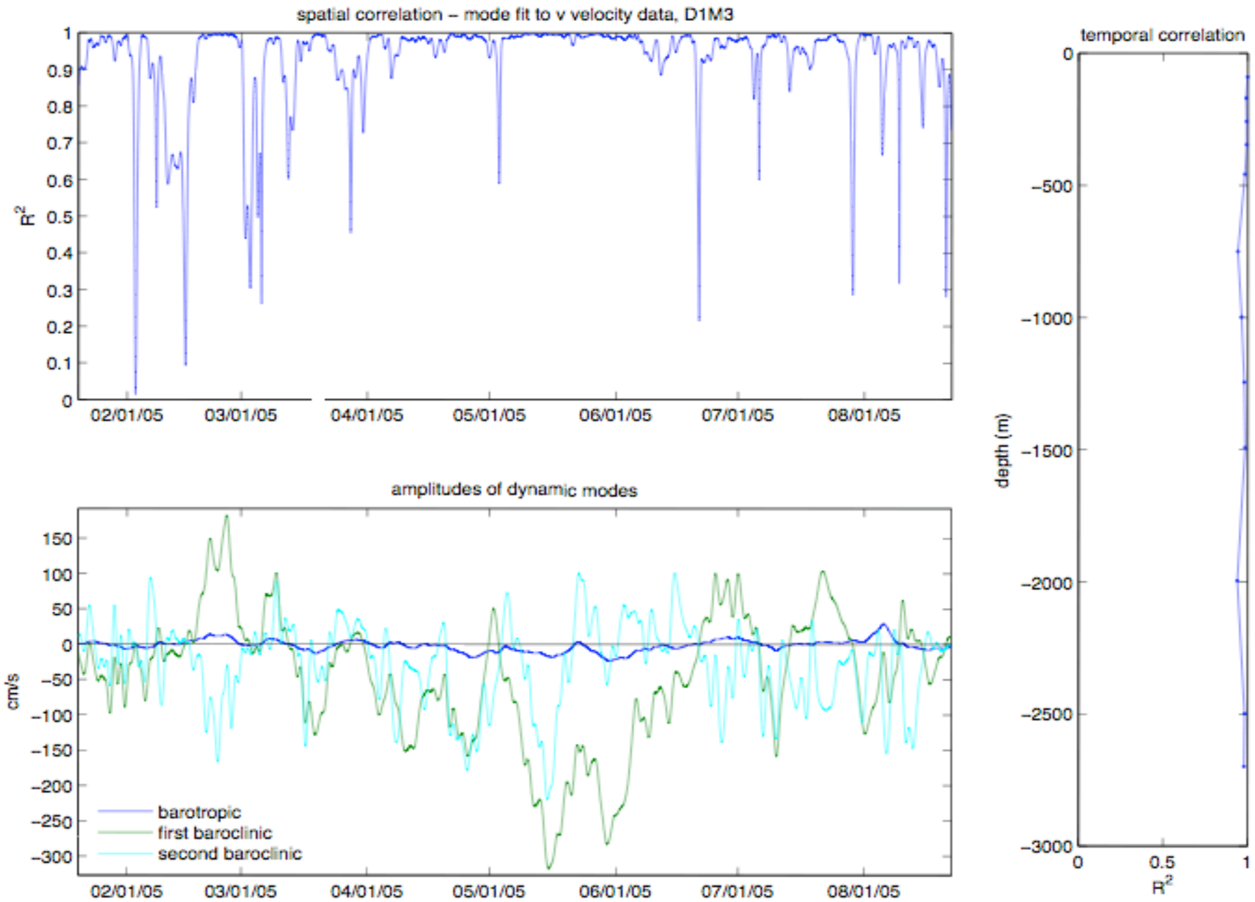

Figure 20. Modal fit to mooring M3 *v*-velocity data. (Top) Spatial correlation between observed *v*-velocity at mooring M3 from deployment 1 and the modeled *v*-velocity from CTD cast data on the EGOM hydrographic cruises. (Bottom) Amplitudes of the first three theoretical modes based on the least squares regression. (Right) Temporal correlation between the modeled and observed velocity.

an indication of the vertical structure of the goodness of fit. Generally, the barotropic time-series amplitudes are significantly smaller than the baroclinic amplitudes at all moorings, both deployments, and both velocity components. As found previously in the EOF analysis, most of the variance in the observed velocity data can be explained by a surface trapped mode that decays exponentially with depth. Therefore, it is expected that the temporal amplitudes of the first baroclinic mode be large, indicating the presence of surface trapped, i.e., eddy related, motions.

The amplitudes of the second baroclinic mode are more variable, i.e., possess higher frequency motions than the first baroclinic mode. During the first deployment, the east-west velocity mode amplitudes are mostly positive, i.e., eastward, because of the location of the mooring relative to the location of the northeastern edge of the Loop Current. The high correlation between mode 1 amplitudes and CTD pressure records, which fluctuate due to mooring draw down, are also validation of the first baroclinic mode amplitudes as indicators of eddy activity in the eastern Gulf.

Spatial correlation at every sample time between observed and modeled velocity from the least squares fit of dynamic modes shows that when the first baroclinic mode amplitudes are close to zero, the correlation is poor. The low correlation could possibly indicate during times of relative quiescence in the wake of eddies, that higher-order modes characterize the vertical structure.

Correlations in the time domain were determined between record length velocity data and modeled velocity at every current meter depth and five ADCP layer depths. The model fits well above 500 m, and below 500 m, the correlation decreases. In some cases, e.g., the fit to velocity components collected during the second deployment, the correlation is minimum between 800 – 1000 m, and may be associated with the kinetic energy minimum at this level in the Gulf.

3.5.3 Model utility tests and summary statistics for the dynamic mode fit

Two types of model utility tests were performed on the modal fit to the observed currents in the space domain. The first test utilizes the F statistic to assess whether a useful relationship between the observed data and any of the modal predictors exists. The null hypothesis, that the coefficients of all modes included in the model equal zero, is rejected if the test statistic is greater than or equal to the F critical value found in an F distribution table. The test statistic is a function of degrees of freedom, the number of modes included in the fit, and spatial correlation, and the F critical value is determined by the degrees of freedom, the number of modes included in the fit, and the significance level, α. For these data, the significance level of $\alpha = 0.05$ was chosen.

The second statistical test is an inference for a single mode coefficient, which determines if a certain mode needs to be included in the fit. This test is a two-tailed test using the t -statistic to reject or accept the null hypothesis that the targeted mode coefficient is equal to zero, i.e., it is not necessary in the multiple regression. The null hypothesis is rejected if the test statistic, calculated from the amplitude of the mode, the error sum of squares, and the error degrees of freedom, falls outside of the rejection region determined by the critical values, which are given in a t table and determined by the degrees of freedom and the significance level α. This test indicates that the first baroclinic mode is necessary to explain the current structure during most of the deployment and surprisingly, the second baroclinic mode is useful to the model for a significant portion of the deployment.

These calculations were performed at each time step during both deployments, providing a time-series of test statistics. Figures A-46 – A-48 in appendix A give time series of the model utility test statistics. The top panel gives the F-test statistic to evaluate the necessity of all of the modes included in the model. At each time step, when the F test statistic (blue line) is greater than the critical value (red line), at least one of the first two baroclinic modes are helpful to the fit of the statistical model to the data. The percentage of time these higher modes are useful to the model during the two deployments are summarized in Tables B-1 and B-2 in appendix B (the fourth column labeled F-test). The bottom two panels illustrate t-test statistics to specifically test the necessity of the first barocinic mode (middle panel) a second baroclinic mode (bottom panel) to the model. When the test statistic (blue line) is between the critical values (red lines), the mode is not useful to the model.

The goodness of fit test confirms that the barotropic and at least one of the baroclinic modes are necessary to the regression approximately 80 - 100 % of the time. Although the second baroclinic mode is not necessary to the model as frequently as the first baroclinic mode, it is a useful predictor of the observed currents for a large portion of the record (columns 5 and 6 labeled t-test in Tables B-1 and B-2 in appendix B).

Tables B-1 and B-2 in appendix B summarize the least squares regression of the dynamic modes onto the moored velocity data. Notice that the mode amplitude means and standard deviations are much larger for the baroclinic modes over the barotropic mode, given their relative amplitudes. When the normalized modes are fit to the data instead of the raw modes calculated via the discritized Taylor-Goldstein equation [*Klink*, 2004], the mode amplitudes change in time such that the barotropic mode exhibits higher amplitudes on the same order as the first baroclinic mode. Also note that in general, the standard deviation of mode amplitudes calculated at mooring M3 are larger, likely due to the higher variance in the eddy field near this mooring.

3.5.4 EOF and dynamic mode comparison

To verify the physical meaning of the surface-trapped first empirical mode, EOF mode 1 was compared to the temporal amplitudes of the first baroclinic mode. This comparison for velocity data at moorings M1 and M3 is shown in Figures 21 and 22 respectively. Clearly, the modes are coherent, especially at low frequencies. EOF modes are centered around zero because temporal means were removed prior to the calculation. This procedure was not followed for the dynamic mode calculation, hence the time series is shifted in the positive direction.

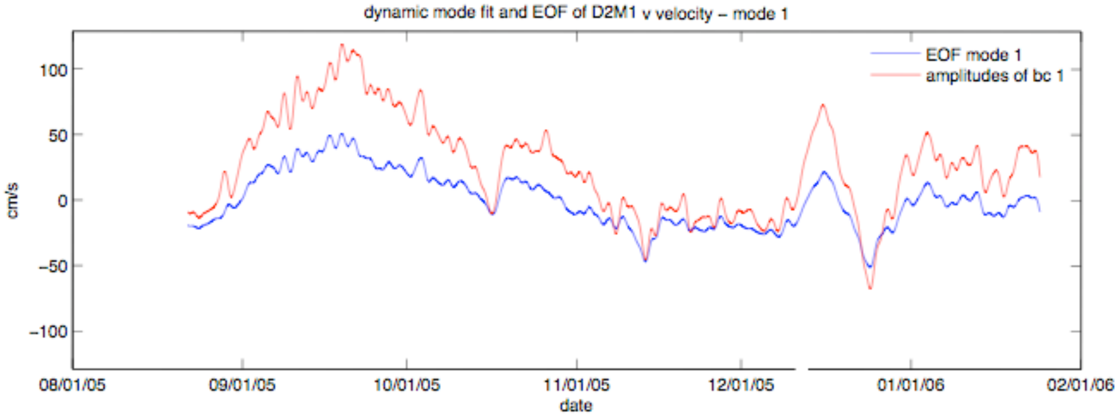

Figure 21. Comparison of EOF mode 1 and the temporal amplitudes of the first baroclinic mode for M1 *v*-velocity during deployment 2.

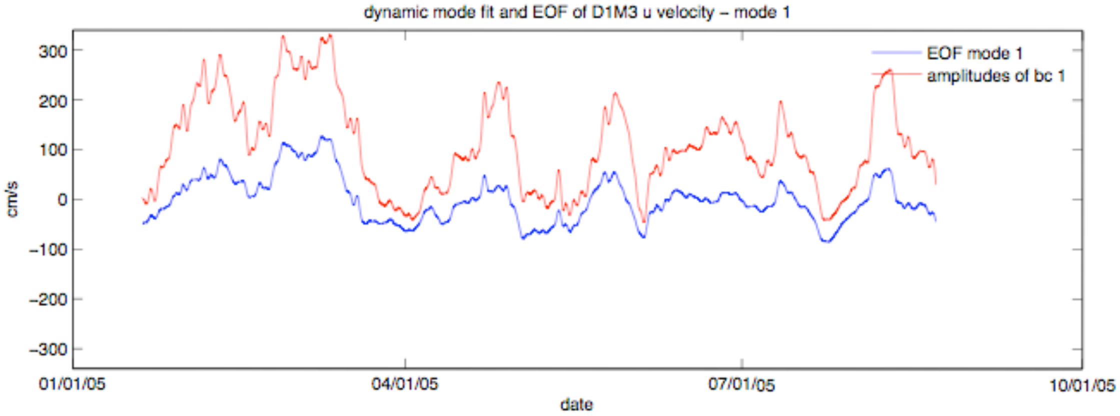

Figure 22. Comparison of EOF mode 1 and the temporal amplitudes of the first baroclinic mode for M3 *u*-velocity during deployment 1.

3.5.5 Temporal correlation of first baroclinic mode and sea surface height gradient

This section investigates potential causes of the observed current structure. Since geostrophic current velocity should be perpendicular to the sea surface height gradient we expect a relationship between sea surface height gradient and the first baroclinic mode. We calculated time series of sea surface height gradient in the north-south and east-west directions in the vicinity of each mooring (sea surface height difference between points 30 km north and south or east and west of the moorings) and correlated that with time series of the first baroclinic mode for the perpendicularly oriented velocity component. In general, significantly large correlation was found between the orthogonal SSH gradient and the first baroclinic mode amplitudes, i.e., east-west velocity mode 1 amplitudes are compared to sea surface height gradient in the north-south direction, and north-south velocity mode 1 amplitudes are compared to sea surface height gradient in the east-west direction (Figure 23 in this section for mode fit to M3 *u*-velocity during deployment 1 and odd numbered Figures A-49 – A-69 in appendix A).

Table 3 summarizes the zero lag correlations between the first baroclinic mode and the sea surface height gradient. Significant correlations, based on the effective degrees of freedom between the two time-series, are bolded, and are not as common as expected. However, the coherency between the two variables indicate in phase coherence at low frequencies despite the insignificant correlation. The coherency spectra show that the coherency is significant only at low frequencies, thus reinforcing that mode 1 amplitudes are related to the pressure gradient, indicating geostrophic currents (Figure 24 in this section for mode fit to M3 *u*-velocity during deployment 1 and even numbered Figures A-50 – A-70 in appendix A).

3.5.6 Spectra and temporal scales of modes

Power spectra and autocorrelation functions are generated for the dynamic mode time-series using FFT methods (as discussed previously). The results from these analyses are consistent between data from each mooring deployment. Spectra of modal amplitudes for the mode fit to mooring M3 velocity data during deployment 1 are presented in Figure 25. Spectra for mode fits to *u* and *v*-velocity exemplify a typical energy and enstrophy-conserving velocity spectrum, with an energy cascade in the red direction, i.e., from high to low frequencies. The barotropic amplitudes exhibit less energy than the first baroclinic modes at low frequencies. Also recall that variance at frequencies greater than 1 cpd is small because 40-hour low-passed filtered versions of the data were used in these calculations. The second baroclinic mode spectra are nearly white (constant) at frequencies less than 1 cpd.

A scales analysis is performed by estimating the first zero-crossing of the normalized autocovariance function (NACF) derived for each modal time-series. This calculation quantifies the temporal lag in which the data becomes decorrelated from previous observations. Results showing the NACF for the fit to the velocity data from mooring M3 during deployment 1 are given in Figure 26. The first baroclinic mode

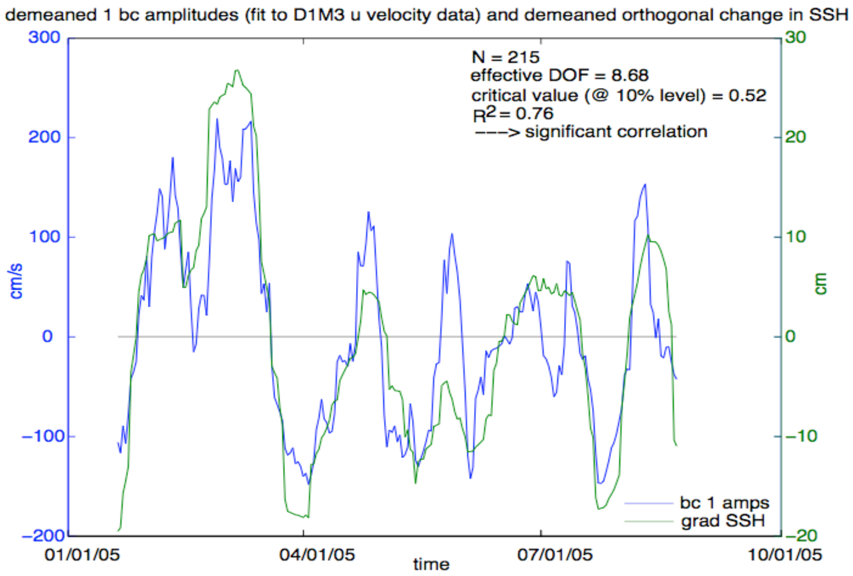

Figure 23. Temporal amplitudes of the first baroclinic mode for the east-west velocity component at mooring M3 during deployment 1 (blue) and the SSH gradient in the north-south direction (green).

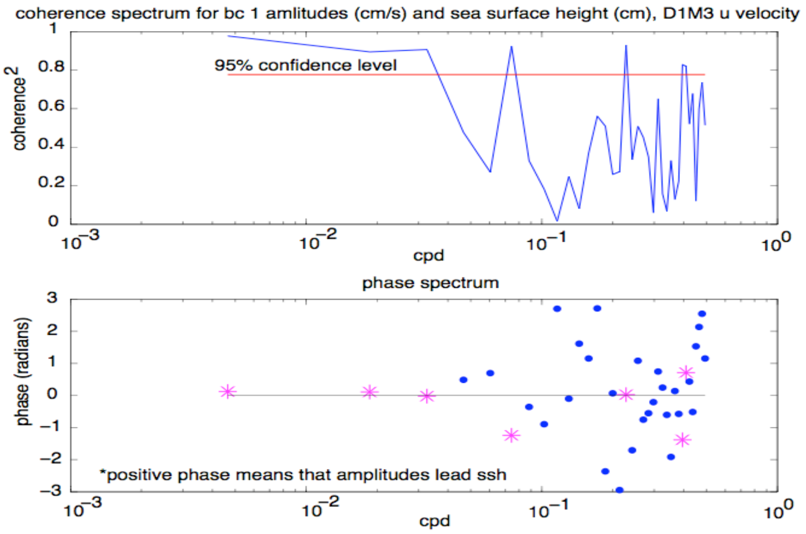

Figure 24. Coherency (top) and phase (bottom) spectra of the temporal amplitudes of the first baroclinic mode for the east-west velocity component at mooring M3 during deployment 1 and the SSH gradient in the north-south direction.

Table 3. East-west and north-south velocity first baroclinic mode amplitude correlations to the orthogonal sea surface height gradient at moorings M1, M2, and M3 for deployments 1 and 2. Bold values indicate significant zero lag correlation at the 90% confidence level.

	Deployment 1		**Deployment 2**	
	East-west velocity	**North-south velocity**	**East-west velocity**	**North-south velocity**
M1	0.56	0.28	0.33	0.43
M2	**0.55**	0.63	0.66	0.58
M3	**0.76**	0.59	**0.80**	0.70

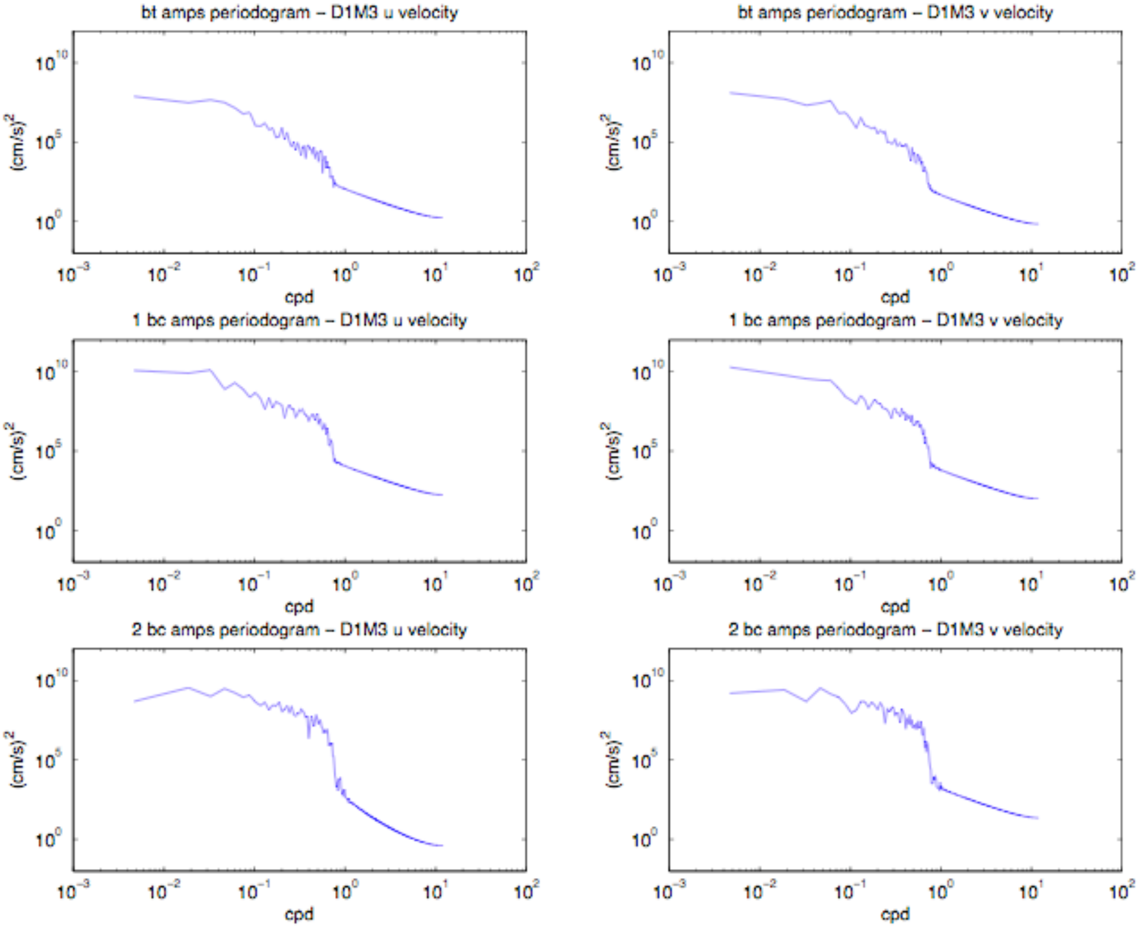

Figure 25. Power spectra of the time-series of amplitudes of the first three theoretical modes at mooring M3 during deployment 1 (top: barotropic mode; middle: first baroclinic mode; bottom: second baroclinic mode). Spectra for fits to the *u*-component and *v*-component are shown in the left and right columns respectively.

amplitudes have the longest time scales (13-39 days), and the second baroclinic mode amplitudes have the shortest time scales (6-7 days). For most of the moored data, the barotropic and first baroclinic mode time series display eddy time scales (~ 25 days), which is expected because of the active eddy regime in the eastern Gulf. Time scales for

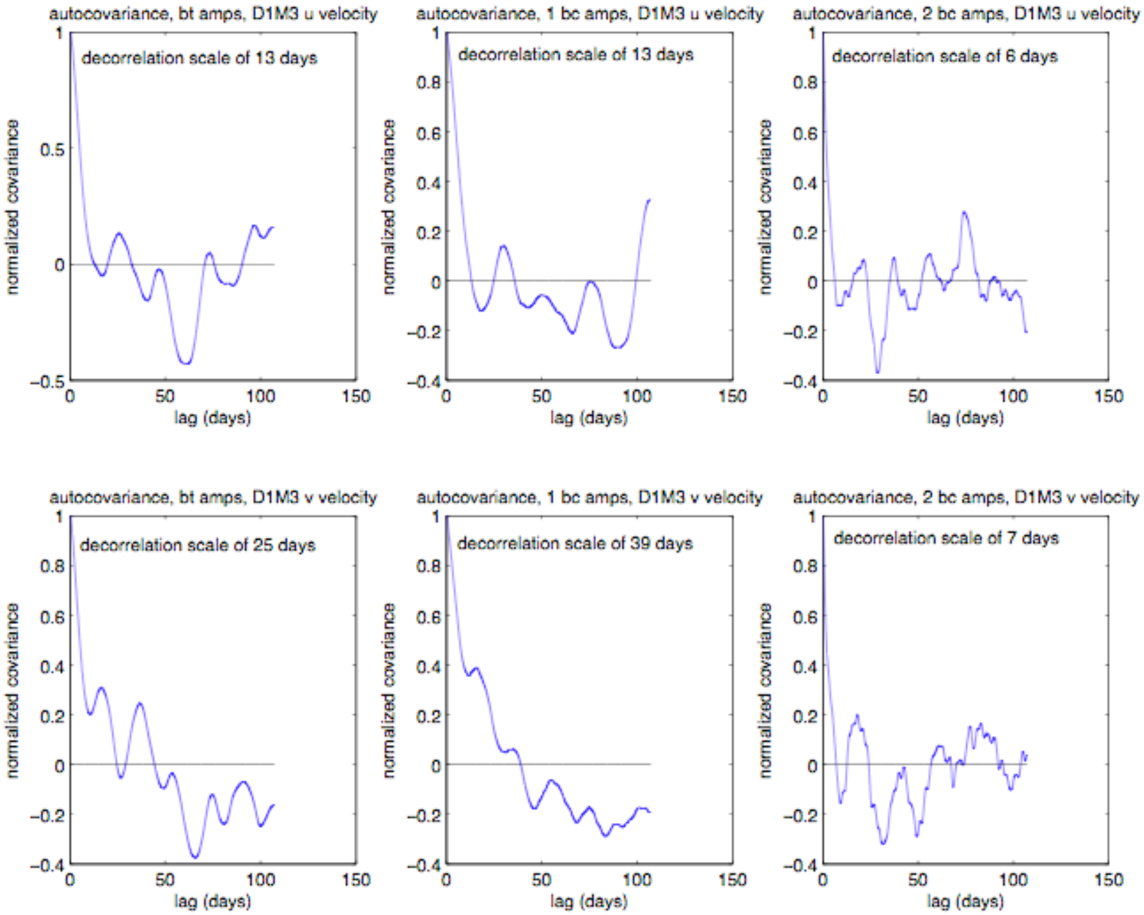

Figure 26. Normalized autocovariance functions of mode amplitudes from the mode fit to east-west and north-south velocity component data at mooring M3 during deployment 1.

the three dynamic modes by velocity component, mooring, and deployment are given in Tables B-3 and B-4 in appendix B.

3.5.7 Dynamic mode kinetic energy and modal coupling

Record length mean kinetic energy, $T(z_m)$, at a fixed level z_m was calculated at each current meter and ADCP bin depth used in the dynamic mode analysis by:

$$T(z_m) = \frac{1}{2L}\sum_{t=1}^{L}\{\sum_{n=0}^{N}(D_{un}(t)\psi_n(z_m))^2 + \sum_{n=0}^{N}(D_{vn}(t)\psi_n(z_m))^2\} \,, \qquad (7)$$

where L is the length of the time series of mode amplitudes, N is the number of modes used in the calculation (in this experiment $N = 2$), $D_{un}(t)$ is the amplitude at time t of the nth mode fit to *u*-velocity data and $D_{vn}(t)$ is the amplitude at time t of the nth mode fit to *v*-velocity data. $\psi_n(z_m)$ is the n^{th} mode value at depth z_m [*Wunsch*, 1997]. Similarly, the kinetic energy in mode k at a fixed depth level z_m, $T_k(z_m)$, is given by:

$$T_k(z_m) = \frac{1}{2L}\sum_{t=1}^{L}\{(D_{uk}(t)\psi_k(z_m))^2 + (D_{vk}(t)\psi_k(z_m))^2\} \,, \qquad (8)$$

The ratio $T_k(z_m) \big/ T(z_m)$ is presented as percentages of kinetic energy in the barotropic, first baroclinic, and second baroclinic modes (record length means) at M3 during deployment 1 at every depth level in Table 4 in this section, and for the other mooring deployment in Tables B-5 – B-9 with summary figures in appendix B.

The energy distribution is similar for all of the mooring deployments. From these tables and figures it is clear that the second baroclinic mode makes a small contribution to the water column kinetic energy, except for at the base of the upper layer around 500 m. For deployment 2 data, the second baroclinic mode exhibits more kinetic energy closer to the Loop Current from mooring M1, to mooring M3, but for deployment 1 data, the distribution of kinetic energy in the second baroclinic mode is about the same at each mooring.

The other interesting pattern to observe is the energy exchange between the barotropic mode and the first baroclinic mode above 1500 m. Near the surface, most of the kinetic energy is in the first baroclnic mode, and there is only slightly more energy in the barotopic mode than the second baroclinic mode. The kinetic energy in the first baroclinic mode decreases as the energy in the barotropic mode and second baroclinic mode increases. The second baroclinic mode reaches maximum kinetic energy at ~500 m and then decreases to near zero around 1000 m. The barotropic mode continues to grow and the first baroclinic mode continues to wane to ~750 m were they reach their respective maximum and minimum. The barotropic and first baroclinic mode contribute approximately the same amount of kinetic energy below 1500 m. This energy division is a reflection of the importance of the first baroclinic mode in the upper water column and the increasing importance of the barotropic mode with depth.

Mode correlations were investigated using a simple coefficient of determination and a significance test based on the statistical t-distribution. Correlations between mode amplitudes from the mode fit to data from the same mooring deployment for the same velocity component are presented in Tables B-10 – B-15 in appendix B. Significant correlations are bolded. Correlations between mode amplitudes of different velocity components yielded no significant correlation, and therefore are not included in the tables.

Table 4. Percentages of kinetic energy in the barotropic (BT), first baroclinic (1BC), and second baroclinic (2BC) modes at each depth level at mooring M3 during deployment 1. The figure on the right is a summary plot of the Kinetic energy percentages in the table.

Depth	$\%T_{BT}(z_m)$	$\%T_{1BC}(z_m)$	$\%T_{2BC}(z_m)$
90 m	5.82 %	93.70 %	0.49 %
170 m	13.72 %	84.38 %	1.90 %
258 m	24.75 %	68.03 %	7.22 %
346 m	34.81 %	53.83 %	11.36 %
458 m	51.58 %	34.06 %	14.37 %
750 m	93.37 %	1.51 %	5.12 %
998 m	70.07 %	29.86 %	0.07 %
1245 m	56.69 %	42.03 %	1.28 %
1492 m	53.33 %	44.86 %	1.80 %
1996 m	52.17 %	45.82 %	2.01 %
2499 m	52.07 %	45.90 %	2.03 %
2699 m	52.07 %	45.90 %	2.03 %

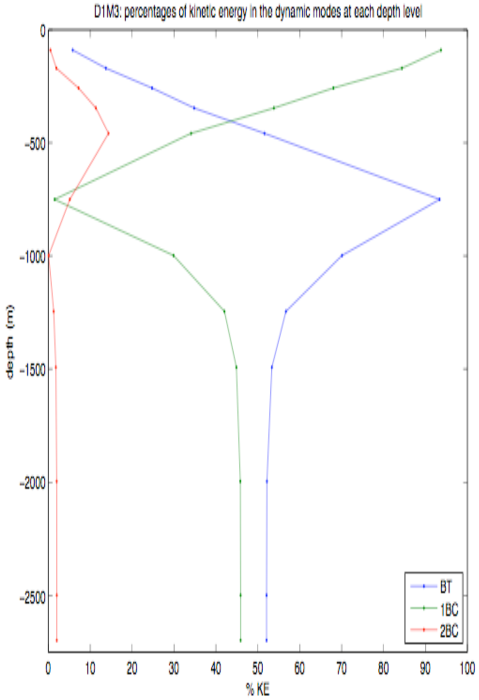

The significant correlation between the barotropic and first barclinic mode is nearly always present for all mooring deployments, especially for the *u*-velocity component. Interestingly, all modes are correlated for mooring M2 *v*-velocity during deployment 2, which is unusual since no modes are correlated for the *u*-velocity component at M2 or the *v*-velocity components at moorings M1 and M3 from the same deployment. This might be an effect of the relative position of mooring M2 to the frontal cyclone during deployment 2. Mooring M2 was usually in the center of the frontal cyclone, as opposed to the position of the other moorings predominantly on the edge of the cyclone.

3.5.8 Modal decomposition of EGOM data versus historical data

The dynamic modes used in the previous analyses were calculated from Brunt-Väisälä frequency profiles at or closest to the mooring measured before and after each deployment. The use of an average of two profiles to construct dynamic modes to fit the velocity data collected throughout deployment is somewhat unrealistic, given that in the eastern Gulf of Mexico the density (temperature and salinity), and hence the dynamic modes, change shape rapidly in the eddy field (this usually affects the zero crossings of the prevalent modes). To assure the results previously discussed are sound, the same analyses were carried out using historical CTD data. In the DW Report, historical data collected since the early 1900s were reanalyzed. All good quality historical data in the eastern Gulf (east of 89°W) was used to create an average Brunt-Väisälä frequency profile for the eastern Gulf of Mexico. Dynamic modes calculated from this profile were fitted to EGOM velocity data using the methods previously discussed and yielded mode amplitudes comparable to those found from the fit of modes assembled from the sparse EGOM CTD data. Some examples from moorings M1 and M3 are illustrated in Figures 27 and 28.

The amplitudes are coherent, probably because the fluctuation in mode shape due to the density field happen on smaller scales than the vertical spacing of data used in the mode calculation or possibly shallower than the shallowest moored time series. However, it is necessary to space the data like this because, statistically, to use all of the

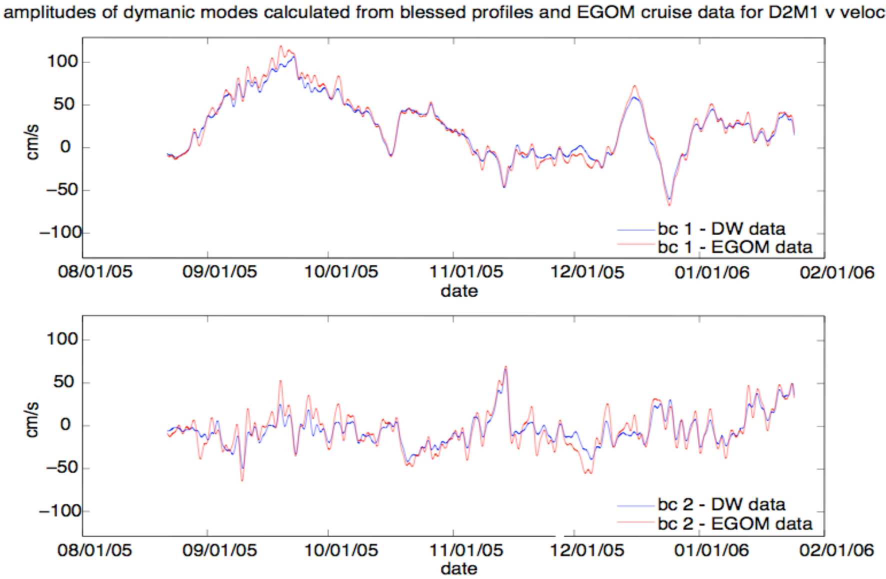

Figure 27. Temporal amplitudes of the first baroclinic mode (top) and second baroclinic mode (bottom) for M1 *v*-velocity during deployment 2 calculated using EGOM CTD cast data (red) and historical CTD data analyzed in the MMS Deepwater Physical Oceanography Reanalysis and Synthesis of Historical Data project (blue).

ADCP data would weight the abundant (~50) measurements in the surface ocean too much over the fewer (~7) current meter records in the deep ocean, thereby skewing the EOF and dynamic modes amplitudes.

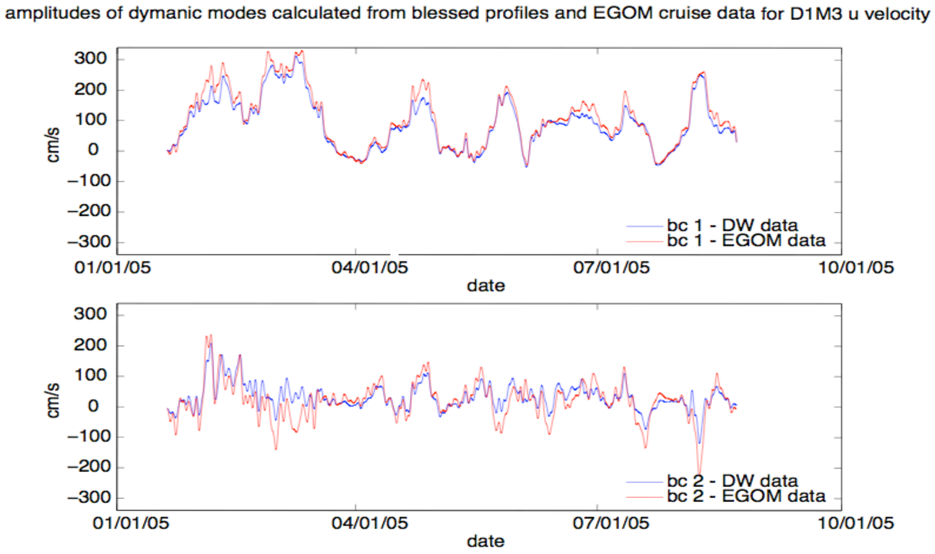

Figure 28. Temporal amplitudes of the first baroclinic mode (top) and second baroclinic mode (bottom) for M3 *u*-velocity during deployment 1 calculated using EGOM CTD cast data (red) and historical CTD data analyzed in the MMS Deepwater Physical Oceanography Reanalysis and Synthesis of Historical Data project (blue).

4. DISCUSSION AND CONCLUSIONS

The importance of low-frequency motion to the circulation in the eastern Gulf of Mexico was addressed in this thesis. Low frequency currents observed by the EGOM array were decomposed into empirical and theoretical modes to observe the effects of the eddy field on horizontal current velocity. There was a strong similarity between dynamical and empirical modes. The high contribution of the first baroclinic mode relative to the other dynamic modes was observed and assessed.

The passage of the northern lobe of the Loop Current and the developing anticyclone over the study area cause intensified surface velocities which amplify the first baroclinic mode, also called the eddy or surface-trapped mode. The barotropic and first baroclinic mode amplitudes exhibit low frequency variability, substantiating the first hypothesis stated in the introduction. First baroclinic mode amplitudes are coherent with moored CTD pressure and a scales analysis of the temporal amplitudes of the first baroclinic mode indicate eddy time scales of 10 – 40 days. Clearly, the first baroclinc mode amplitudes are influenced by the Loop Current and eddy field. For example, during deployment 1, the amplitudes of the *u*-velocity first barolinic mode are mostly positive at mooring M3, indicating eastward flow. This is caused by the moorings position at the northern edge of the loop current and the growing eddy.

The second baroclinic mode contributes a relatively large amount of vertical shear and promotes mixing in the upper ocean. For a given level of wave energy, if the modal distribution of energy is weighted towards the second baroclinic mode, low

Richardson numbers and high shear variance occur, which in turn increases the probability of shear instabilities [*Mackinnon and Gregg,* 2003]. In this study, energy was found to be concentrated in lower modes, and the second baroclinic mode amplitudes showed higher frequency variability and were not significant to the regression model as often as the first baroclinic mode. However, the regression analysis shows second baroclinic mode amplitudes comparable to first baroclinic mode amplitudes at times, especially at mooring M3, indicating higher order dynamics that could be related to eddy shedding or frontal eddies present in the study region.

Inoue [1985] found that some mooring locations in Drake Passage showed a higher contribution of the higher baroclinic modes (he hypothesized this was due to topographic effects in the southern part of the passage), but in the EGOM region, higher modes are not favored at any mooring site. Time scales of the modes in the EGOM study area do not monotonically increase or decease towards the loop current as hypothesized. For north-south velocity barotropic and first baroclinic modes, the time scales are fairly consistent between moorings (most within 10 days of each other).

There is higher spatial correlation between modeled and observed horizontal velocity when mode one amplitudes are large. There also seems to be poor correlation between modeled and observed velocity in the time domain at 500 – 1000 m, where an energy minimum is present in the Gulf. The first baroclinic mode amplitudes and SSH gradient are coherent at low frequencies, but the correlation is not always significant at zero lag.

In agreement with the second hypothesis, the first baroclinic mode amplitudes were affected by the surface intensification of the eddy field. Figure 29 shows sea surface height on March 25, 2005 in the EGOM study region and in the entire Gulf. The arrows in the figure on the right represent velocity at 50 m (black arrows) and 250 m (pink arrows) depth at moorings M1, M2, and M3. The moorings appear to be in a cyclonic eddy in an area of weak vertical shear, which is reflected in the small first and second barocilinic mode amplitudes (Figures 19, 20, A-36, A-37, A-40, and A-41). Similarly, Figure 30 shows the sea surface height on June 11, 2005 in the Gulf of Mexico. The amplitudes of the *u*-velocity first baroclinic mode are large at this time at all of the moorings, especially at mooring M1, as it is positioned at the greatest gradient

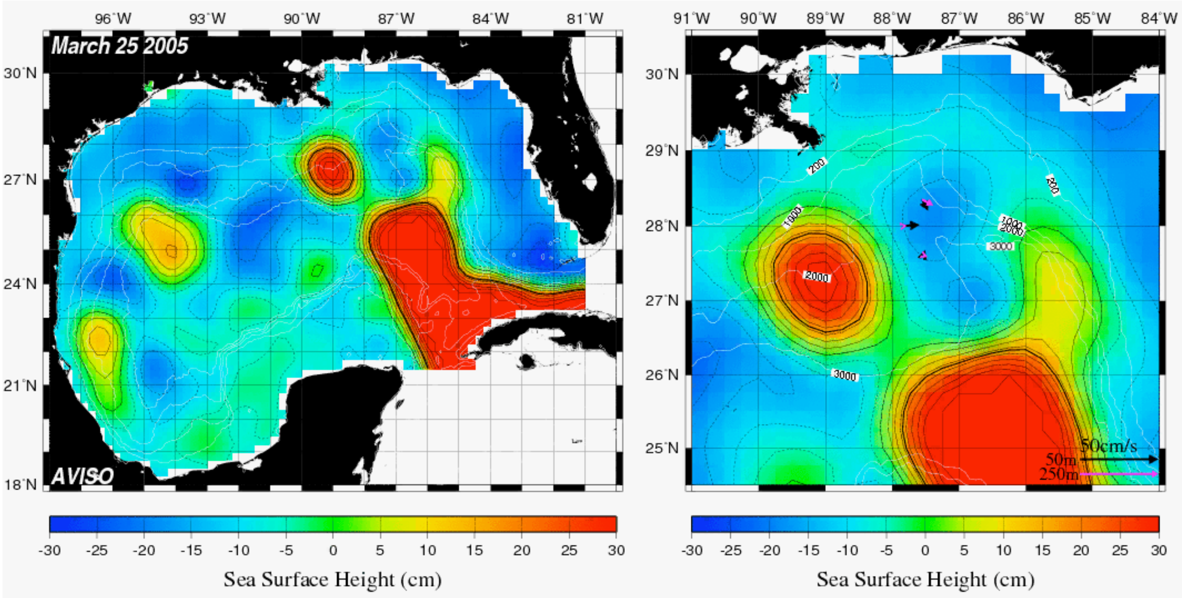

Figure 29. (Left) Sea surface height (from R. Leben) in the Gulf of Mexico on March 25, 2005. (Right) Sea surface height in the EGOM study region. Arrows represent velocity at 50 m and 250 m depth at M1, M2, and M3. Contours are 5 cm apart.

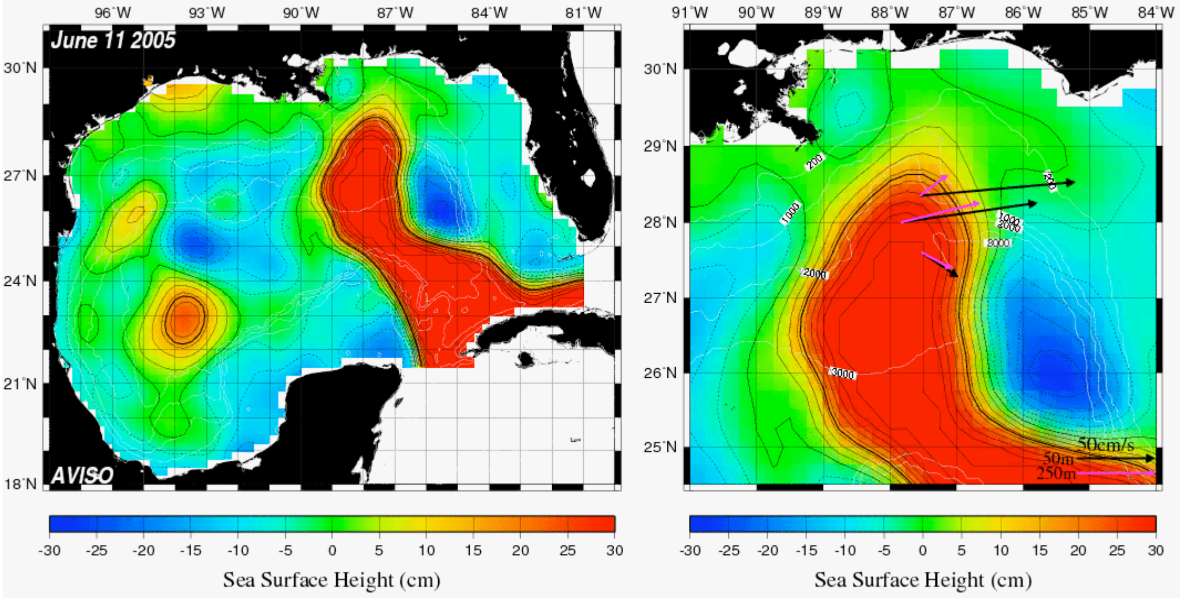

Figure 30. (Left) Sea surface height (from R. Leben) in the Gulf of Mexico on June 11, 2005. (Right) Sea surface height in the EGOM study region. Arrows represent velocity at 50 m and 250 m depth at M1, M2, and M3. Contours are 5 cm apart.

of sea surface height (Figures 19, A-36, and A-40). It is clear from these images that the position of the Loop Current and it's eddies relative to the moorings is manifested in the temporal evolution of the first baroclinic mode.

Changes in vorticity with depth are characterized by vertical shear and are vital to eddy shedding, but the EGOM study site is too far north of the Loop Current eddy shedding region and there are too few separation events in this dataset to adequately evaluate the impact of eddy shedding on the second baroclinic mode amplitudes. There is one interesting event that should be noted. Figure 31 shows sea surface height on August 9, 2005 in the Gulf of Mexico. The eddy in this figure in the north central Gulf reattaches to the Loop Current at the end of August just before separating a final time in

September and traveling west. The second baroclinic mode at mooring M3 on this date is highly amplified (Figure 19), which could be a result of the shear related to instabilities tied to eddy separation.

Contrary to the second hypothesis, the barotropic mode amplitudes were found to be small throughout deployment at all of the moorings. This is a surprising result, as previous studies have found the barotropic mode amplitudes along with the first baroclinic mode amplitudes to dominate in most deepwater regions. *Wunsch* [1997] concluded that most areas are dominated by a barotropic and first baroclinic component to flow, from a modal analysis of data from the north Atlantic, a latitude band in the north Pacific, and a few stations in the south Atlantic. This is likely simply a difference

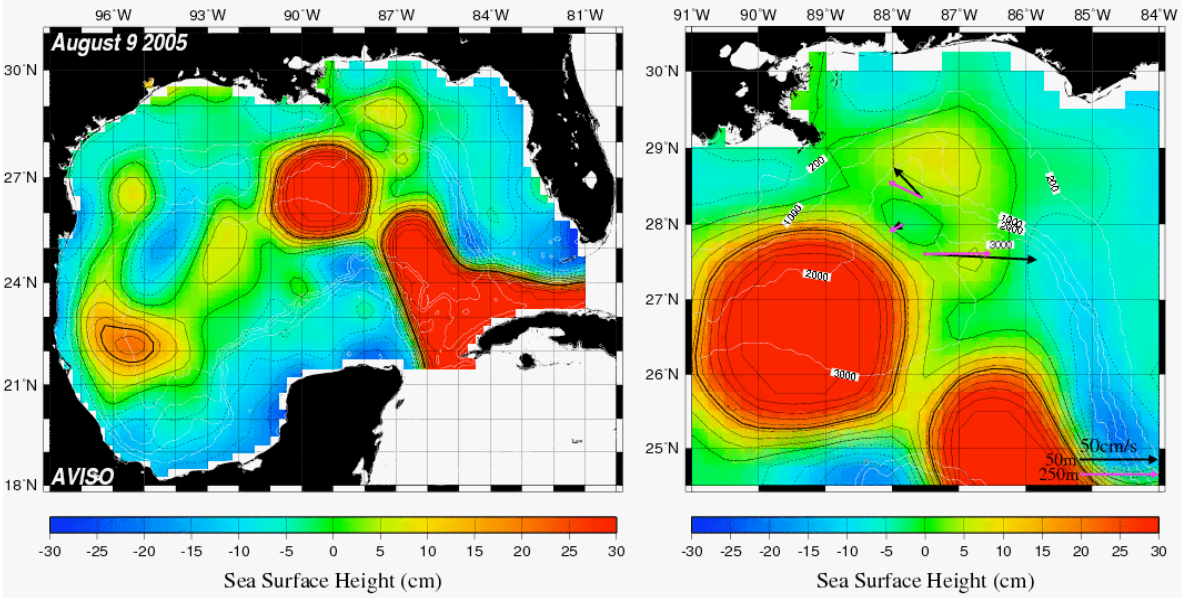

Figure 31. (Left) Sea surface height (from R. Leben) in the Gulf of Mexico on August 9, 2005. (Right) Sea surface height in the EGOM study region. Arrows represent velocity at 50 m and 250 m depth at M1, M2, and M3. Contours are 5 cm apart.

in the method of the applied statistics in the analysis. In this study, the temporal mean was not removed from the time-series data for fear of altering the barotropic mode amplitudes, and the dynamic modes were not normalized before they were fit to the moored velocity data through a multiple regression. Thus, the baroclinic modes were quite small relative to the barotropic mode, which was taken to be one throughout the water column (the barotropic mode can be thought of as the y-intercept in traditional regression analysis). This is not the same procedure followed by others, for which the barotropic mode was found to attain amplitudes almost as large as the first baroclinc mode's. To compare these results to others, it must be understood that the mode amplitudes simply give half of the information, and only by multiplying the amplitudes by the mode values can useful quantities be obtained (as seen in section 3.5.7 with the kinetic energy calculation).

This is not to say that trends cannot be analyzed by looking at the dynamic mode amplitudes. Corroborating the third hypothesis, the barotropic mode amplitudes and first baroclinic mode amplitudes were found to be correlated in almost every case, which suggests that the barotropic and first baroclinic modes follow the same driving mechanisms and ultimately net transport and current shear are coupled. The strong vertical shear in the mean currents could lead to baroclinic instability and eddy shedding. This is in agreement with the findings of *McWilliams and Shen* [1980], who determined that there were significant barotropic and first baroclinic modal covariances between both streamfunction and velocity fields. Furthermore, it is the combination of the first baroclinic and barotropic modes that gives the vertical structure for the first empirical mode [*Inoue*, 1985]. Higher order modes were correlated in some cases in this analysis, but it was more variable than the barotropic – first baroclinic coupling. The results of the partition of kinetic energy amongst the dynamic modes presented in section 3.5.7 indicate that the barotropic mode contains more than (or approximately the same) amount of kinetic energy as the first baroclinic mode below ~ 500 m.

During the EGOM Study mooring deployment, five hurricanes and one tropical storm traversed the gulf; the most severe being Hurricanes Katrina and Rita, which caused devastating loss of life and property damage to the Gulf coast. Hurricane Katrina entered the Gulf of Mexico on August 26, 2005 and was nearest the study area on August 28, 2005; Hurricane Rita entered the Gulf of Mexico on September 20, 2005 and was nearest the study region on September 22, 2005. The signature of these storms is not evidenced in the dynamic mode amplitudes, as they were created from low-pass filtered data.

A direct response of the ocean to this atmospheric forcing is a wake of near-inertial oscillations, characterized by the downward propagation of energy and upward propagation of leading phase. Near-inertial motions are an essential and ubiquitous element of ocean circulation, evidenced by the high degree of coherency in the near inertial band discussed in sections 3.4.2 and 3.4.3. *Xing and Davies* [2005] found that inertial-internal waves propagate at near-inertial frequencies modified by the nonlinear effects associated with vorticity in the eddy.

Figure 32 gives contours of the frequency-averaged wavelet power in the inertial band (0.5 – 2 day period) during the weeks after Hurricanes Katrina and Rita in the upper 500 m of the water column at moorings M1, M2, and M3. The wavelet method estimates the temporal variability of energy in specified frequency bands. Wavelet power spectra were generated for all detided, gap-filled, gridded ADCP and current meter records using a Morlet basis function. The method described in *Torrence and Compo* [1998] was used to transform observed time-series into Fourier space.

The downward propagation of inertial energy after Katrina and Rita to at least 500 m is indicated in this figure. The strongest response to the storms is seen at moorings M2 and M3, as the storm track was just southwest of the moorings. Note that

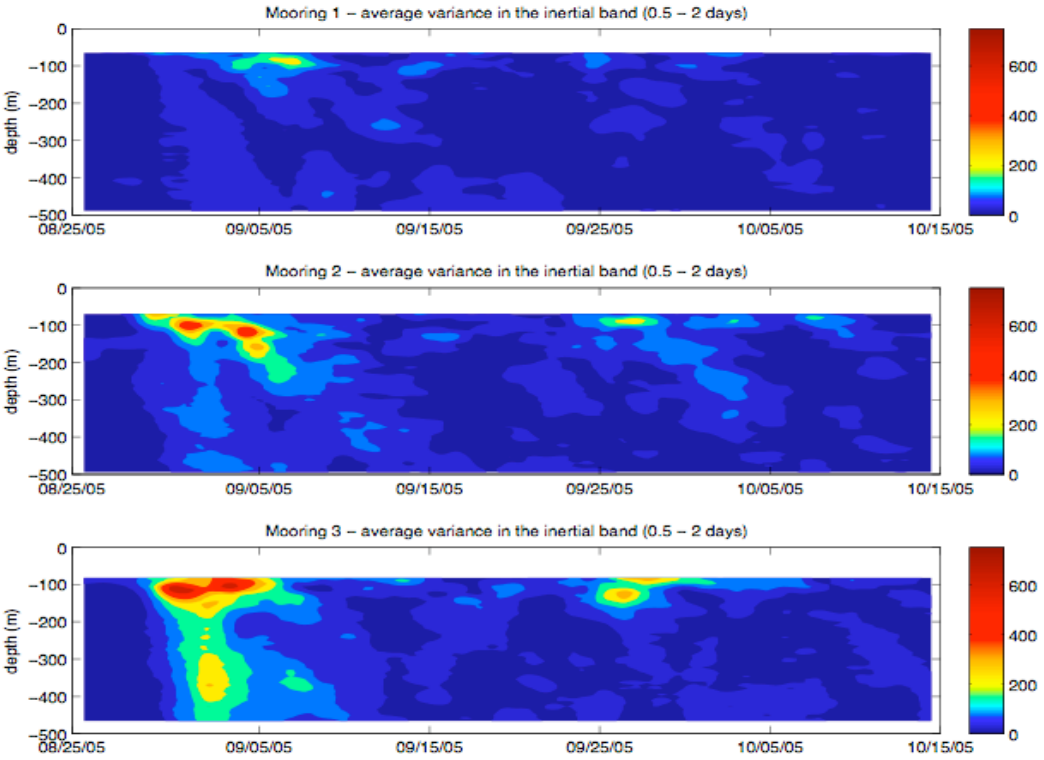

Figure 32. Contours of the frequency-averaged wavelet power in the inertial band (0.5 – 2 day period) during the weeks after Hurricanes Katrina and Rita in the upper 500 m of the water column at moorings M1 (top), M2 (middle), and M3 (bottom).

there are generally two subsurface maxima of energy present after the storms and two paths for inertial energy are revealed. There is a direct influence on the entire water column that occurs during or immediately after the storm due to the storm's intensity, evidenced by the nearly vertical column of high inertial energy around September 1, 2005. There is also the downward propagation of inertial energy, evidenced by the diagonal streak of high energy following the storm. It seems that the initial response to the storms is strongest at M3, while the propagation response is strongest at M2. Inertial waves after Katrina are present more than 2 weeks after the storm and penetrate quickly to the base of the upper layer. It is interesting to note the energy minimum between 200 and 300 m at mooring M3, which may represent the effect of the pycnocline on the downward energy propagation. Inertial oscillations are usually confined to the upper 100 m of the ocean and decay rapidly below the mixed layer [*Pollard*, 1970]. The amplitudes of inertial oscillations after Hurricane Rita are not as large as the motions excited by Hurricane Katrina and don't penetrate as deep, but appear to persist at the surface longer. The presence of a cold core eddy in the study region during the passage of these storms has likely affected the inertial motions. The rate of downward inertial energy propagation is roughly 30 m/day. *Brooks* [1983] estimated the vertical energy transport velocity of the wake of inertial oscillations in the western Gulf after Hurricane Allen in 1980 to be ~ 60 m/day. *Pollard* [1970] established that variance in the wind field on the order of an inertial period or shorter can initiate and destroy inertial motions, which could be the cause of the fingering of inertial energy down into the water column.

The EOF analysis in this thesis does not suggest the propagation of topographic Rossby waves through this region. The deep ocean spectra presented in section 3.3.2 show some indication of bottom intensification, i.e. elevated energy at sub-inertial frequencies, but there are no dominant spectral peaks that distinguish topographic Rossby waves (18 – 37 day period) in the Gulf [*Hamilton*, 1990]. Horizontal coherency of deep ocean time-series between the moorings indicate minimal coherency. The weak coherence between moorings M2 and M3 *u*-velocity in the deep records during deployment one (Figures 14 and 15) is the best indication of topographic effects. The conjecture that this could be a generation region for topographic Rossby waves was not tested in this analysis, but since the EGOM study area is flat bottomed and a great distance form the Loop Current eddy shedding region, topographic Rossby wave generation is not likely to be observed in these data.

Future research objectives in the Gulf of Mexico should include studies focused on the stochastic formation and separation of rings from the Loop Current, as they are an important part of the heat and salt budgets of the Gulf. Studies directed at understanding the exact mechanism of generation of topographic Rossby waves, which could be related to eddy shedding, ring-ring interaction, or ring-topography interaction [*Oey and Lee,* 2002], should be conducted as well. From the EGOM data, it is clear that a study of the Loop Current, further south of the EGOM region, would be helpful to our understanding of these phenomena.

The Eastern Gulf of Mexico Circulation Study provides a complete, good quality, year-long data set that encapsulates the current regime of this region.

Furthermore, signatures of atmospheric and oceanic events of great magnitude are evident in these data, such as the passages of Hurricanes Katrina and Rita through the Gulf and the separation of Eddy Vortex from the Loop Current. The analyses presented in this thesis were somewhat limited by the depth and duration of the measurements. Longer time-series from moored instruments would be useful to investigate the inter-annual variability of currents, and data closer to the surface would provide a means of studying the current-wind relationship in the eastern Gulf. Diurnal variability of currents related to sea breeze and the tropical storm induced affects on currents in the surface ocean of the eastern Gulf could be better evaluated with data in the upper 40 m of the water column. Wavelet coherency between wind and current velocity would be interesting to calculate as well.

Low-frequency waves have a different modal energy distribution than high-frequency waves [*Mackinnon and Gregg,* 2003]. Sub-inertial variability was explored in this thesis, but inertial band and super-inertial variability in the EGOM dataset should be considered as well. An in depth analysis of the cold core eddy in the study region during the second deployment and its affect on the inertial-internal wave propagation after the hurricanes would be helpful in understanding the doppler shift of the inertial frequency due to the vorticity of the Loop Current and the eddy field. EGOM observations could be paired with modeling and theory to evaluate if the presence of the cold core eddy in the study site damps the wake of internal waves caused by the storm or possibly advects them away. It is unlikely that packets of inertial oscillations at great depths are generated by a single atmospheric event at the surface [*Pollard,* 1970]; they could be the result of an eddy.

The conclusion of this study is that the low-frequency currents in the eastern Gulf of Mexico can be accurately depicted by a linear combination of the first three theoretical dynamic modes. The barotropic and first baroclinic modes alone represent the horizontal current structure ~ 20 - 40% the time, but there are significant excursions from this regime that correspond to higher order structure as well as deviations from geostrophy, and it is plausible that they are linked to complex Loop Current dynamics. The vertical structure of low-frequency horizontal currents in the eastern Gulf of Mexico is driven by the northward extent of the Loop Current and the temporally and spatially varying eddy field. Frontal eddies play an important role in the mesoscale circulation; perhaps more so than Loop Current anticyclones, but it is an amalgam of these dynamic features that comprise the currents.

REFERENCES

Brooks, D. A. (1983), The wake of Hurricane Allen in the western Gulf of Mexico, *J. Phys. Oceanogr.*, *13*(1), 117 – 129.

Bunge, L., J. Ochoa, A. Badan, J. Candela, and J. Sheinbaum (2002), Deep flows in the Yucatan Channel and their relation to changes in the Loop Current extension, *J. Geophys. Res.*, *107*(C12), 3233, doi:10.1029/2001JC001256.

Candela, J., J. Sheinbaum, J. L. Ochoa, and A. Badan, and R. Leben (2002), The potential vorticity flux through the Yucatan Current and the Loop Current in the Gulf of Mexico, *Geophys. Res. Lett.*, *29*(22), 2059, doi:10.1029/2002GL015587.

Charney, J. G., and G. R. Flierl (1981), Oceanic analogues of large-scale atmospheric motions, in *Evolution of Physical Oceanography*, edited by B. A. Warren and C. Wunsch, pp. 504–548, MIT Press, Cambridge, MA.

Chérubin, L. M., W. Sturges and E. P. Chassignet (2005), Deep flow variability in the vicinity of the Yucatan Straits from a high-resolution numerical simulation, *J. Geophys. Res.*, *110*(C4), C04009, doi:10.1029/2004JC002280.

Chérubin, L. M., Y. Morel and E. P. Chassignet (2006), Loop Current ring shedding: the ormation of cyclones and the effect of topography, *J. Phys. Oceanogr.*, *36*(4), 569 – 591.

Coats, D. A. (1992), The Loop Current, in *The Physical Oceanography of the U.S. Atlantic and Eastern Gulf of Mexico*, edited by J. D. Milliman and E. Imamura, chap. 6, U.S. Dep. Of the Interior, Minerals Management Service, Atl. OCS Region, Herndon, VA.

Cochrane, J. D. (1972), Separation of an anticyclone and subsequent developments in the Loop Current, in *Contributions on the Physical Oceanography of the Gulf of Mexico, Texas A&M Oceanographic Studies*, vol. 2, edited by L. R. A. Capurro and J. L. Reid, pp. 91 – 106, Gulf Press, Houston, TX.

Cushman-Roisin, B. E., E. P. Chassignet, and B. Tang (1990), Westward motion of mesoscale eddies, *J. Phys. Oceanogr.*, *20*(5), 758 – 768.

Dietrich, G. (1937), Die Lage Meeresoberfläche im Druckfeld Ozean und Atmosphäre mit besonderer Berücksichtigund des westlichen Nordatlantischen Ozeans und des Golfs von Mexiko. Veröffentlichungen des Institut für Meereskunde an der Universität Berlin, Heft *33*, 5 – 52.

DiMarco, S. F., A. E., Jochens, and M. K. Howard (1997), LATEX Shelf data report: current meter moorings, April 1992 through December 1994. *Technical Report No. 97-01-T*, 61 pp., Texas A&M University, Oceanography, College Station, TX. (Available on CD-ROM NODC-88, *Texas-Louisiana Shelf Circulation and Transport Processes Study, Current meter, meteorological buoy, XBT/XSV/XCP/CTD/IES Data and Reports*, 1992-1994)

DiMarco, S. F., W. D. Nowlin, Jr., and R. O. Reid (2005), A statistical description of the velocity fields from upper ocean drifters in the Gulf of Mexico, in *Circulation in the Gulf of Mexico: Observations and Models*, edited by W. Sturges and A. Lugo-Fernandez, pp. 101-110, AGU, Washington, DC.

Donohue, K., P. Hamilton, K. Leaman, R. Leben, M. Prater, E. Waddell, and R. Watts (2006), Exploratory study of deepwater currents in the Gulf of Mexico, *OCS Study MMS 2006-073*, 76 pp., U.S. Dept. of the Interior, Minerals Management Service, Gulf of Mexico OCS Region, New Orleans, LA.

Elliott, B. A. (1982), Anticyclonic rings in the Gulf of Mexico, *J. Phys. Oceanogr.*, *12*(11), 1292 – 1309.

Emery, W. J., and R. E. Thompson (2001), *Data Analysis Methods in Physical Oceanography*, Elsevier, Amsterdam.

Fratantoni, P. S., T. N. Lee, G. P. Podesta, and F. Muller-Karger (1998), The influence of Loop Current perturbations on the formation and evolution of Tortugas eddies in the southern Straits of Florida, *J. Geophys. Res.*, *103*(C11), 24759 – 24779.

Fuglister, F. C. (1951), Annual variations in current speeds in the Gulf Stream, *J. Mar. Res.*, *10*(1), 119 – 127.

Gill, A. E., J. S. A. Green, and A. J. Simmons (1974), Energy partition in the large-scale ocean circulation and the production of mid-ocean eddies. *Deep-Sea Res., 21*(7), 499 – 528.

Hamilton, P. (1990), Deep currents in the Gulf of Mexico, *J. Phys. Oceanogr.*, *20*(7), 1087 – 1104.

Hamilton, P. (2007), Deep-current variability near the Sigsbee Escarpment in the Gulf of Mexico, *J. Phys. Oceanogr.*, *37*(3), 708 – 726, doi:10.1175/JPO2998.1.

Hamilton, P., and T. N. Lee (2005), Eddies and jets over the slope of the Northeast Gulf of Mexico, in *Circulation in the Gulf of Mexico: Observations and Models*, edited by W. Sturges and A. Lugo-Fernández, pp. 123-142, AGU, Washington, DC.

Hamilton, P., and A. Lugo-Fernández (2001), Observations of high speed deep currents in the northern Gulf of Mexico, *Geophys. Res. Lett.*, *28*(14), 2867 – 2870.

Hetland, R., Y. Hsueh, and D. Yuan (2001), On the decay of a baroclinic jet flowing along a continental slope, *J. Geophys. Res.*, *106*(C9), 19797 – 19807.

Hofmann, E. E., and S. J. Worley (1986), An investigation of the circulation of the Gulf of Mexico, *J. Geophys. Res*., *91*(C12), 14221 – 14236.

Hurlburt, H. E., and J. D. Thompson (1980), A numerical study of Loop Current intrusion and eddy shedding, *J. Phys. Oceanogr.*, *10*(10), 1611 – 1651.

Ichiye, T. (1962), Circulation and water mass distribution in the Gulf of Mexico, *Geofis. Int.*, *2*, 47 – 76.

Inoue, M. (1982), Vertical structure of the low-frequency currents at Drake Passage, Ph.D. dissertation, Texas A&M University, College Station, TX.

Inoue, M. (1985), Modal decomposition of the low-frequency currents and baroclinic instability at Drake Passage, *J. Phys. Oceanogr.*, *15*(9), 1157 – 1181.

Kantha, L., J. Choi, K. J. Schaudt, and C. K. Cooper (2005), A regional data-assimilative model for operational use in the Gulf of Mexico, in *Circulation in the Gulf of Mexico: Observations and Models*, edited by W. Sturges and A. Lugo-Fernández, pp. 165-180, AGU, Washington, DC.

Klinck, J. M., E. E. Hofmann, R. C. Beardsley, B. Salihoglu, and S. Howard (2004), Water-mass properties and circulation on the west Antarctic Peninsula Continental Shelf in austral fall and winter 2001, *Deep-Sea Res. II, 51*(17-19), 1925 – 1946, doi:10.1016/j.dsr2.2004.08.001.

Kundu, P. K., J. S. Allen, and R. L. Smith (1975), Modal decomposition of the velocity field near the Oregon coast, *J. Phys. Oceanogr.*, *5*(4), 683 – 704.

Kuznetsov, L., M. Toner, A. D. Kirwan Jr., C. K. R. T. Jones, L.H. Kantha, and J.Choi (2002), The Loop Current and adjacent rings delineated by Lagrangian analysis of the near-surface flow, *J. Marine. Res.*, *60*(3), 405 – 429.

LeBlond, P. H., and L. A. Mysak (1978), *Waves in the Ocean*, Elsevier, New York.

Leben, R. R. (2005), Altimeter-derived Loop Current metrics, in *Circulation in the Gulf of Mexico: Observations and Models*, edited by W. Sturges and A. Lugo-Fernández, pp. 181-201, AGU, Washington, DC.

Lewis, J. K., and A. D. Kirwan, Jr. (1985), Some observation of ring topography and ring-ring interactions in the Gulf of Mexico, *J. Geophys. Res.*, *90*, 9017 – 9028.

Lewis, J. K., and A. D. Kirwan, Jr. (1987), Genesis of a Gulf of Mexico ring as determined from kinematic analyses, *J. Geophys. Res.*, *92*(C11), 11727 – 11740.

Lugo-Fernández, A. (2007), Is the Loop Current a chaotic oscillator, *J. Phys. Oceanogr.*, *37*(6), 1455 – 1469, doi:10.1175/JPO3066.1.

MacKinnon, J. A., and M. C. Gregg (2003), Shear and baroclinic energy flux on the summer New England Shelf, *J. Phys. Oceanogr.*, *33*(7), 1462 – 1475.

Maul, G. A. (1977), The annual cycle of the Gulf Loop Current part I: Observations during a one-year time series, *J. Marine. Res.*, *35*(1), 29 – 47.

McWilliams, J. C., and G. R. Flierl (1975), Quasi-geostrophic wave analyses: Dynamics and the analysis of MODE – 1, *Report of the MODE – 1 dynamics group*, 250 pp., Dept. of Meteorology, MIT.

McWilliams, J. C., and C. Y. Shen (1980), Mesoscale modal coupling, *J. Phys. Oceanogr.*, *10*(5), 741 – 752.

Morrison, J. M., and W. D. Nowlin, Jr. (1982), General distribution of water masses within the eastern Caribbean Sea during the winter of 1972 and fall of 1973, *J. Geophys. Res.*, *87*(C6), 4207 – 4229.

Morrison, J. M., W. J. Merrell, Jr., R. M. Key, and T. C. Key (1983), Property distributions and deep chemical measurements within the western Gulf of Mexico, *J. Geophys. Res.*, *88*(C4), 2601 – 2608.

Nof, D., and T. Pichevin (2001), The ballooning of outflows, *J. Phys. Oceanogr.*, *31*(10), 3045 – 3058.

Nowlin, W. D., Jr., and J. M. Hubertz (1972), Contrasting summer circulation patterns for the Eastern Gulf, in *Contributions on the Physical Oceanography of the Gulf of Mexico*, *Texas A&M Oceanographic Studies*, vol. 2, edited by L. R. A. Capurro and J. L. Reid, pp. 119 – 137, Gulf Press, Houston, TX.

Nowlin, W. D., Jr., and H. J. McLellan (1967), A characterization of the Gulf of Mexico waters in winter, *J. Mar. Res.*, *25*(1), 29 – 59.

Nowlin, W. D., Jr., A. E. Jochens, S. F. DiMarco, R. O. Reid, and M. K. Howard (2001), Deepwater physical oceanography reanalysis and synthesis of historical data: Synthesis Report, *OCS Study MMS 2001-064*, 528 pp., U.S. Dept. of the Interior, Minerals Management Service, Gulf of Mexico OCS Region, New Orleans, LA.

Oey, L. Y., and H. C. Lee (2002), Deep eddy energy and topographic Rossby waves in the Gulf of Mexico, *J. Phys. Oceanogr.*, *32*(12), 3499 – 3527.

Pichevin, T. and D. Nof (1997), The momentum imbalance paradox, *Tellus, Ser A., 49*(2), 298 – 319.

Pollard, R. T. (1970), On the generation by winds of inertial waves in the ocean, *Deep-Sea Res.*, *17*(4), 795 – 812.

Preisendorfer, R. W. (1988), *Principal Component Analysis in Meteorology and Oceanography*, Elsevier, Amsterdam.

Press, W. H., B. P. Flannery, S. .A. Teukolsky, and W. T. Vetterling (1986), *Numerical Recipies: The Art of Scientific Computing*, Cambridge UP, New York.

Sheinbaum, J., J. Candela, A. Badan, and J. Ochoa (2002), Flow structure and transport in the Yucatan Channel, *Geophys. Res. Lett.*, *29*(3), 1040, doi:10.1029/2001GL013990.

Schmitz, W. J. (1978), Observations of the vertical distribution of low-frequency kinetic energy in the western North Atlantic, *J. Mar. Res.*, *36*(2), 295 – 310.

Sturges, W. (1994), The frequency of ring separations from the Loop Current, *J. Phys. Oceanogr.*, *24*(7), 1647 – 1651.

Sturges, W., and R. R. Leben (2000), Frequency of ring separations from the Loop Current in the Gulf of Mexico: A revised estimate, *J. Phys. Oceanogr.*, *30*(7), 1814 – 1818.

Sturges W., J. C. Evans, S. Welsh, and W. Holland (1993), Separation of warm core rings in the Gulf of Mexico, *J. Phys. Oceanogr.*, *23*(2), 250 – 286.

Sturges, W., A. Lugo-Fernández, and M. D. Shargel (2005), Introduction to circulation in the Gulf of Mexico, in *Circulation in the Gulf of Mexico: Observations and Models*, edited by W. Sturges and A. Lugo-Fernández, pp. 1-10, AGU, Washington, DC.

Torrence, C., and G. P. Compo (1998), A practical guide to wavelet analysis, *Bull. Amer. Meteor. Soc., 79*(1), 61 – 78.

Vidal, V. M. V., F. V. Vidal, and J. M. Pérez-Molero (1992), Collision of a Loop Current anticyclonic ring against the continental shelf slope of the western Gulf of Mexico, *J. Geophys. Res.*, *97*(C2), 2155 – 2172.

Vukovich, F. M. (1986), Aspects of the behavior of cold perturbations in the Eastern Gulf of Mexico: A case study, *J. Phys. Oceanogr.*, *16*(1), 175 – 188.

Vukovich, F. M. (1995), An updated evaluation of the Loop Current's eddy-shedding frequency, *J. Geophys. Res.*, *100*(C5), 8655 – 8659.

Vukovich, F. M., and G. A. Maul (1985), Cyclonic eddies in the Eastern Gulf of Mexico, *J. Phys. Oceanogr.*, *15*(1), 105 – 117.

Walker, N. D. (2005), Wind and eddy-related shelf/slope circulation processes and coastal upwelling in the northwestern Gulf of Mexico, in *Circulation in the Gulf of Mexico: Observations and Models*, edited by W. Sturges and A. Lugo-Fernández, pp. 295-313, AGU, Washington, DC.

Walker, N., S. Myint, A. Babin, and A. Haag (2003), Advances in satellite radiometry for the surveillance of surface temperatures, ocean eddies and upwelling processes in the Gulf of Mexico using GOES-8 measurements during summer, *Geophys. Res. Lett.*, *30*(16), 1854, doi:10.1029/2003GL017555.

Welsh, S. E., and M. Inoue (2000), Loop Current rings and the deep circulation in the Gulf of Mexico, *J. Geophys. Res.*, *105*(C7), 16951 – 16959.

Wunsch, C. (1997), The vertical partition of oceanic horizontal kinetic energy, *J. Phys. Oceanogr.*, *27*(8), 1770 – 1794.

Wyrtki, K., L. Magaard, and J. Hager (1976), Eddy energy in the oceans, *J. Geophys. Res.*, *81*(15), 2641 – 2646.

Xing, J. X., and A. M. Davies (2005), Nonlinear interaction between wind-forced currents and near-inertial oscillations and internal waves in the nearshore frontal regions, *J. Geophys. Res.*, *110*(C5), C05003, doi:10.1029/2004JC002579.

Zavala-Hidalgo, J., S. L. Morey, and J. J. O'Brien (2003), Cyclonic eddies northeast of the Campeche Bank from altimetry data, *J. Phys. Oceanogr.*, *33*(3), 623 – 629.

APPENDIX A

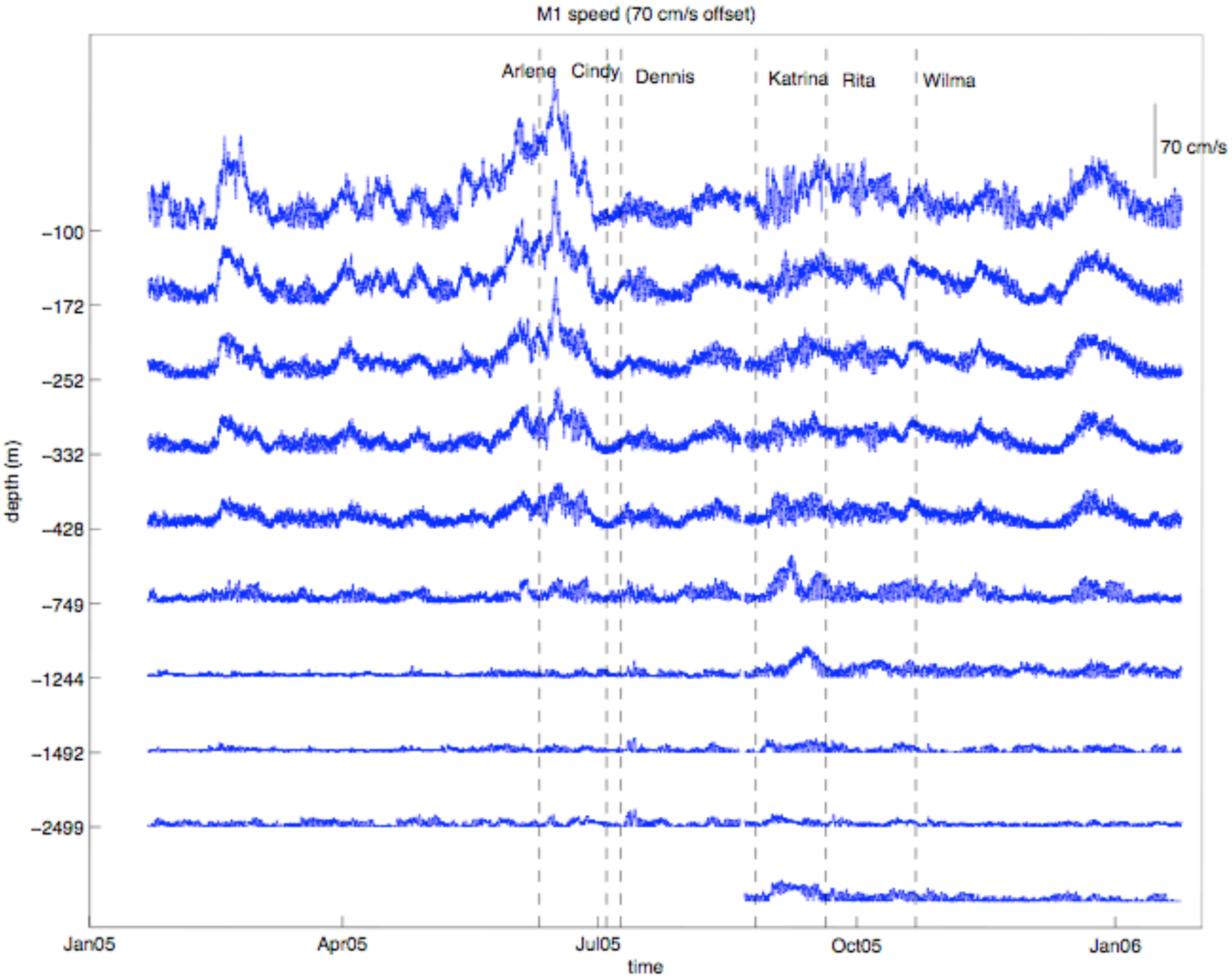

Figure A-1. Gap-filled, gridded current speed from five moored ADCP depths and moored current meters for deployments 1 and 2 at mooring M1. Time periods when tropical storms traversed the Gulf are indicated by vertical dotted lines.

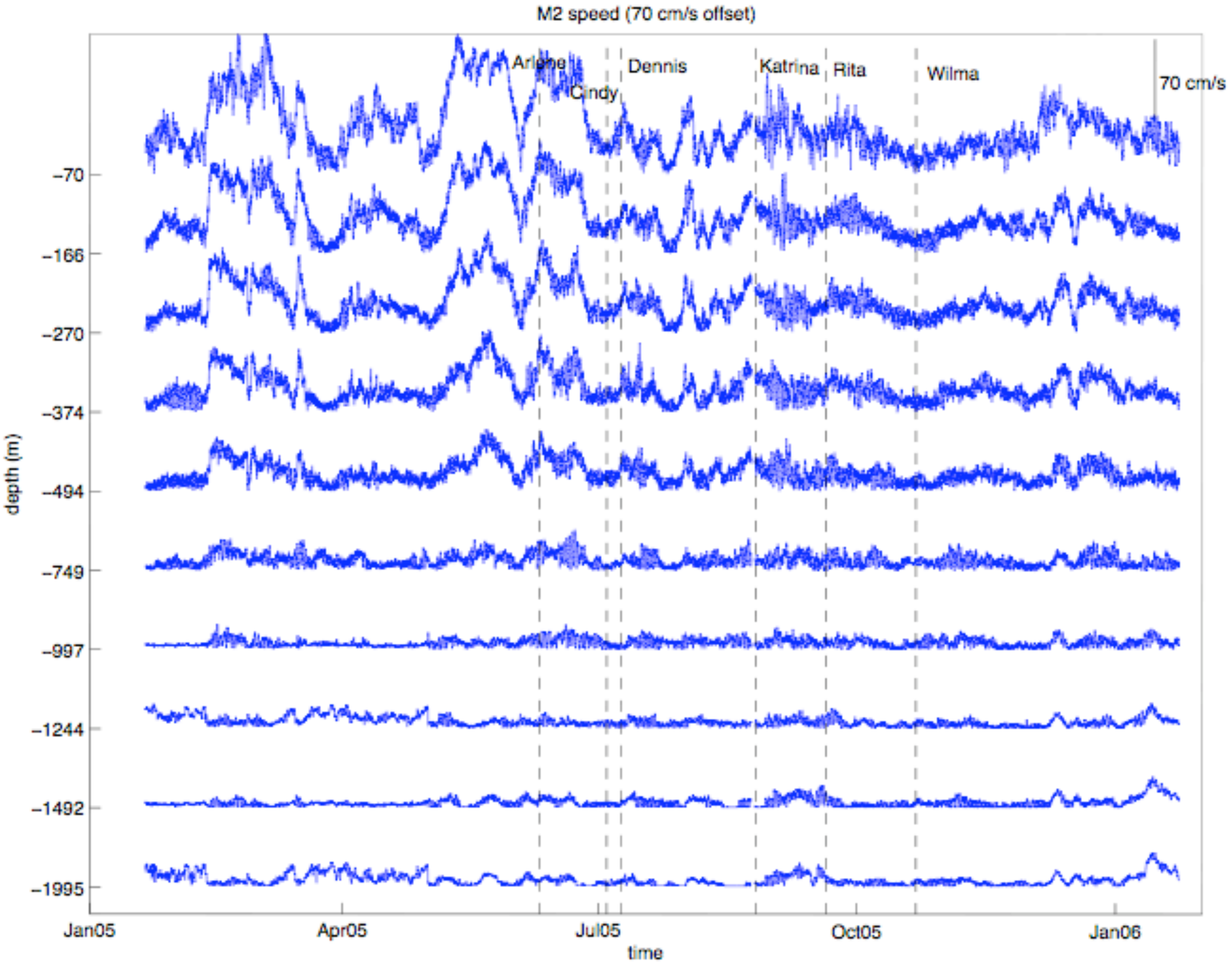

Figure A-2. Gap-filled, gridded current speed from five moored ADCP depths and moored current meters for deployments 1 and 2 at mooring M2. Time periods when tropical storms traversed the Gulf are indicated by vertical dotted lines.

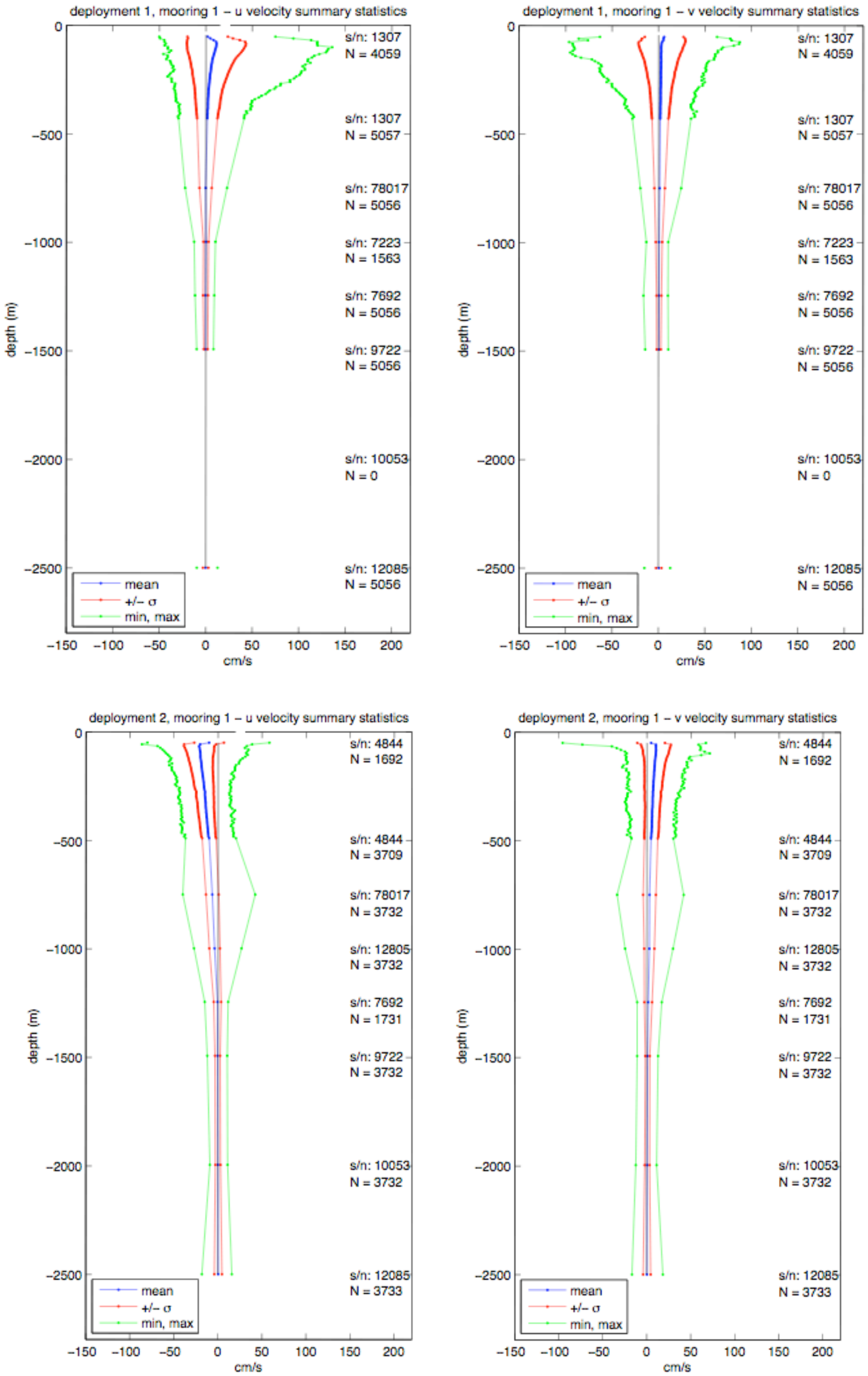

Figure A-3. Vertical profiles of record-length mean, standard deviation, minimum, and maximum velocity components for mooring M1 (left: east-west component; right: north-south component). Top row: Deployment 1. Bottom row: Deployment 2.

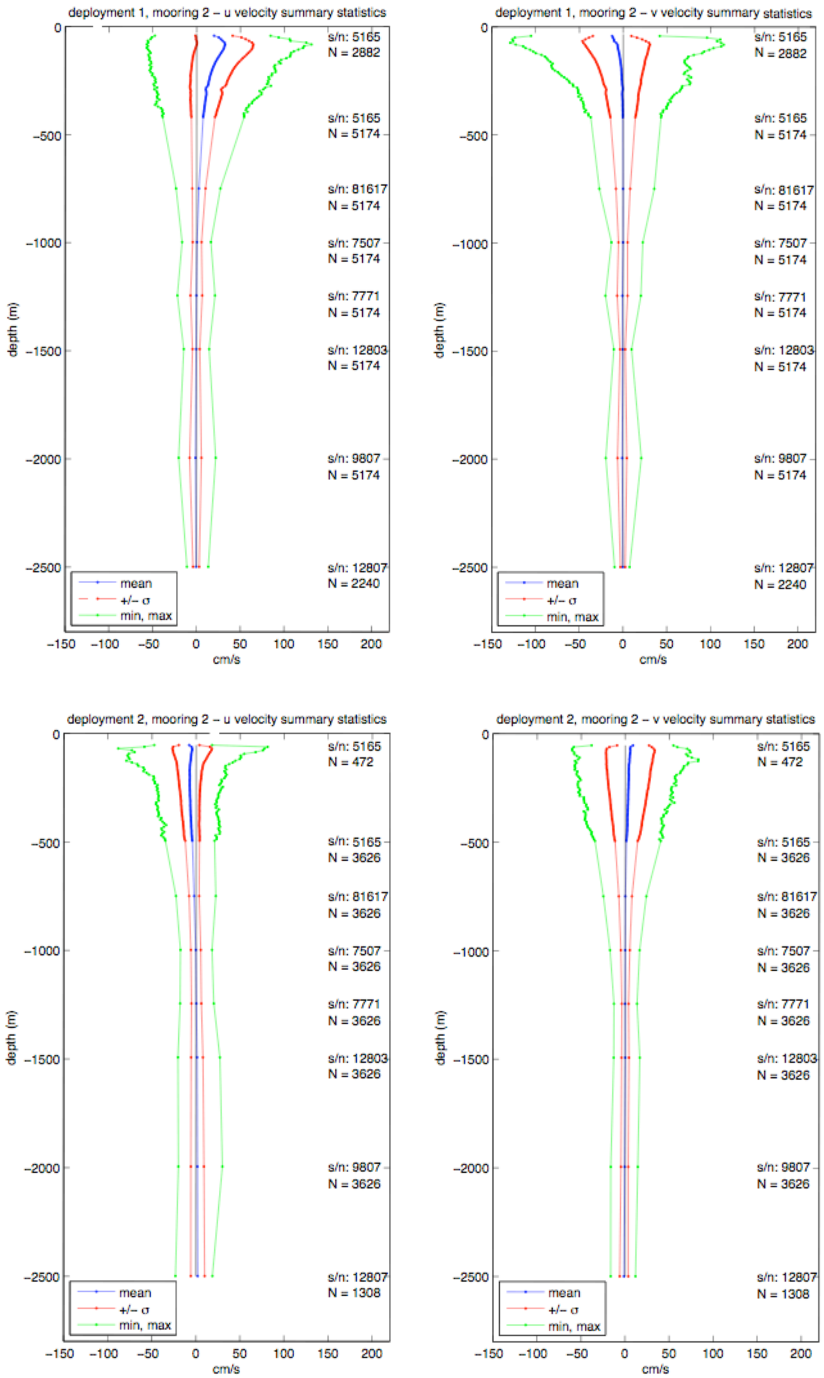

Figure A-4. Vertical profiles of record-length mean, standard deviation, minimum, and maximum velocity components for mooring M2 (left: east-west component; right: north-south component). Top row: Deployment 1. Bottom row: Deployment 2.

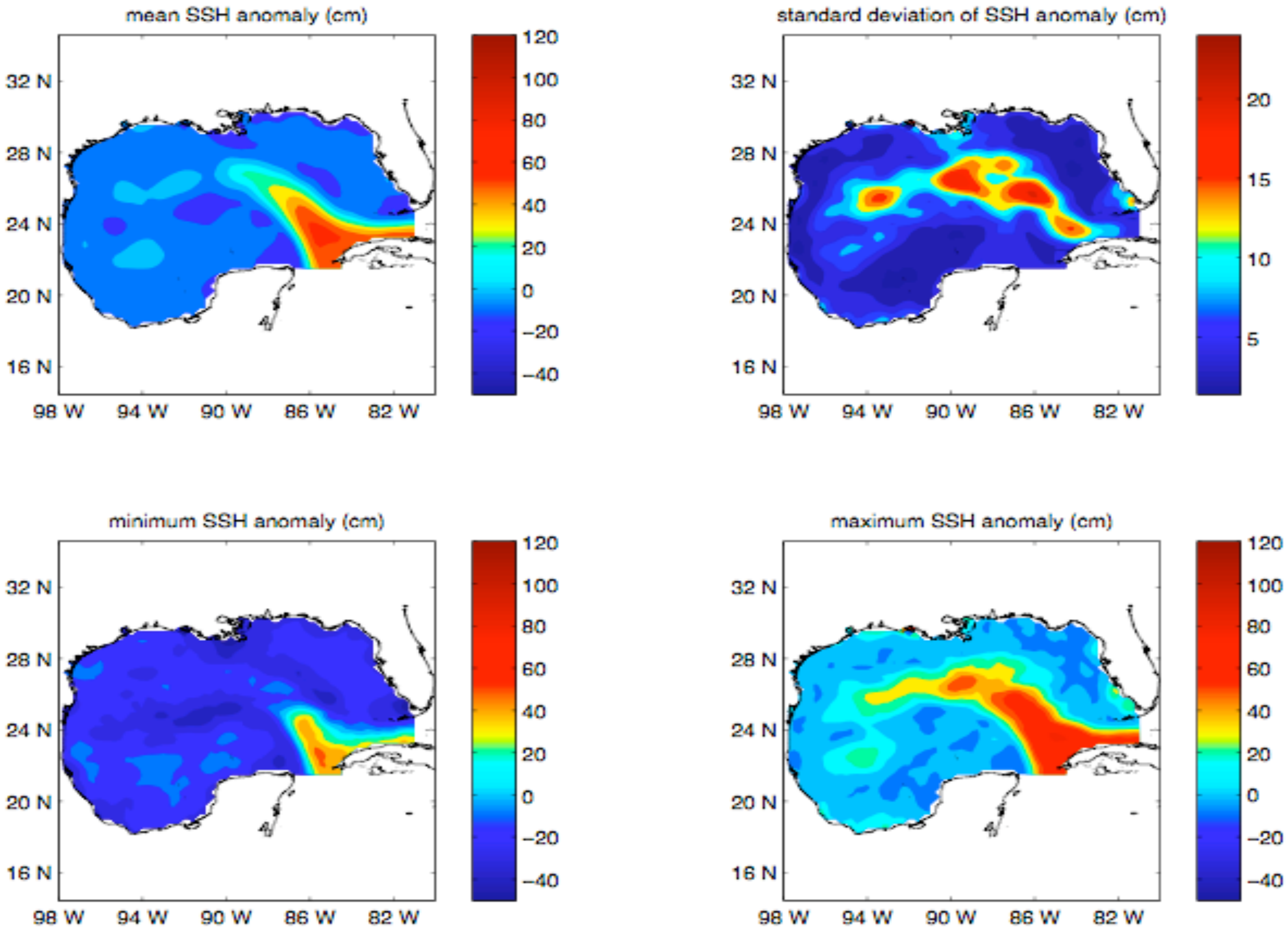

Figure A-5. (Clockwise from top left) mean, standard deviation, maximum, and minimum of altimeter derived sea surface height anomaly in centimeters (from Leben) in the Gulf of Mexico between January 1, 2005 and January 31, 2006.

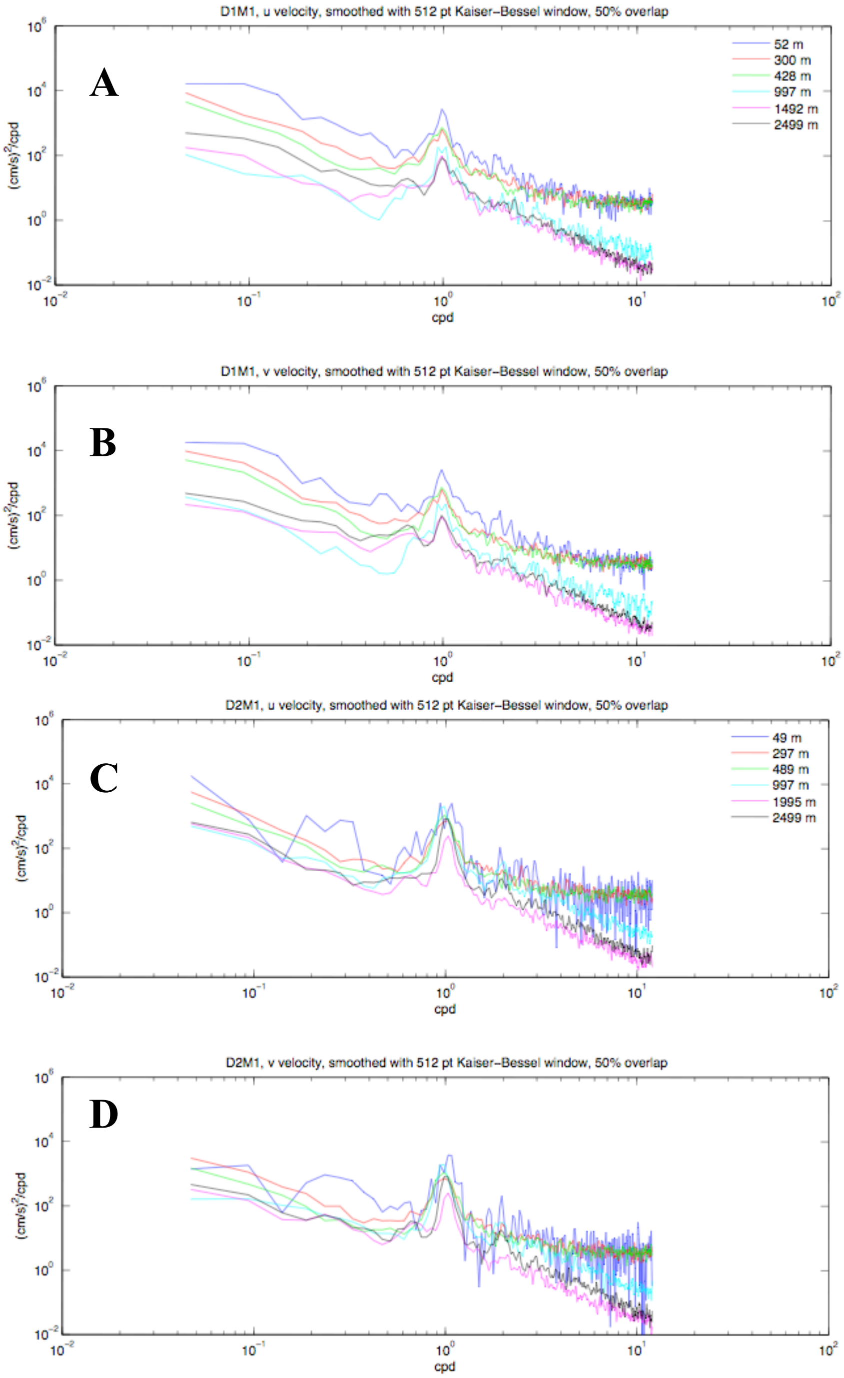

Figure A-6. Panels A and B give power spectral density of detided, gap-filled *u* and *v*-velocity respectively at 6 depths at mooring 1 from deployment 1. Panels C and D give power spectral density of *u* and *v*-velocity respectively at 6 depths at mooring 1 from deployment 2.

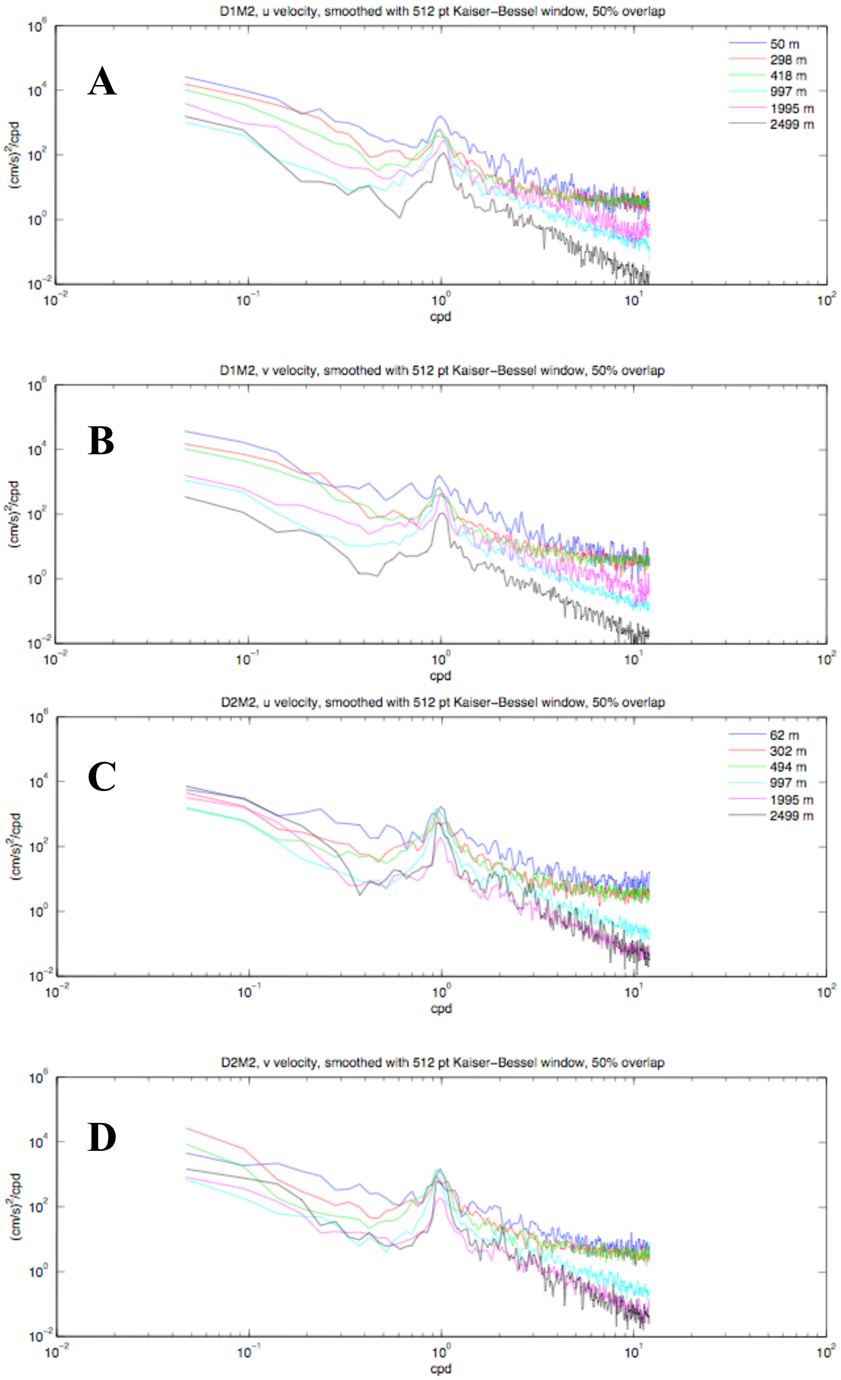

Figure A-7. Panels A and B give power spectral density of detided, gap-filled *u* and *v*-velocity respectively at 6 depths at mooring 2 from deployment 1. Panels C and D give power spectral density of *u* and *v*-velocity respectively at 6 depths at mooring 2 from deployment 2.

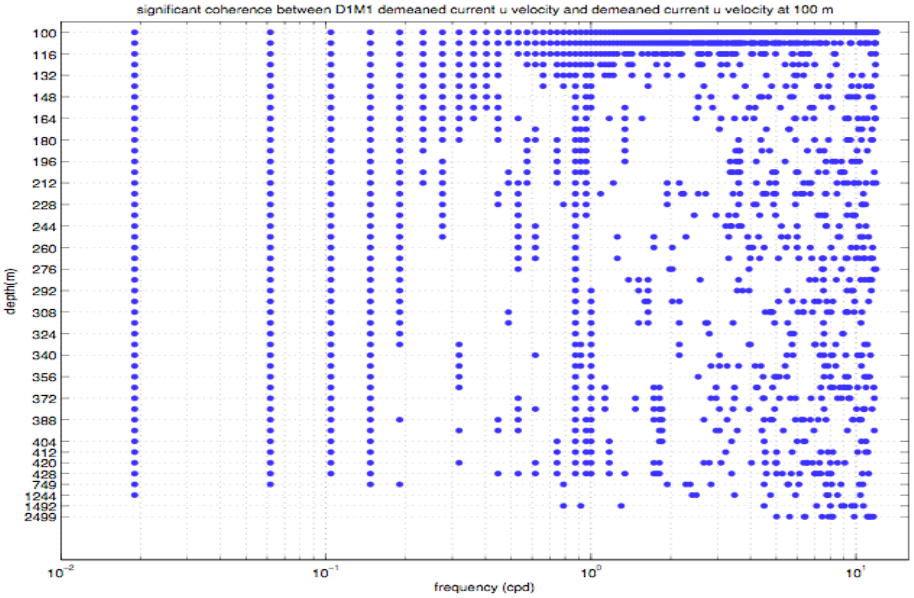

Figure A-8. Significant coherence (at 5% level) between mooring M1 deployment 1 current *u*-velocity component by depth relative to the upper-most time-series.

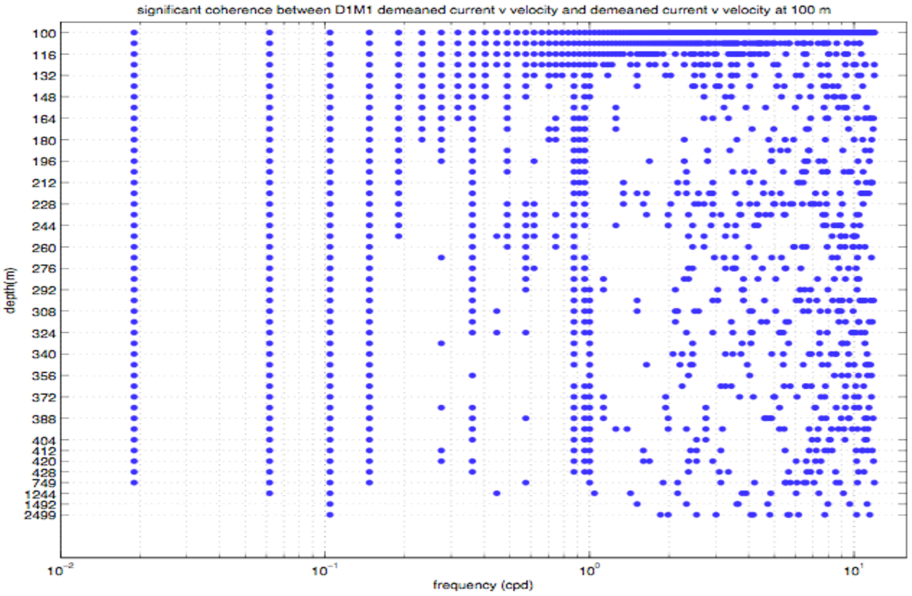

Figure A-9. Significant coherence (at 5% level) between mooring M1 deployment 1 current *v*-velocity component by depth relative to the upper-most time-series.

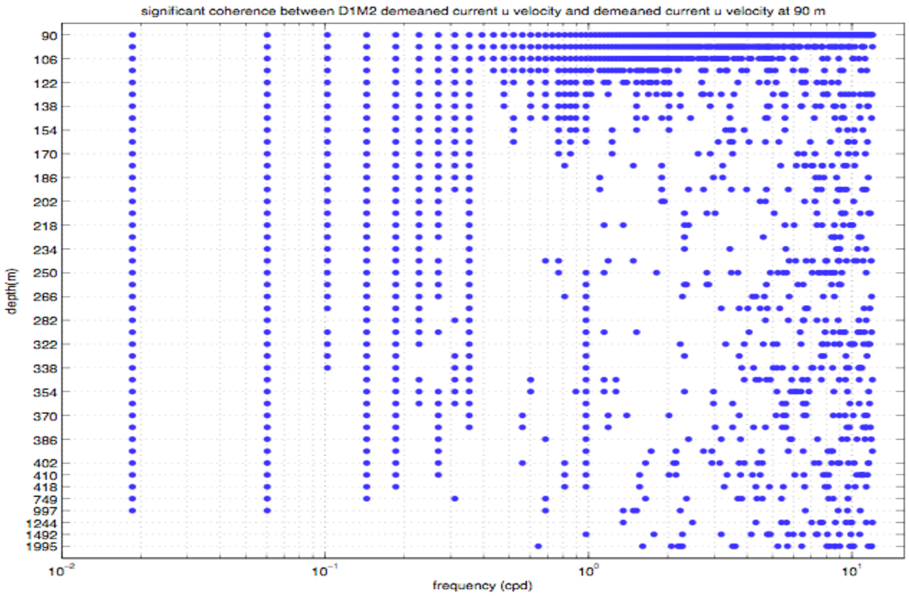

Figure A-10. Significant coherence (at 5% level) between mooring M2 deployment 1 current *u*-velocity component by depth relative to the upper-most time-series.

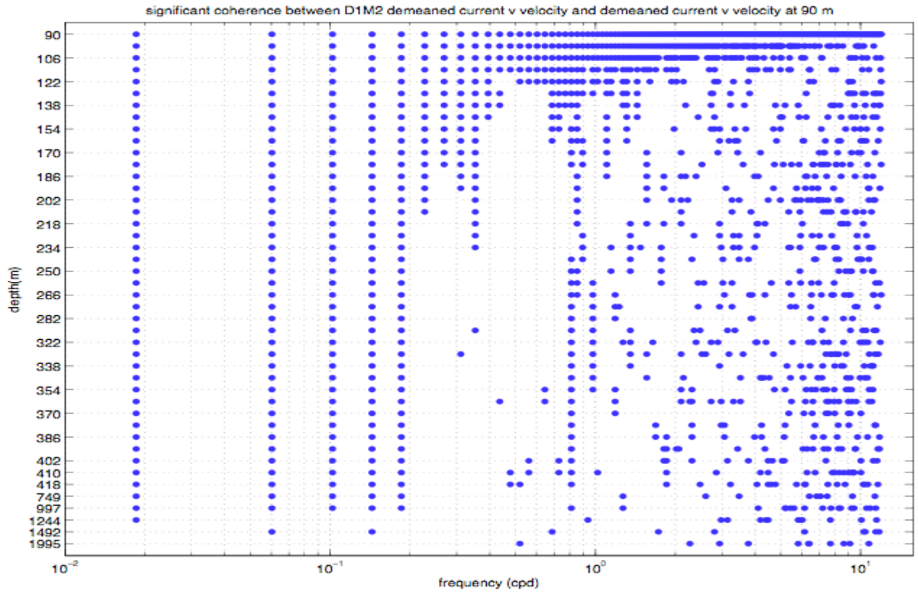

Figure A-11. Significant coherence (at 5% level) between mooring M2 deployment 1 current *v*-velocity component by depth relative to the upper-most time-series.

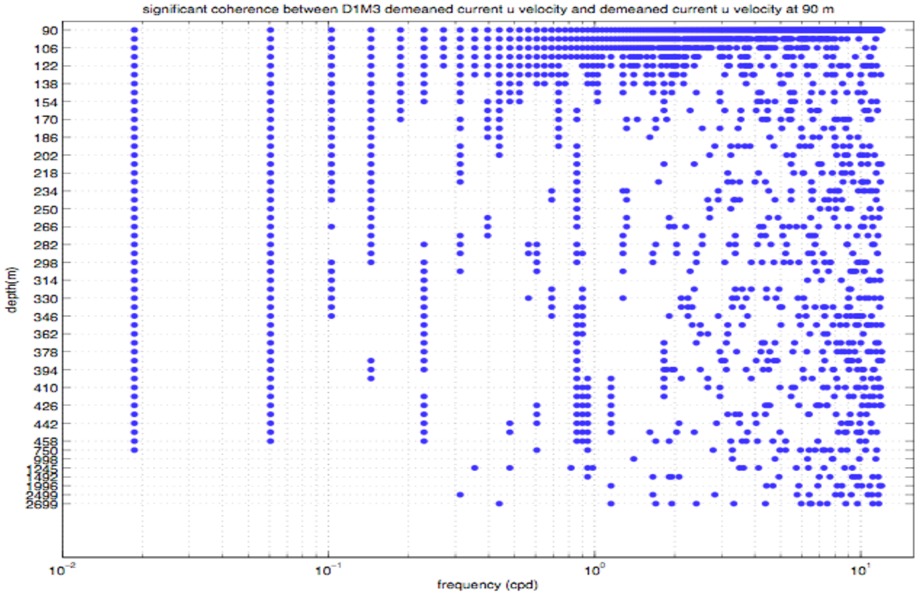

Figure A-12. Significant coherence (at 5% level) between mooring M3 deployment 1 current *u*-velocity component by depth relative to the upper-most time-series.

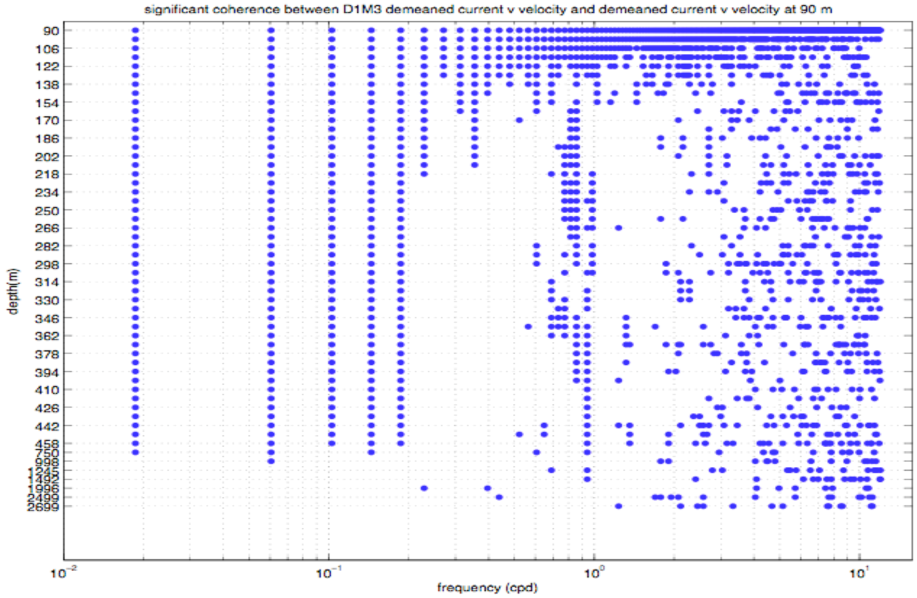

Figure A-13. Significant coherence (at 5% level) between mooring M3 deployment 1 current *v*-velocity component by depth relative to the upper-most time-series.

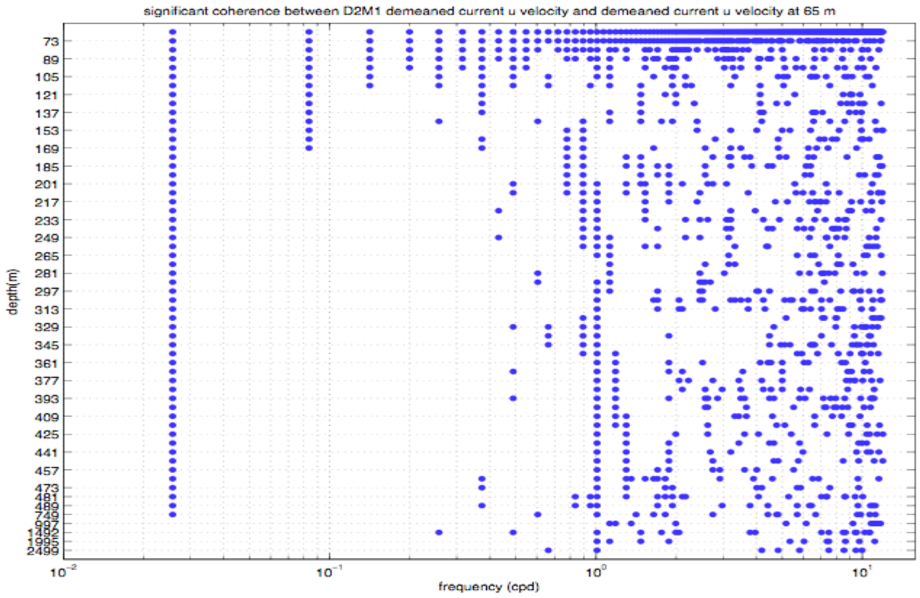

Figure A-14. Significant coherence (at 5% level) between mooring M1 deployment 2 current *u*-velocity component by depth relative to the upper-most time-series.

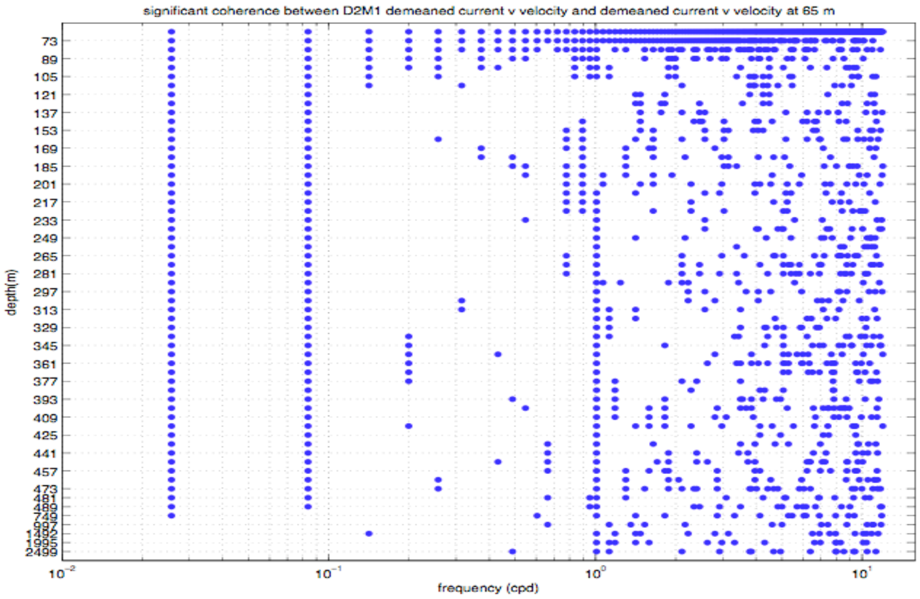

Figure A-15. Significant coherence (at 5% level) between mooring M1 deployment 2 current *v*-velocity component by depth relative to the upper-most time-series.

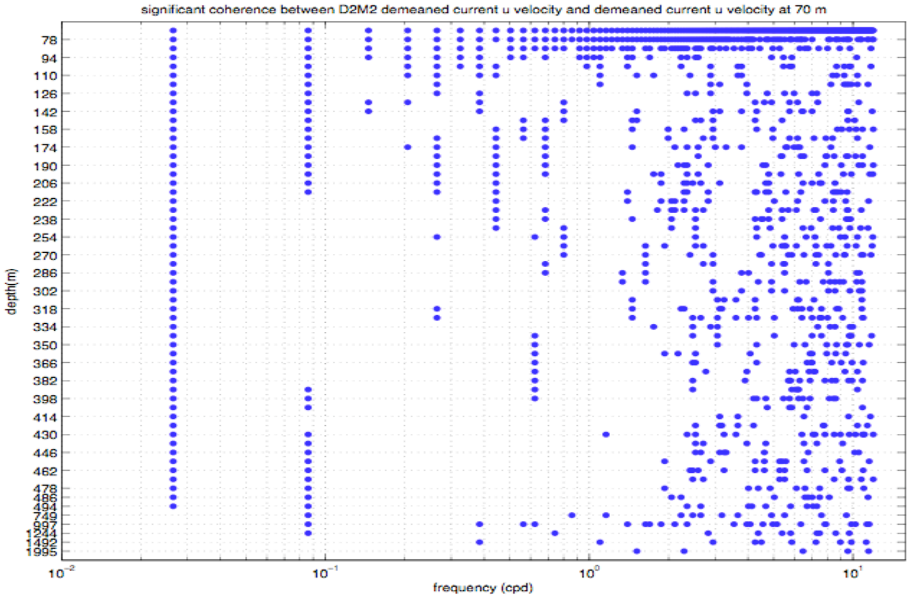

Figure A-16. Significant coherence (at 5% level) between mooring M2 deployment 2 current *u*-velocity component by depth relative to the upper-most time-series.

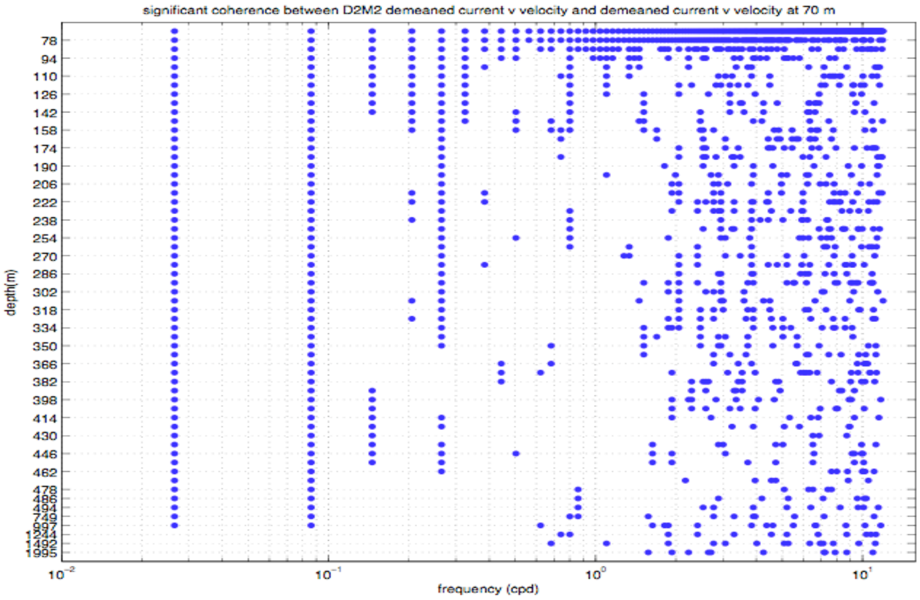

Figure A-17. Significant coherence (at 5% level) between mooring M2 deployment 2 current *v*-velocity component by depth relative to the upper-most time-series.

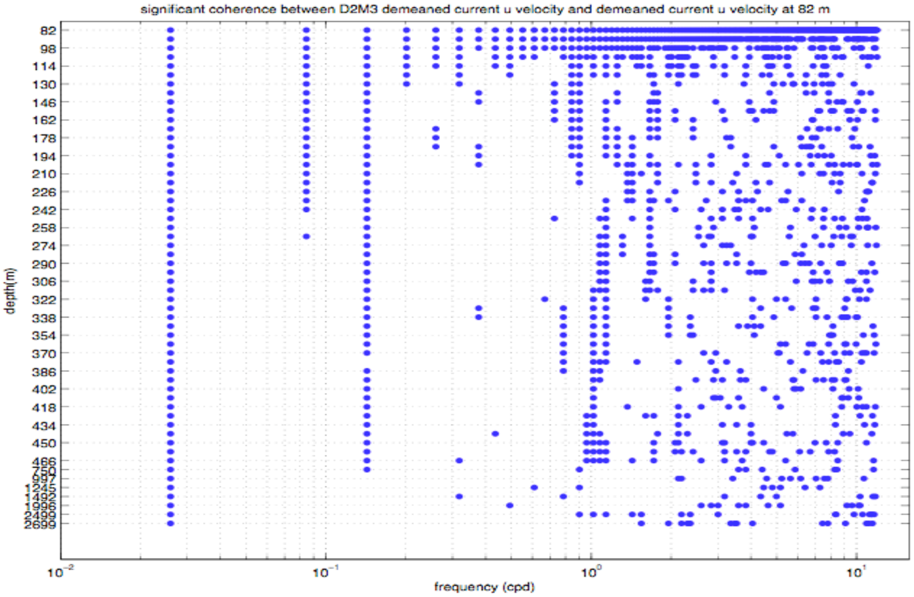

Figure A-18. Significant coherence (at 5% level) between mooring M3 deployment 2 current *u*-velocity component by depth relative to the upper-most time-series.

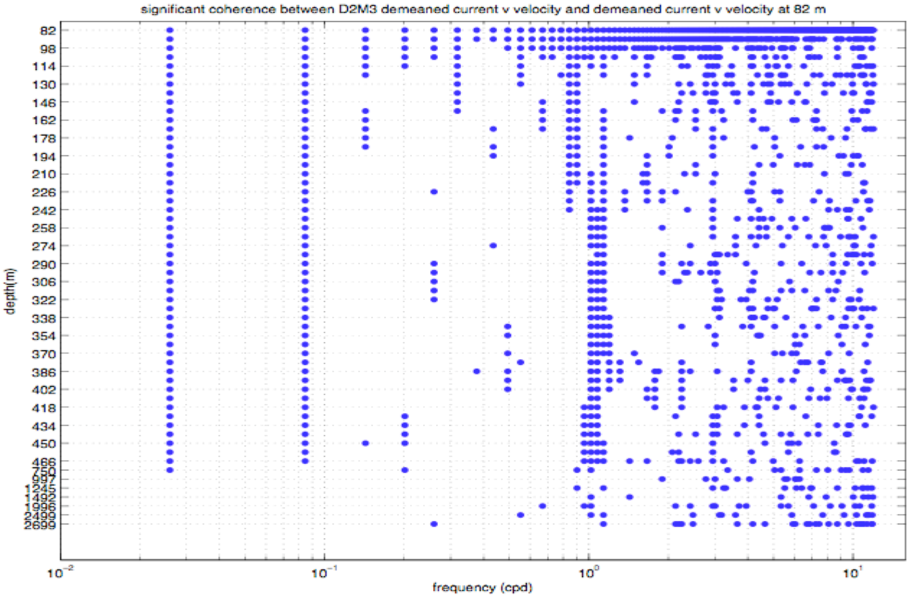

Figure A-19. Significant coherence (at 5% level) between mooring M3 deployment 2 current *v*-velocity component by depth relative to the upper-most time-series.

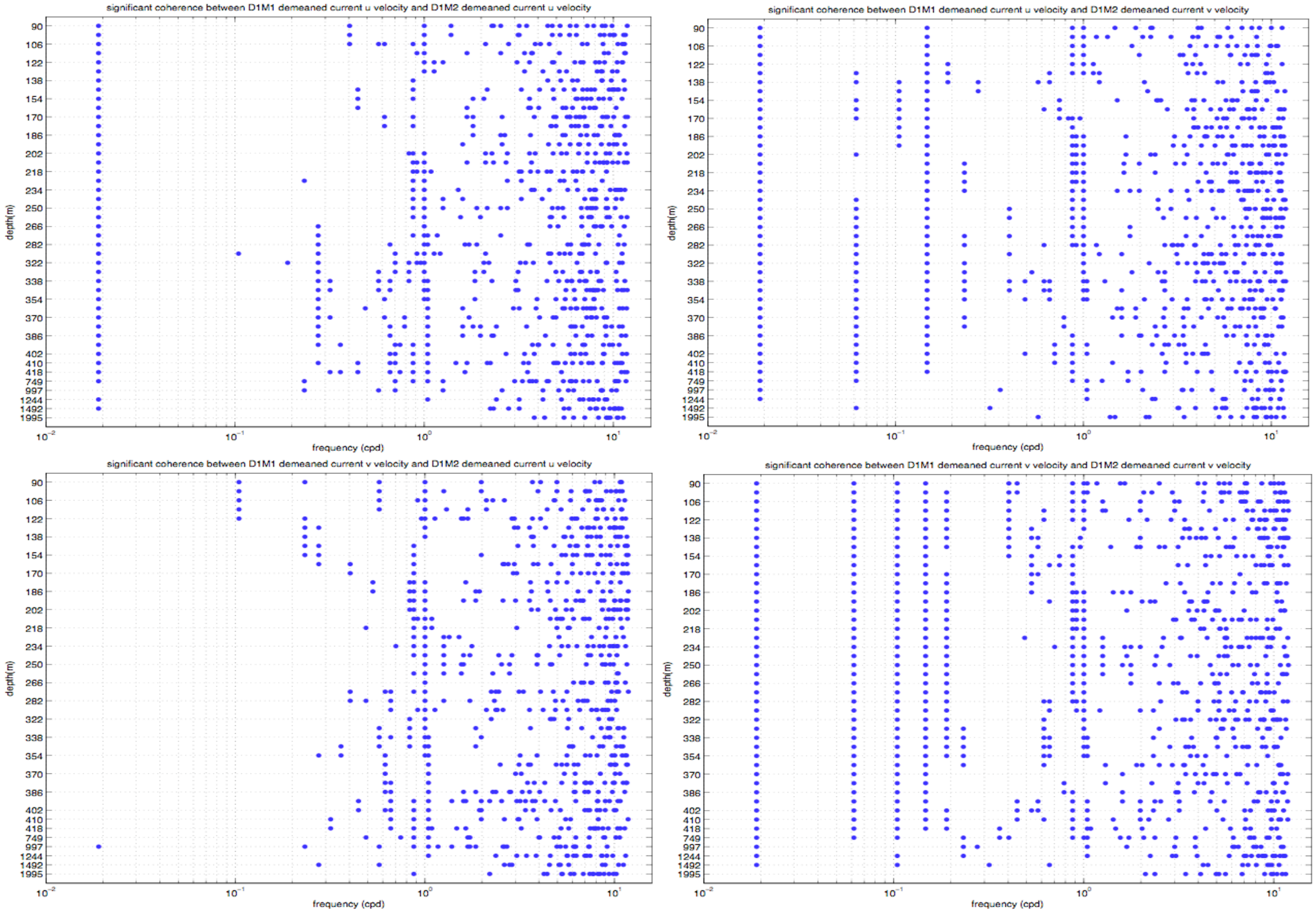

Figure A-20. (Clockwise from top left) Significant coherence (at 5% level) between D1M1 *u*-velocity and D1M2 *u*-velocity, D1M1 *u*-velocity and D1M2 *v*-velocity, D1M1 *v*-velocity and D1M2 *u*-velocity, and D1M1 *v*-velocity and D1M2 *v*-velocity by depth.

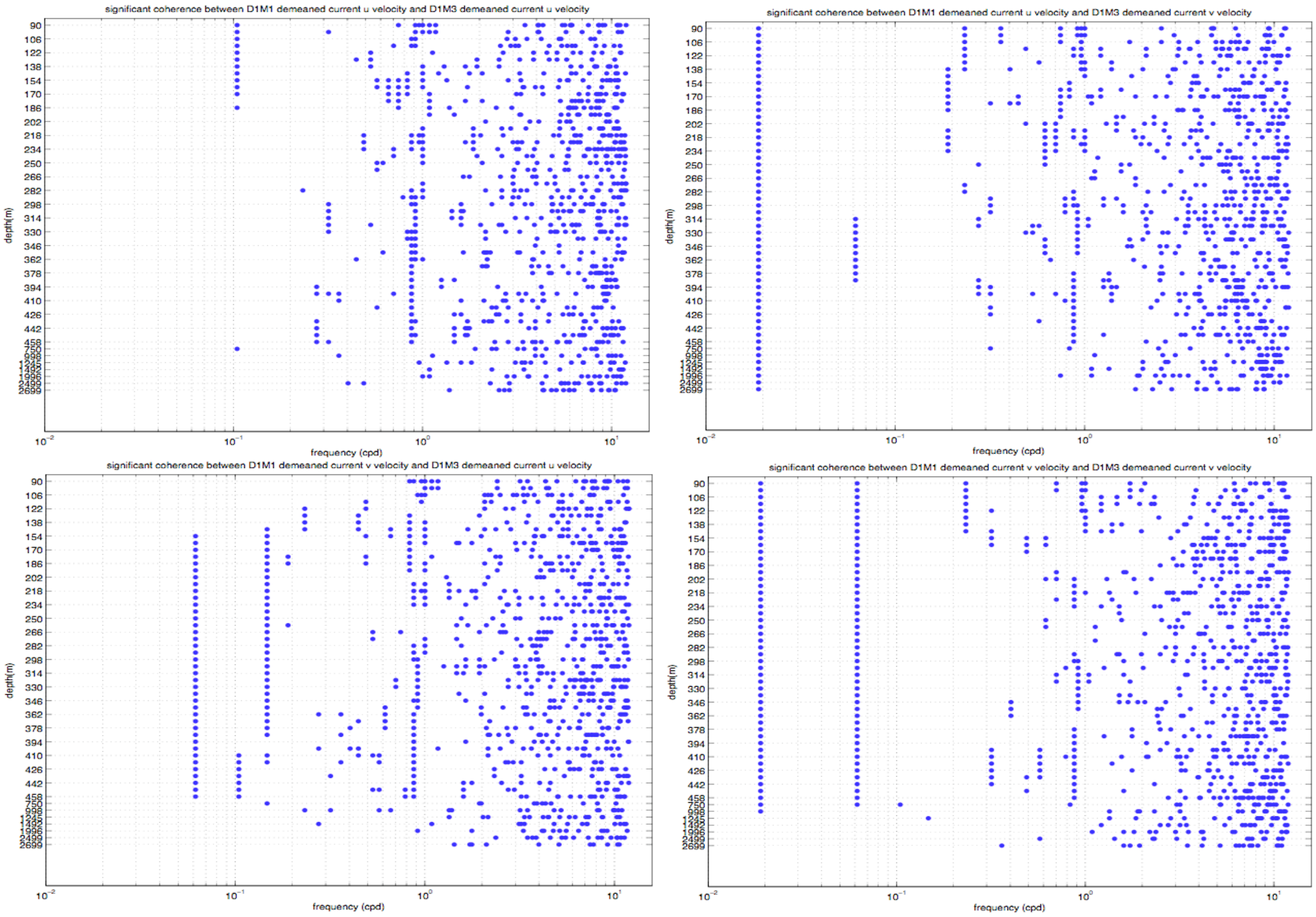

Figure A-21. (Clockwise from top left) Significant coherence (at 5% level) between D1M1 *u*-velocity and D1M3 *u*-velocity, D1M1 *u*-velocity and D1M3 *v*-velocity, D1M1 *v*-velocity and D1M3 *u*-velocity, and D1M1 *v*-velocity and D1M3 *v*-velocity by depth.

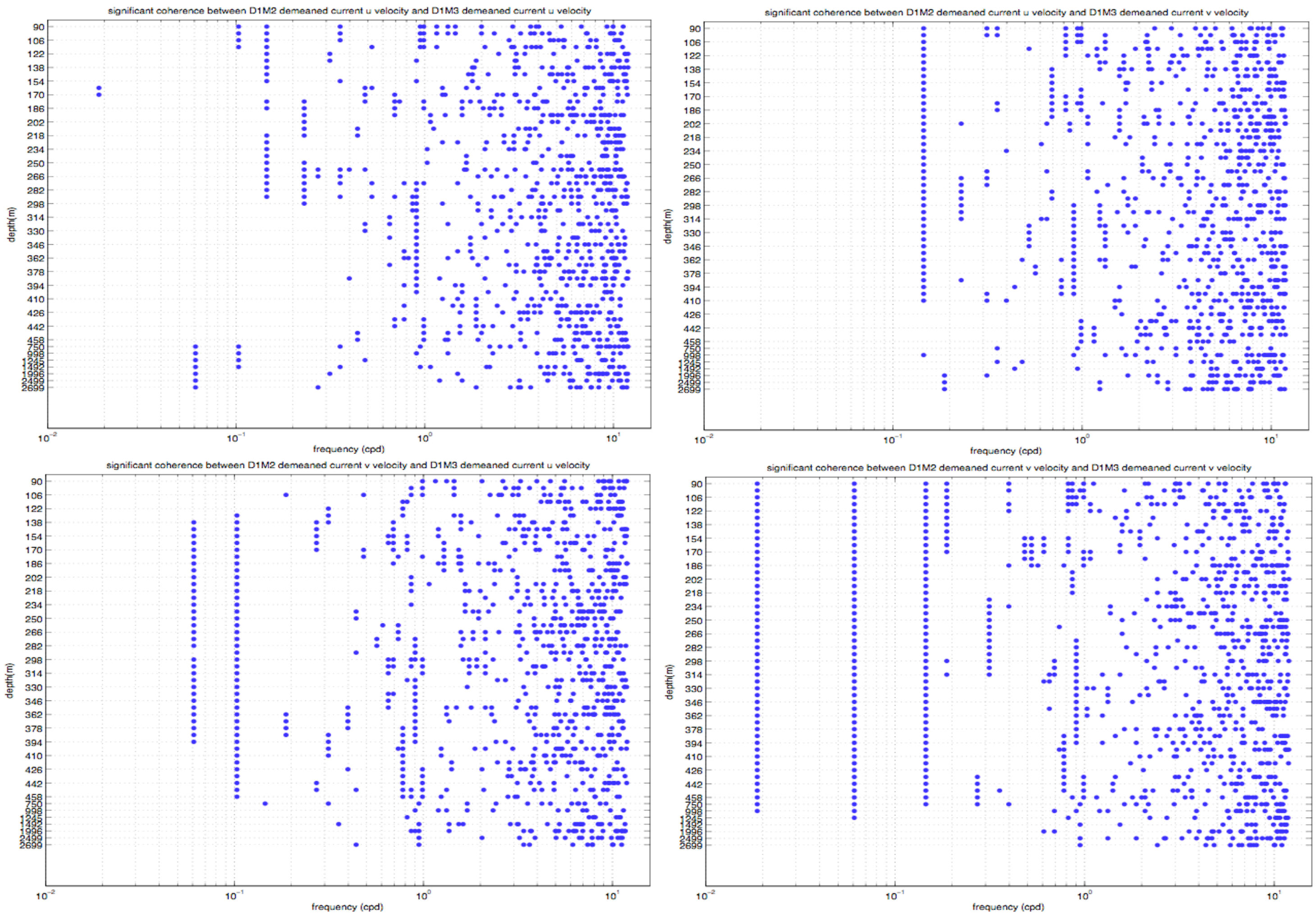

Figure A-22. (Clockwise from top left) Significant coherence (at 5% level) between D1M2 *u*-velocity and D1M3 *u*-velocity, D1M2 *u*-velocity and D1M3 *v*-velocity, D1M2 *v*-velocity and D1M3 *u*-velocity, and D1M2 *v*-velocity and D1M3 *v*-velocity by depth.

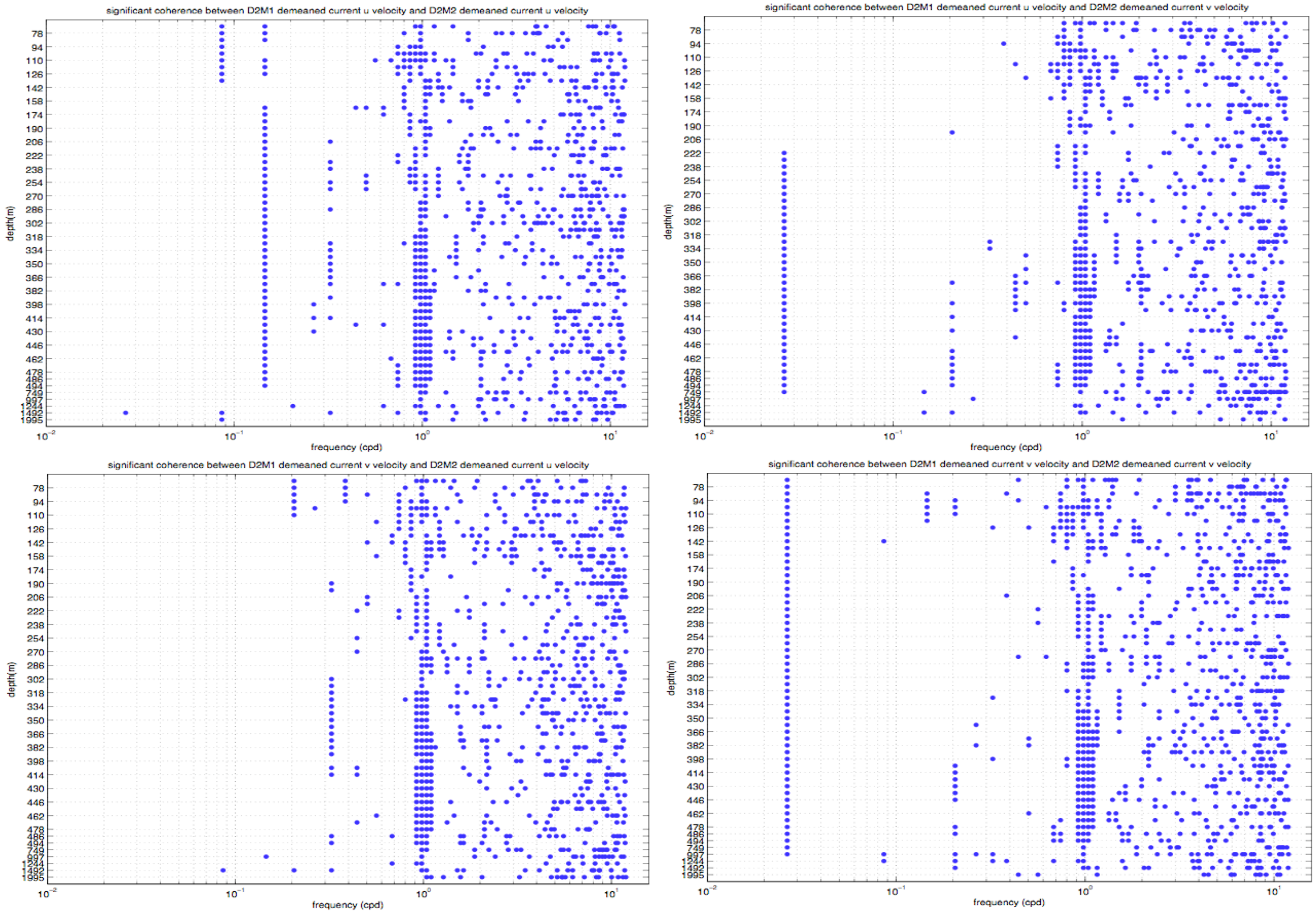

Figure A-23. (Clockwise from top left) Significant coherence (at 5% level) between D2M1 *u*-velocity and D2M2 *u*-velocity, D2M1 *u*-velocity and D2M2 *v*-velocity, D2M1 *v*-velocity and D2M2 *u*-velocity, and D2M1 *v*-velocity and D2M2 *v*-velocity by depth.

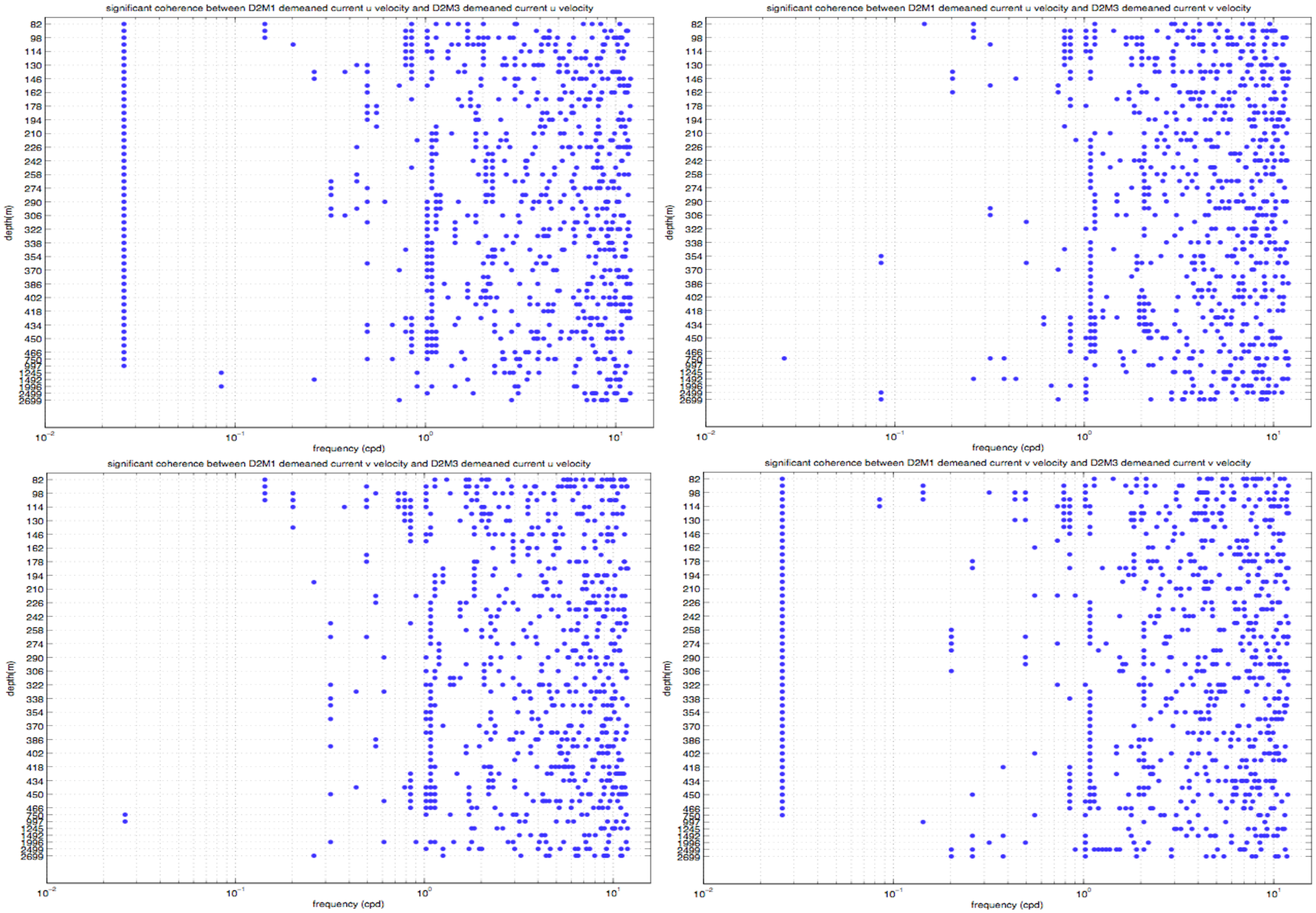

Figure A-24. (Clockwise from top left) Significant coherence (at 5% level) between D2M1 *u*-velocity and D2M3 *u*-velocity, D2M1 *u*-velocity and D2M3 *v*-velocity, D2M1 *v*-velocity and D2M3 *u*-velocity, and D2M1 *v*-velocity and D2M3 *v*-velocity by depth.

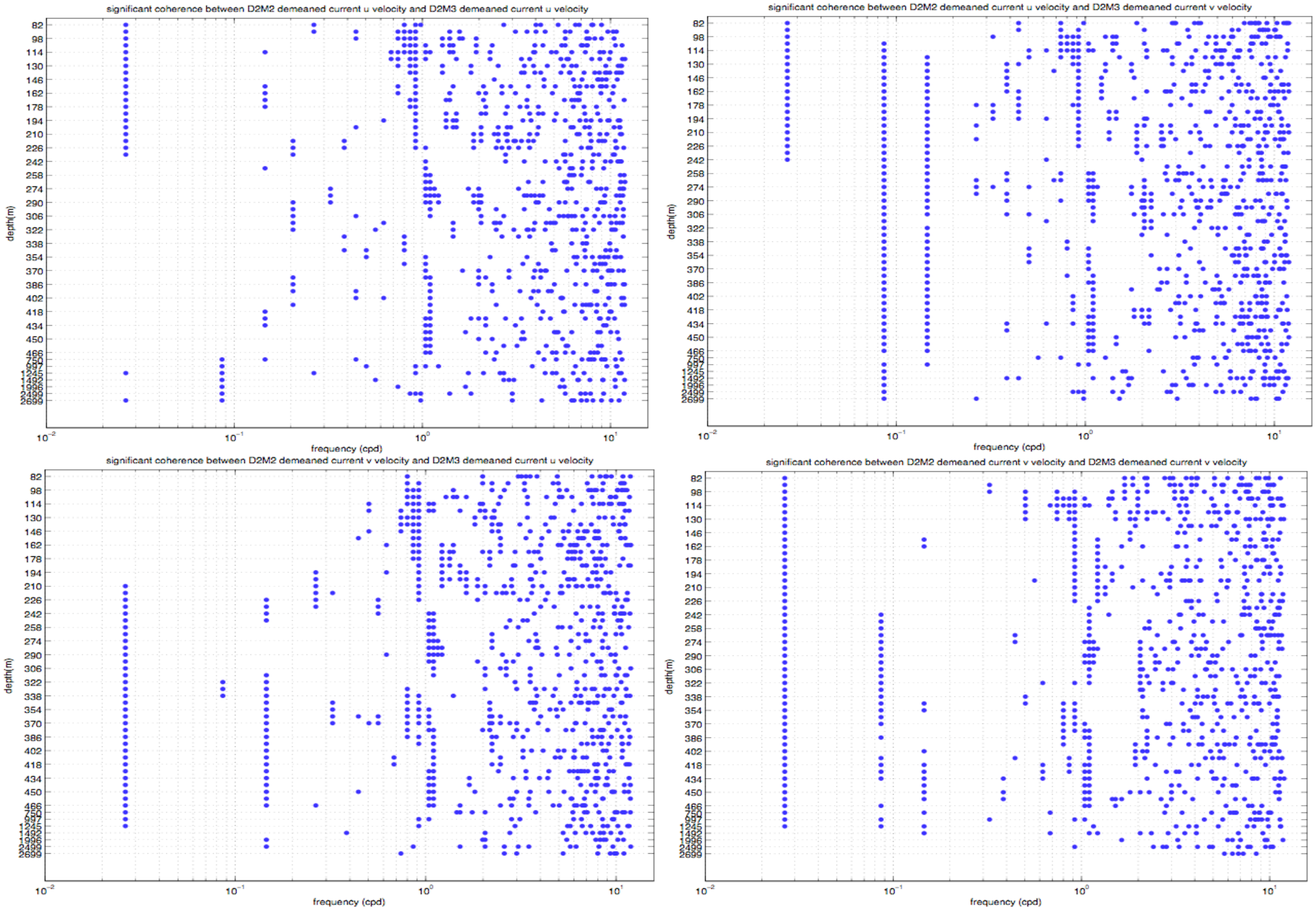

Figure A-25. (Clockwise from top left) Significant coherence (at 5% level) between D2M2 *u*-velocity and D2M3 *u*-velocity, D2M2 *u*-velocity and D2M3 *v*-velocity, D2M2 *v*-velocity and D2M3 *u*-velocity, and D2M2 *v*-velocity and D2M3 *v*-velocity by depth.

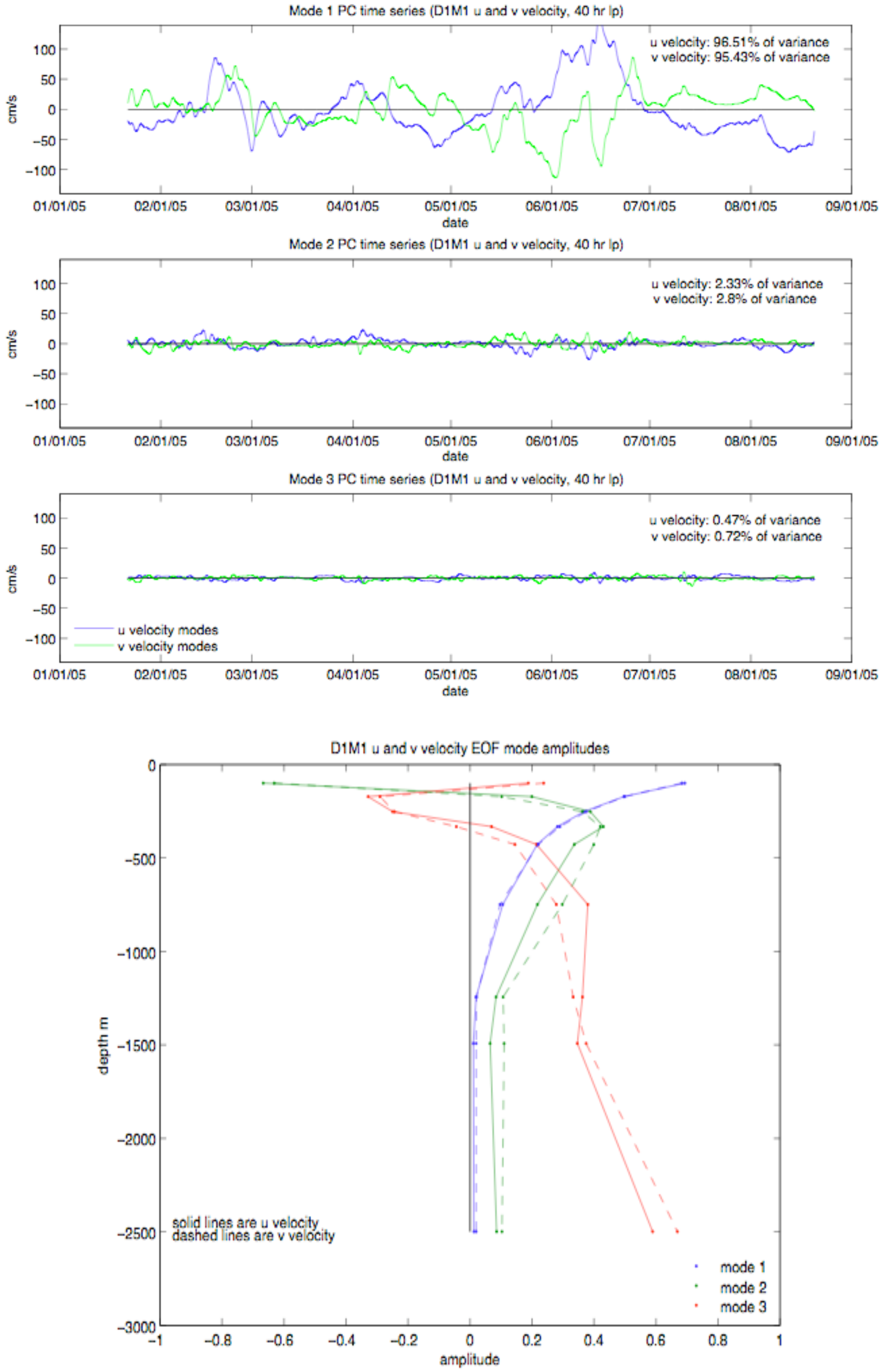

Figure A-26. Vertical EOFs of east-west and north-south current velocity at mooring M1 during deployment 1. Top three panels: Principal component (PC) time-series of first three empirical modes. Bottom panel: Amplitudes of empirical modes corresponding to PC time-series.

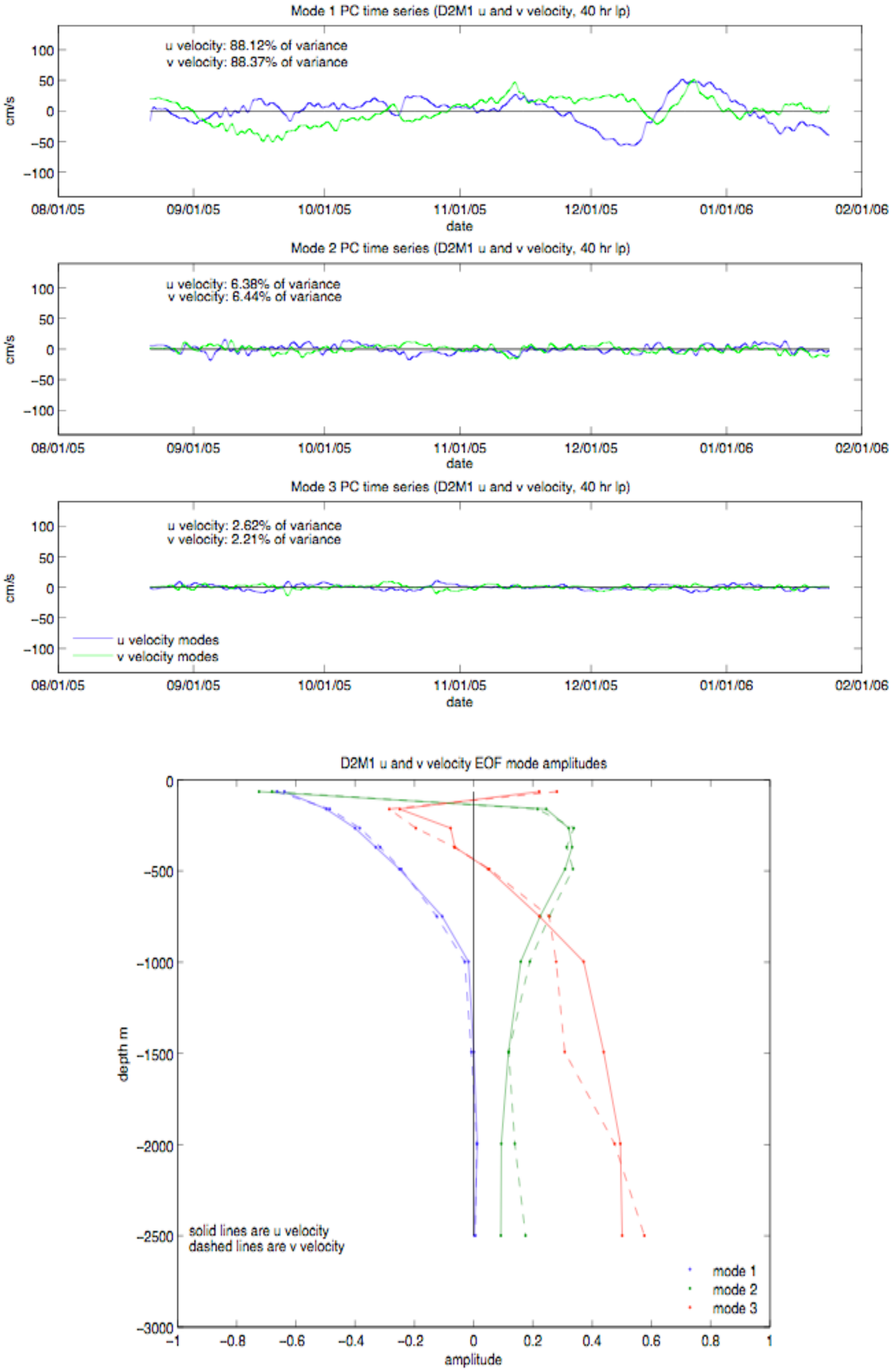

Figure A-27. Vertical EOFs of east-west and north-south current velocity at mooring M1 during deployment 2. Top three panels: Principal component (PC) time-series of first three empirical modes. Bottom panel: Amplitudes of empirical modes corresponding to PC time-series.

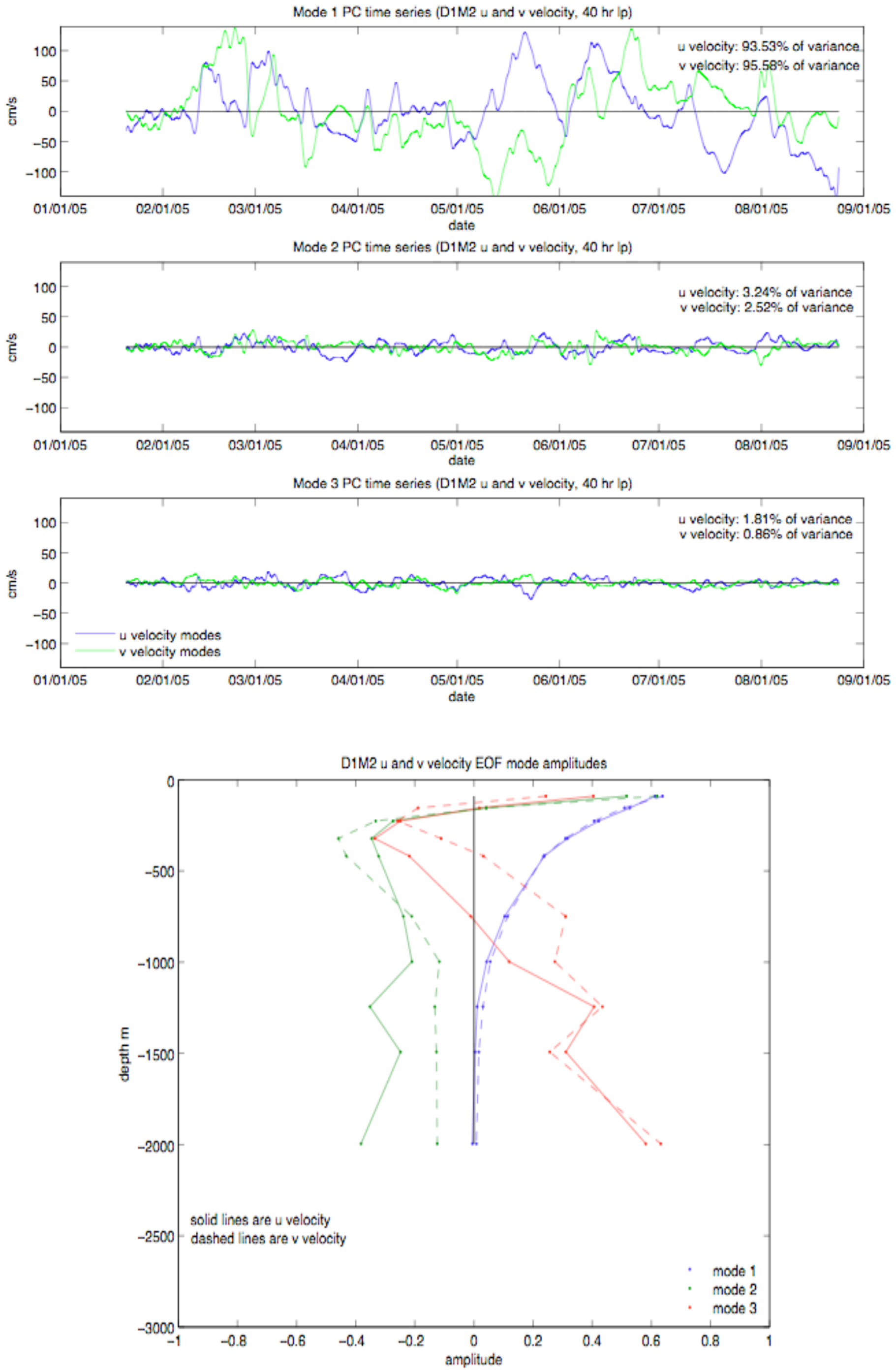

Figure A-28. Vertical EOFs of east-west and north-south current velocity at mooring M2 during deployment 1. Top three panels: Principal component (PC) time-series of first three empirical modes. Bottom panel: Amplitudes of empirical modes corresponding to PC time-series.

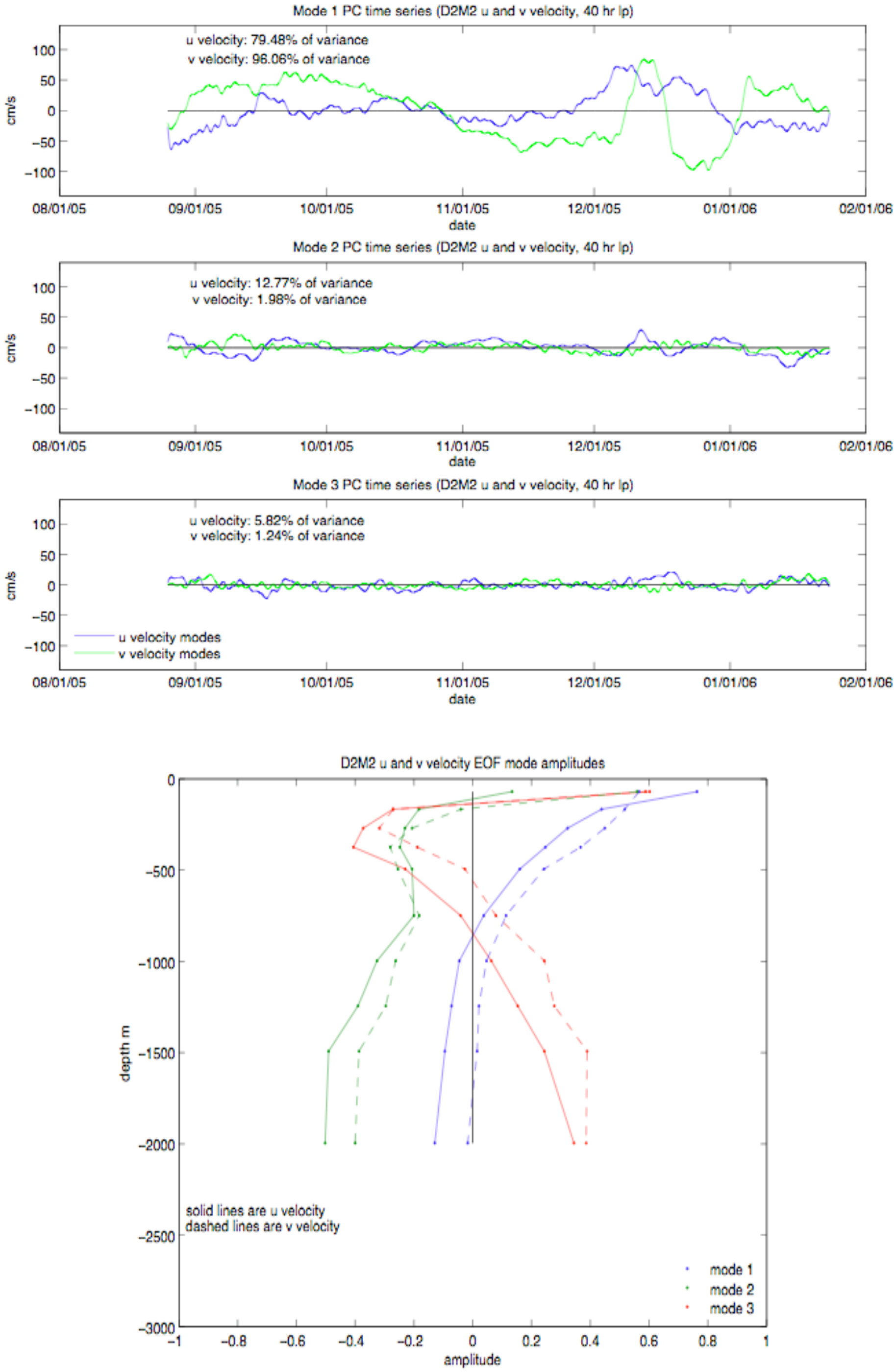

Figure A-29. Vertical EOFs of east-west and north-south current velocity at mooring M2 during deployment 2. Top three panels: Principal component (PC) time-series of first three empirical modes. Bottom panel: Amplitudes of empirical modes corresponding to PC time-series.

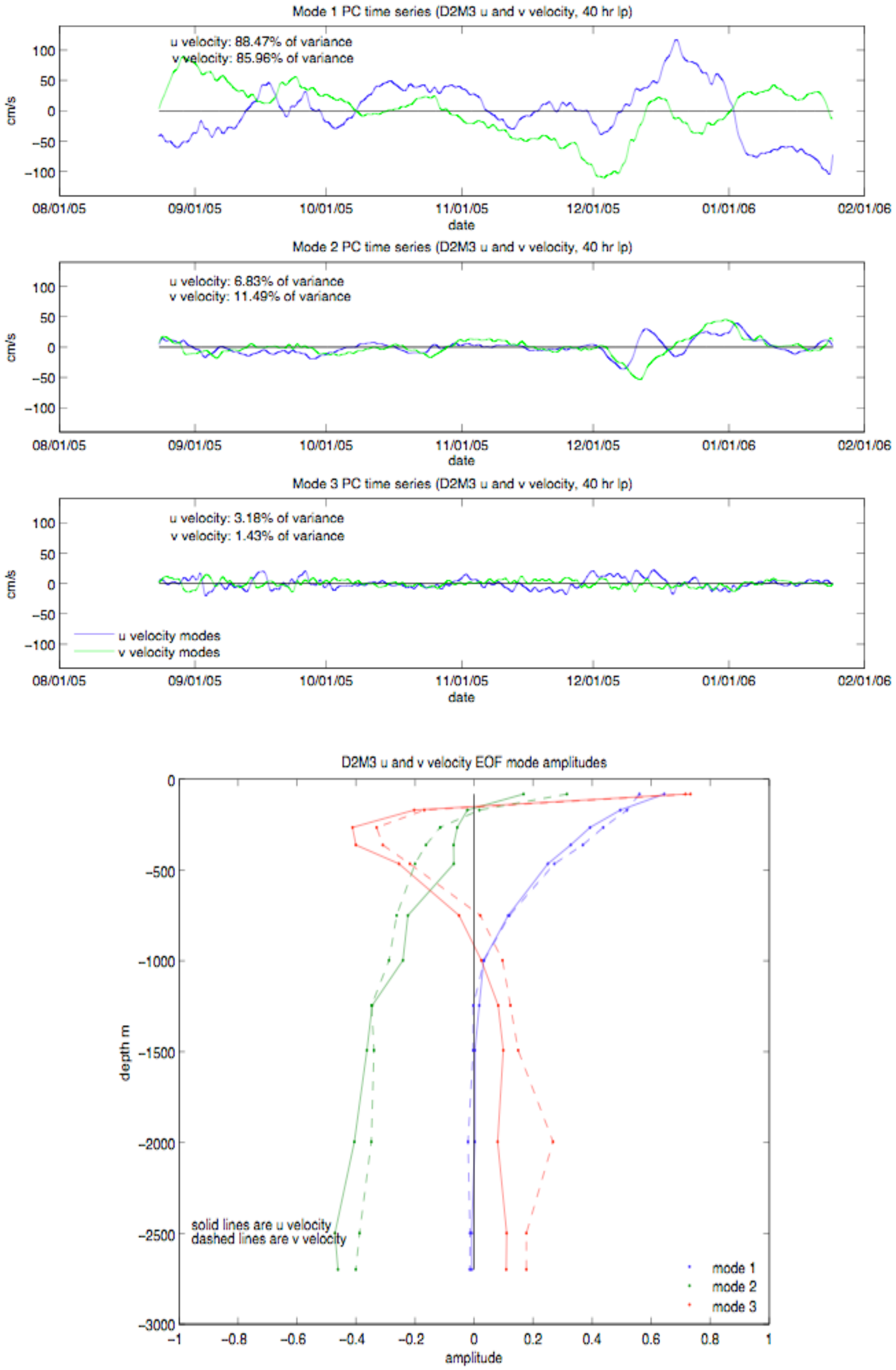

Figure A-30. Vertical EOFs of east-west and north-south current velocity at mooring M3 during deployment 2. Top three panels: Principal component (PC) time-series of first three empirical modes. Bottom panel: Amplitudes of empirical modes corresponding to PC time-series.

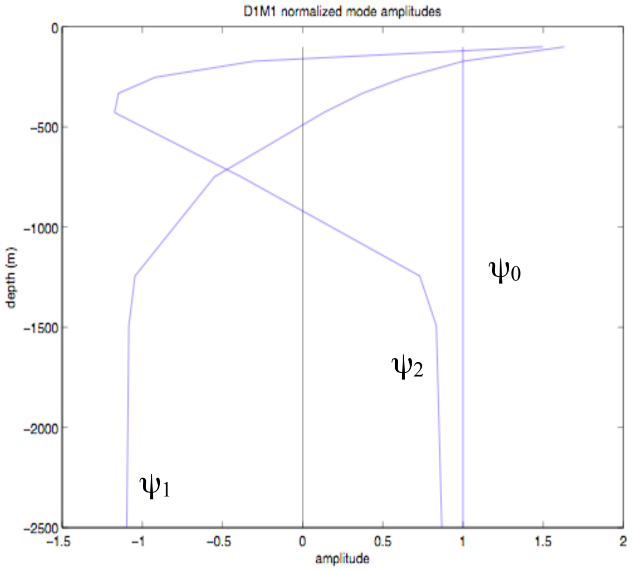

Figure A-31. Normalized barotropic and first two baroclinic modes calculated with averaged casts at mooring M1 from cruises in January and August of 2005.

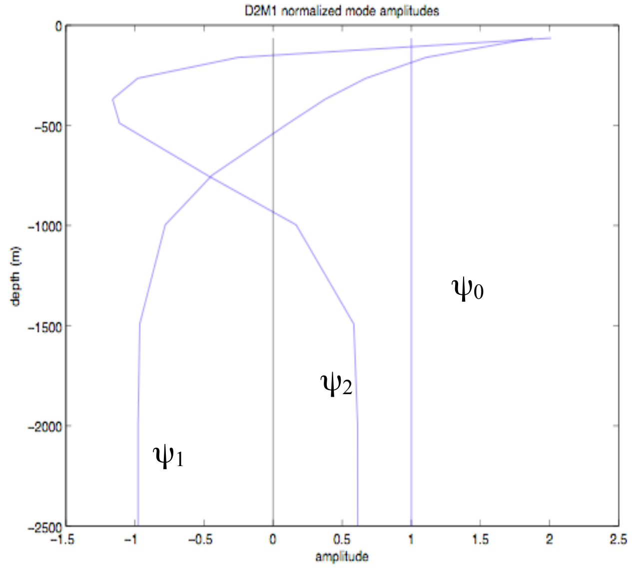

Figure A-32. Normalized barotropic and first two baroclinic modes calculated with averaged casts at mooring M1 from cruises in August 2005 and January 2006.

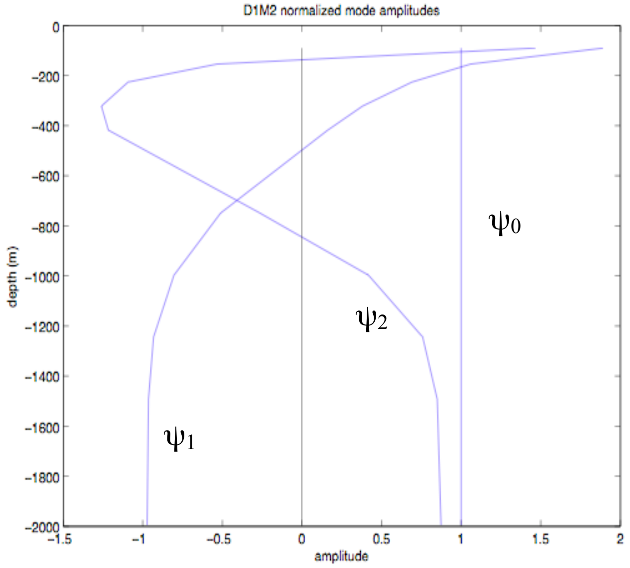

Figure A-33. Normalized barotropic and first two baroclinic modes calculated with averaged casts at mooring M2 from cruises in January and August of 2005.

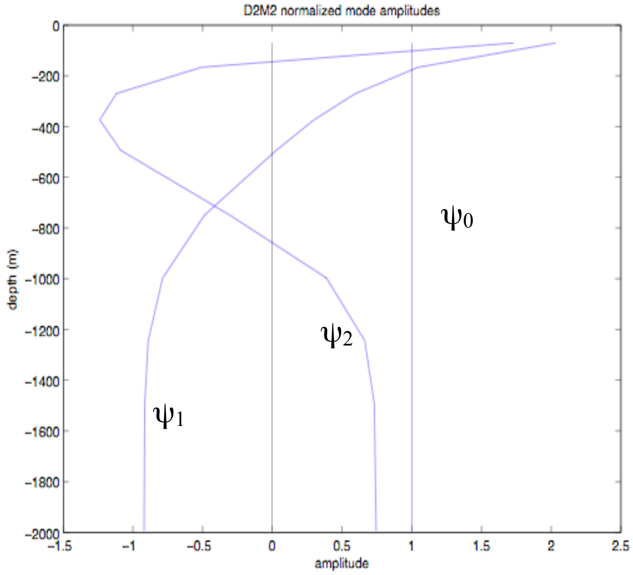

Figure A-34. Normalized barotropic and first two baroclinic modes calculated with averaged casts at mooring M2 from cruises in August 2005 and January 2006.

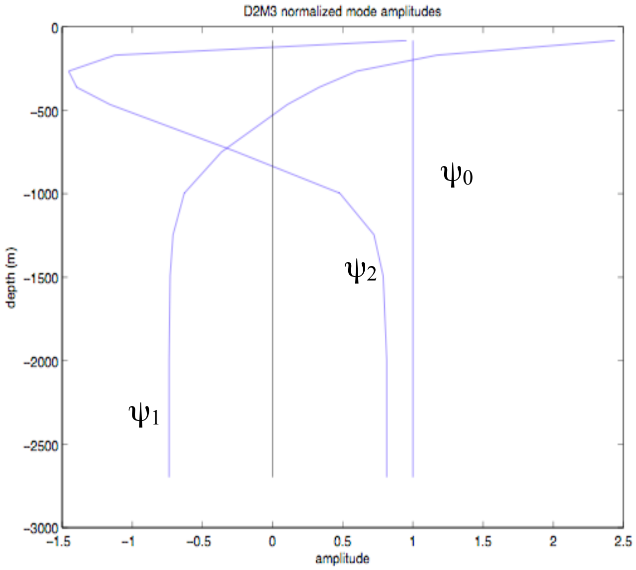

Figure A-35. Normalized barotropic and first two baroclinic modes calculated with averaged casts at M3 from cruises in August 2005 and January 2006.

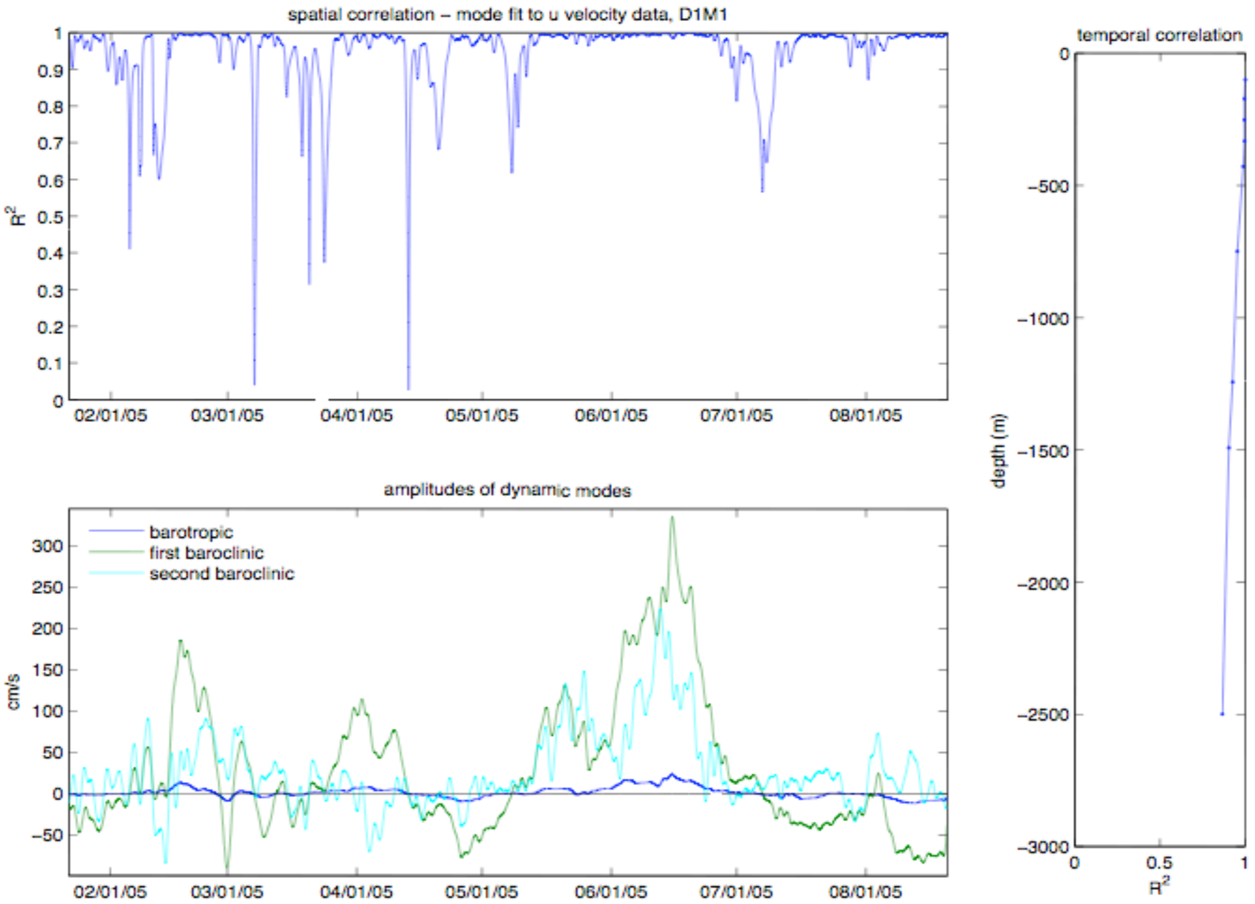

Figure A-36. (Top) Spatial correlation between observed *u*-velocity at mooring M1 from deployment 1 and the modeled *u*-velocity from CTD cast data on the EGOM hydrographic cruises. (Bottom) Amplitudes of the first three theoretical modes based on the least squares regression. (Right) Temporal correlation between modeled and observed velocity.

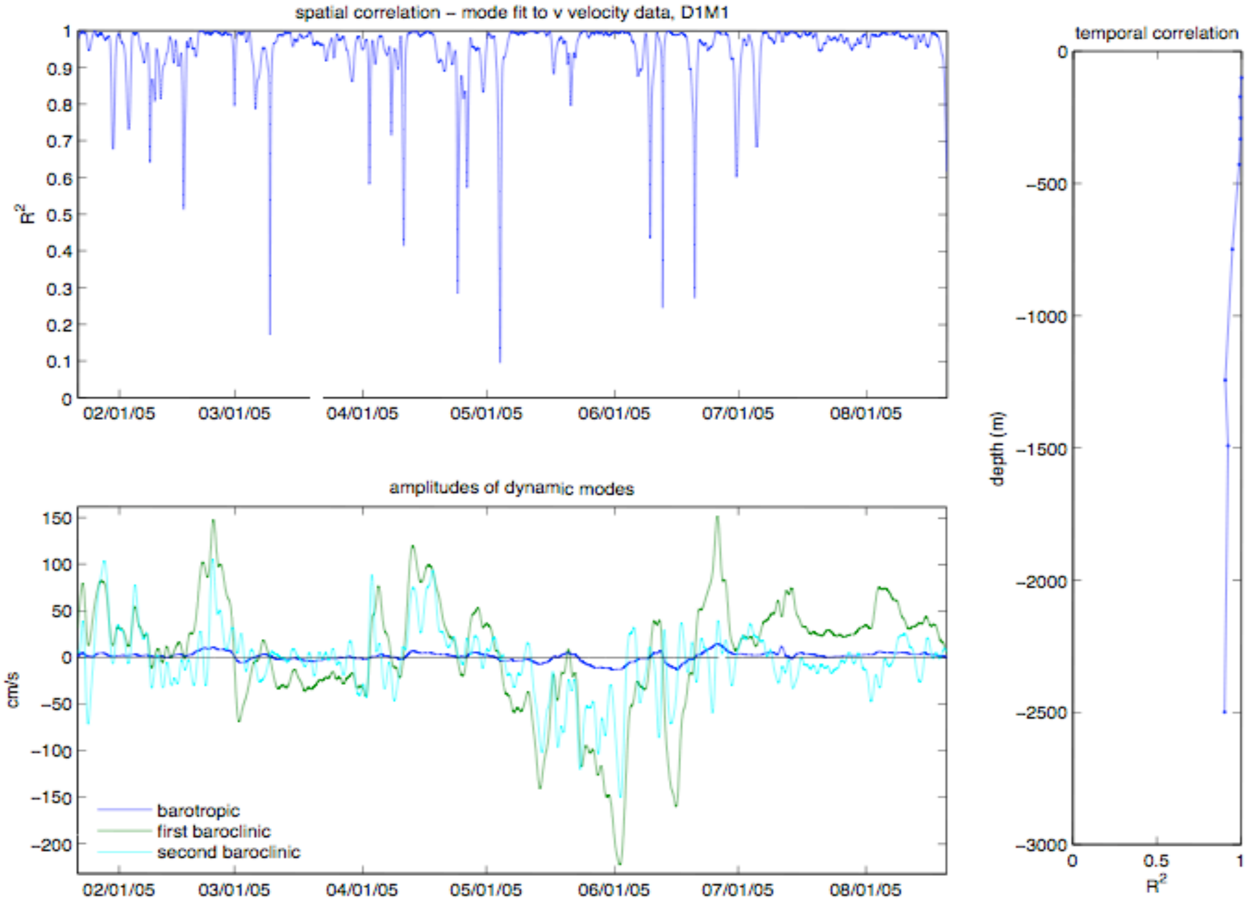

Figure A-37. (Top) Spatial correlation between observed *v*-velocity at mooring M1 from deployment 1 and the modeled *v*-velocity from CTD cast data on the EGOM hydrographic cruises. (Bottom) Amplitudes of the first three theoretical modes based on the least squares regression. (Right) Temporal correlation between the modeled and observed velocity.

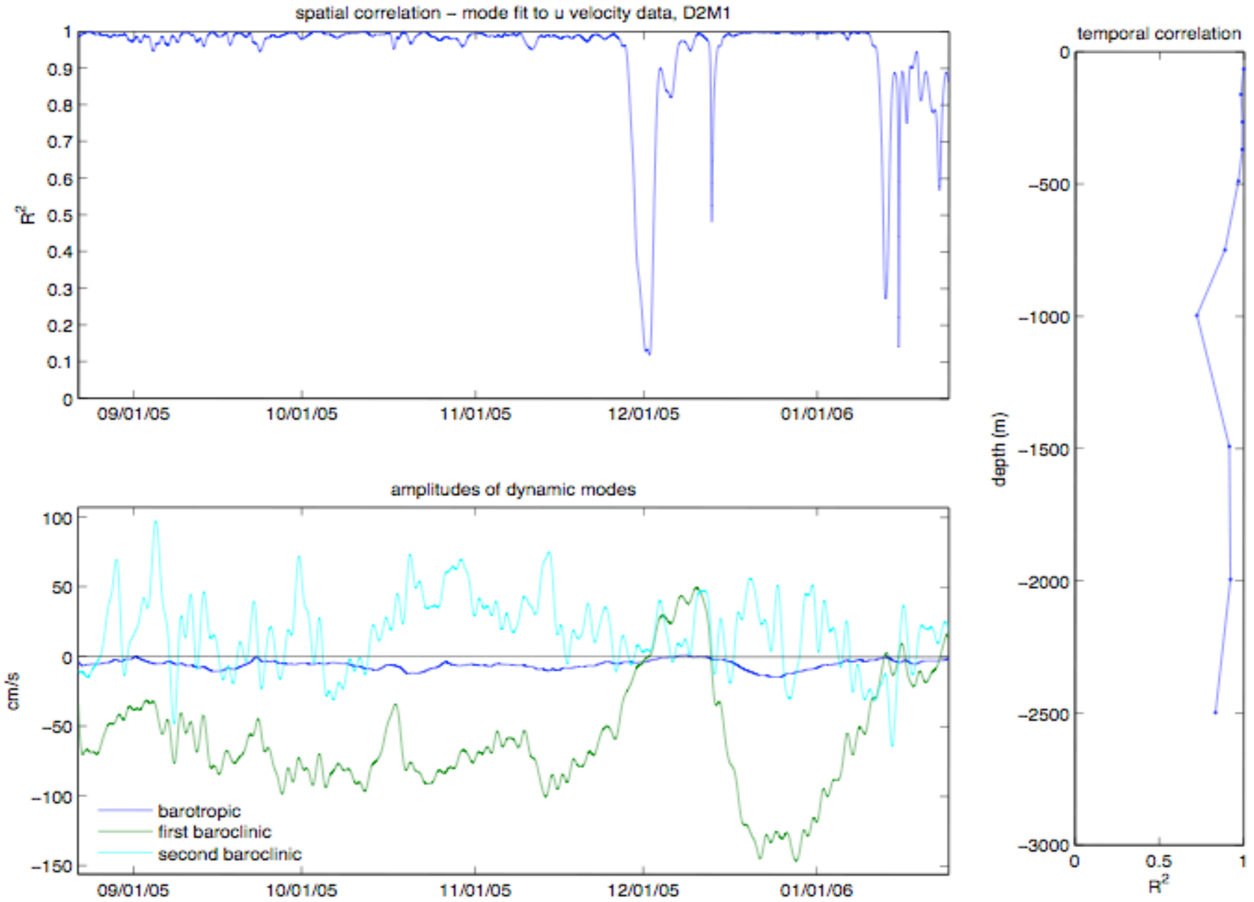

Figure A-38. (Top) Spatial correlation between observed *u*-velocity at mooring M1 from deployment 2 and the modeled *u*-velocity from CTD cast data on the EGOM hydrographic cruises. (Bottom) Amplitudes of the first three theoretical modes based on the least squares regression. (Right) Temporal correlation between the modeled and observed velocity.

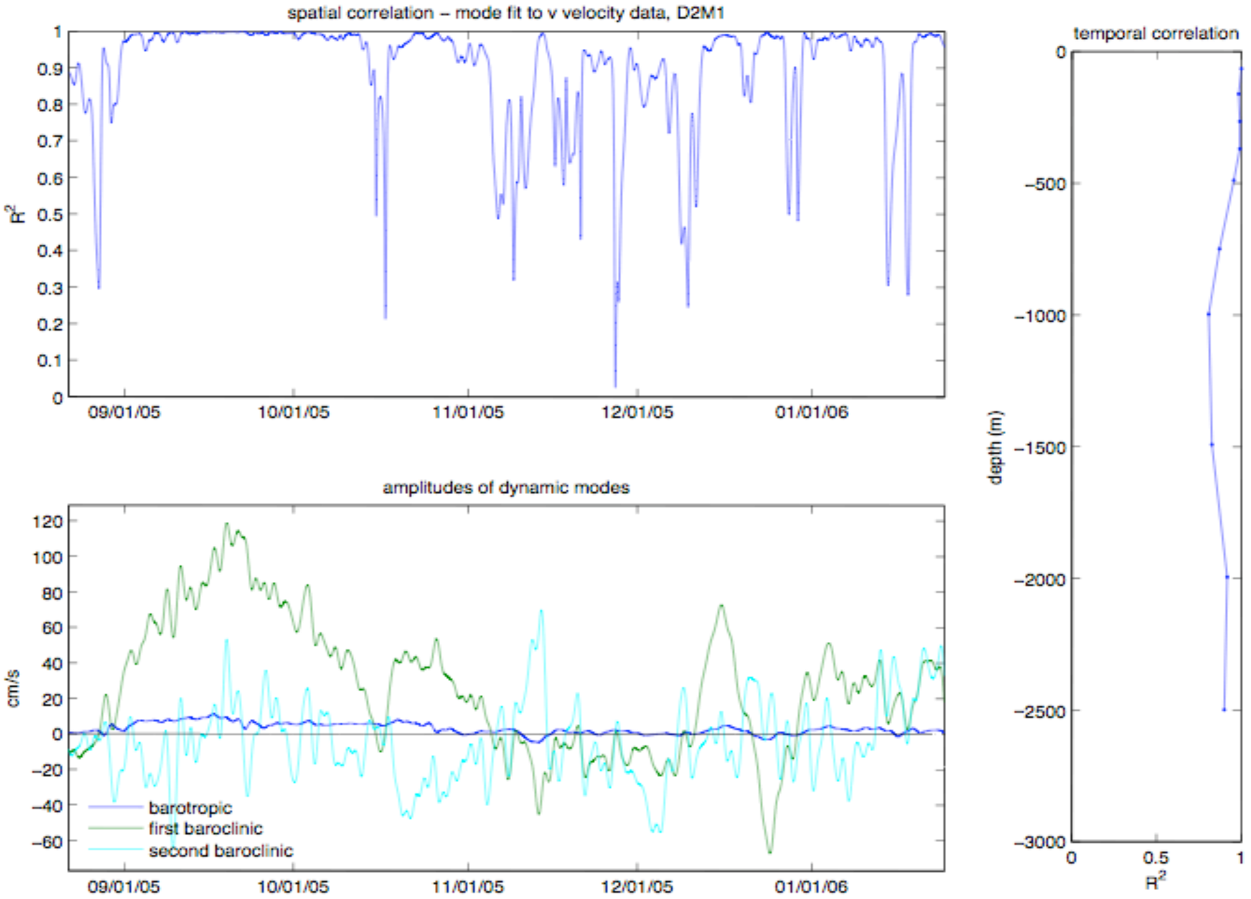

Figure A-39. (Top) Spatial correlation between observed *v*-velocity at mooring M1 from deployment 2 and the modeled *v*-velocity from CTD cast data on the EGOM hydrographic cruises. (Bottom) Amplitudes of the first three theoretical modes based on the least squares regression. (Right) Temporal correlation between the modeled and observed velocity.

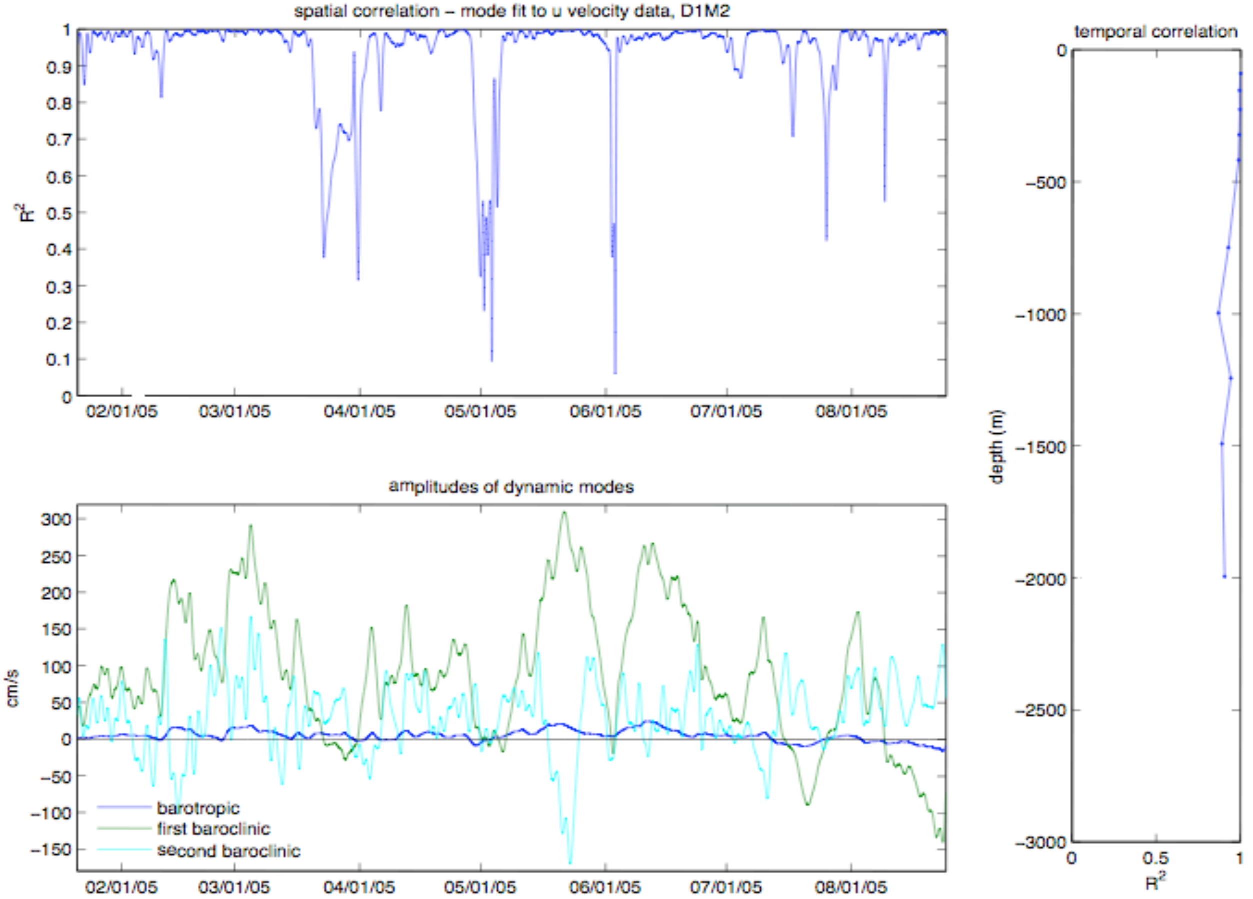

Figure A-40. (Top) Spatial correlation between observed *u*-velocity at mooring M2 from deployment 1 and the modeled *u*-velocity from CTD cast data on the EGOM hydrographic cruises. (Bottom) Amplitudes of the first three theoretical modes based on the least squares regression. (Right) Temporal correlation between the modeled and observed velocity.

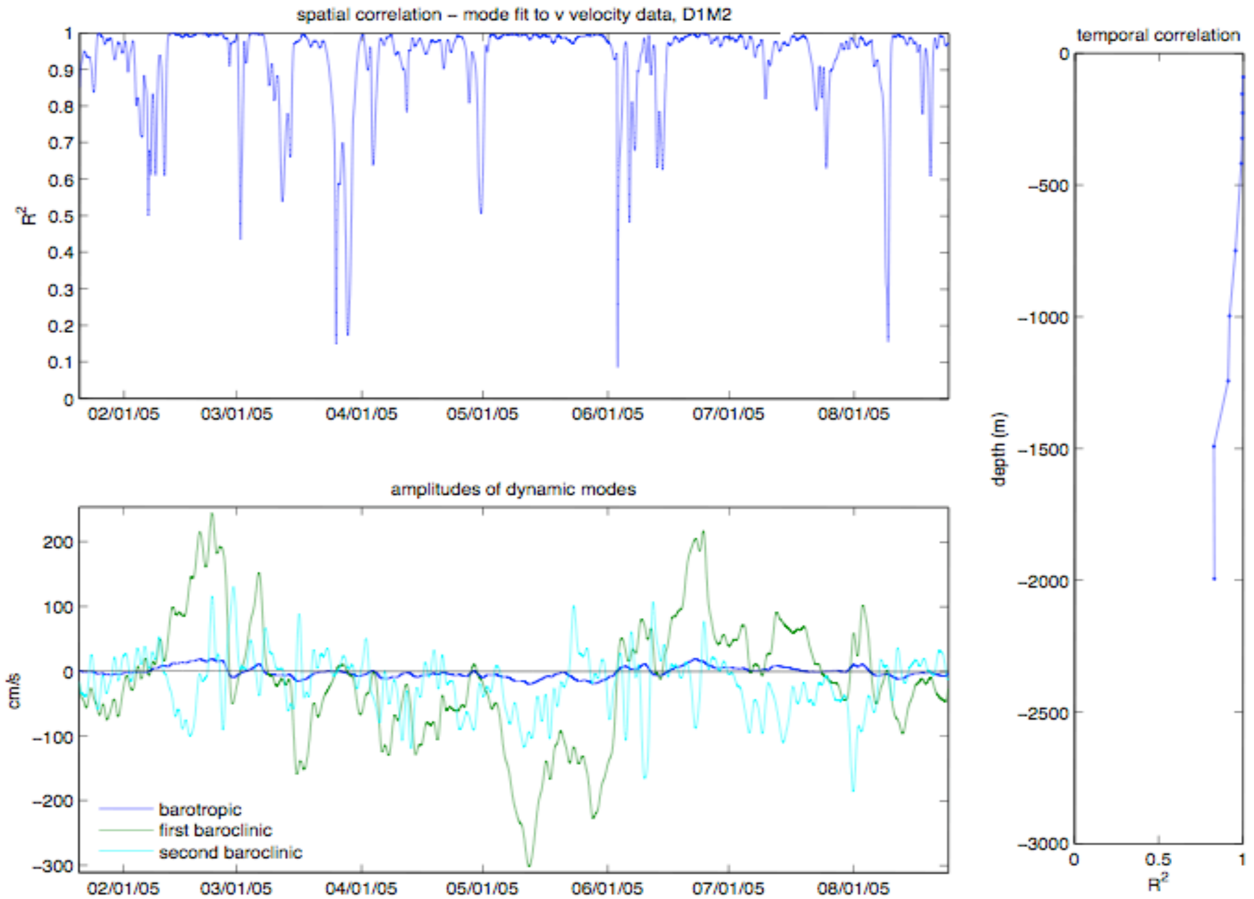

Figure A-41. (Top) Spatial correlation between observed *v*-velocity at mooring M2 from deployment 1 and the modeled *v*-velocity from CTD cast data on the EGOM hydrographic cruises. (Bottom) Amplitudes of the first three theoretical modes based on the least squares regression. (Right) Temporal correlation between the modeled and observed velocity.

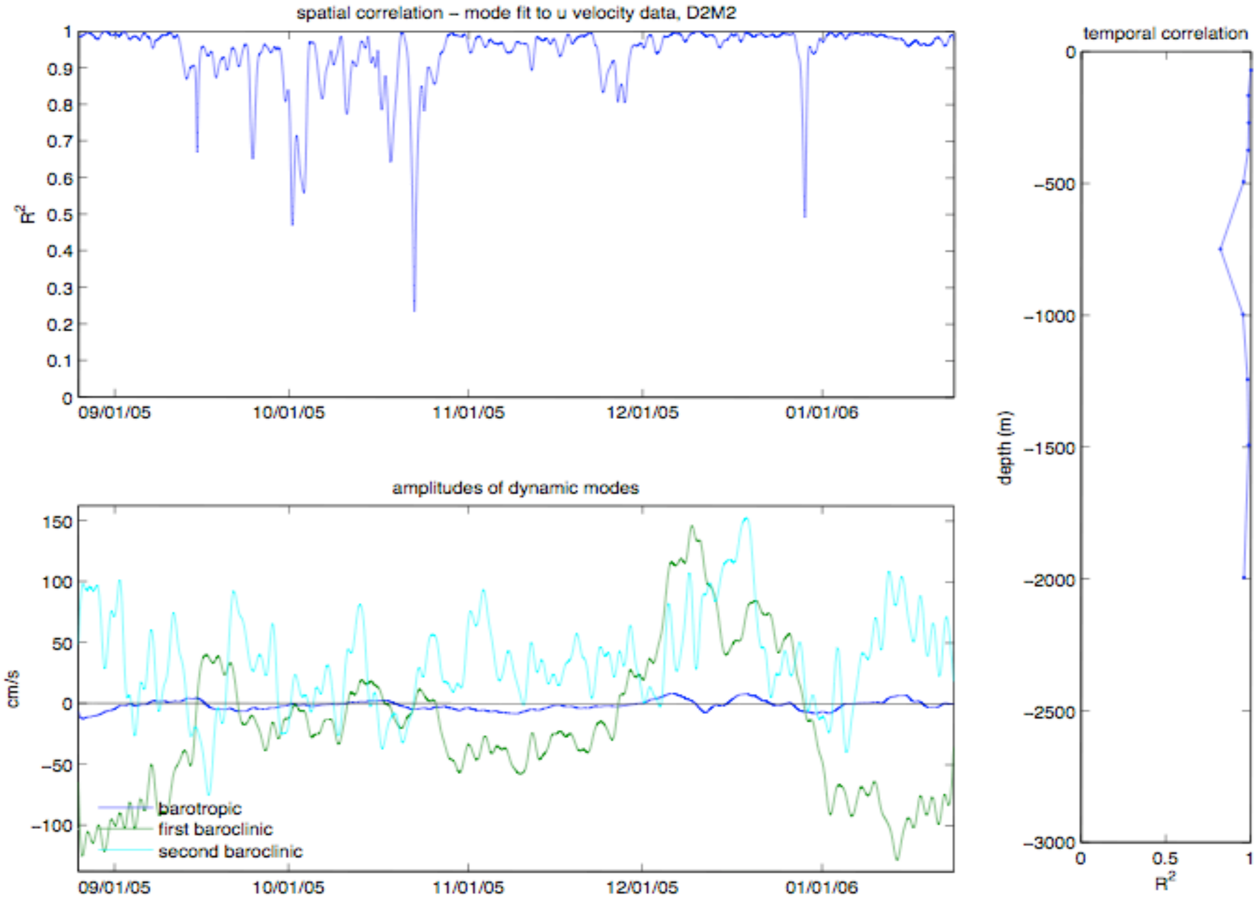

Figure A-42. (Top) Spatial correlation between observed *u*-velocity at mooring M2 from deployment 2 and the modeled *u*-velocity from CTD cast data on the EGOM hydrographic cruises. (Bottom) Amplitudes of the first three theoretical modes based on the least squares regression. (Right) Temporal correlation between the modeled and observed velocity.

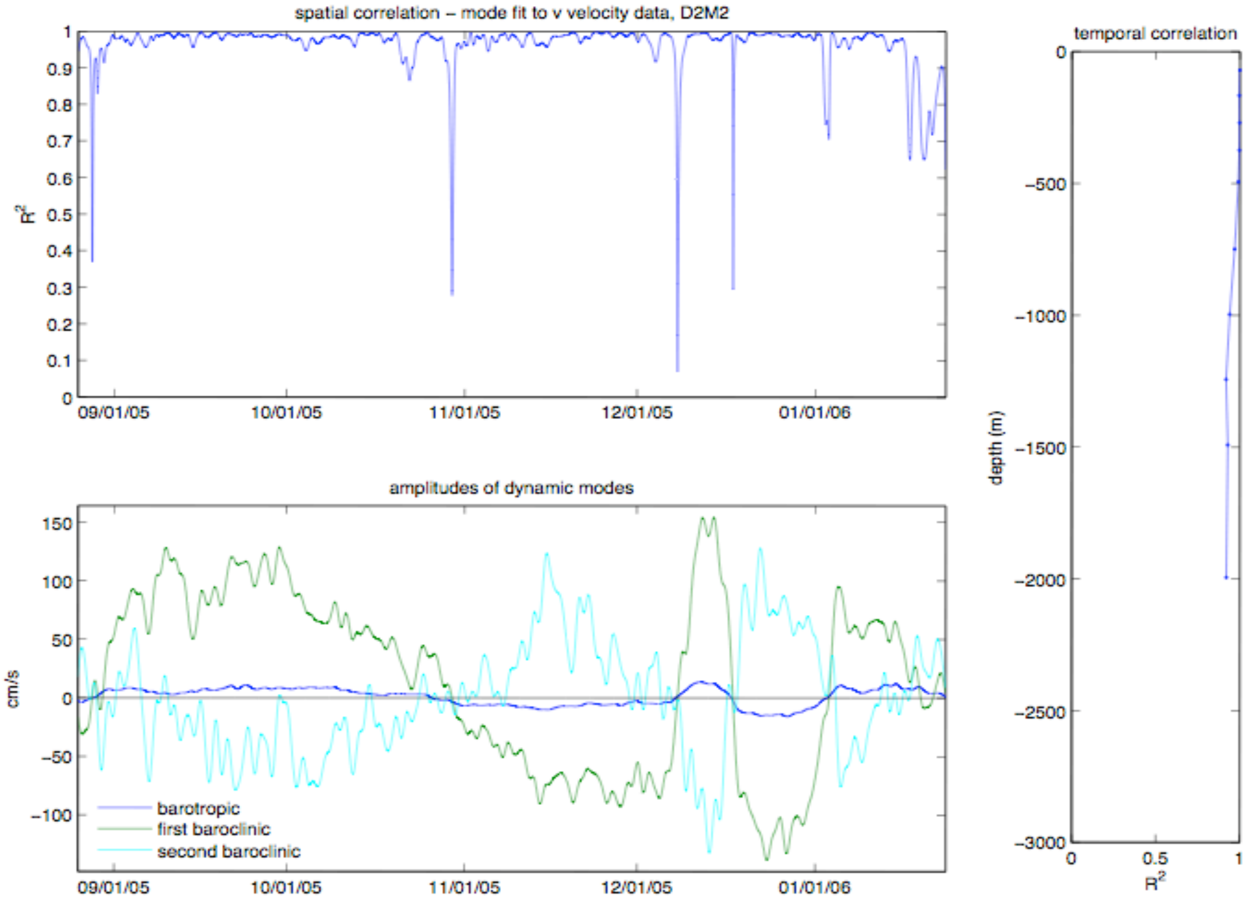

Figure A-43. (Top) Spatial correlation between observed *v*-velocity at mooring M2 from deployment 2 and the modeled *v*-velocity from CTD cast data on the EGOM hydrographic cruises. (Bottom) Amplitudes of the first three theoretical modes based on the least squares regression. (Right) Temporal correlation between the modeled and observed velocity.

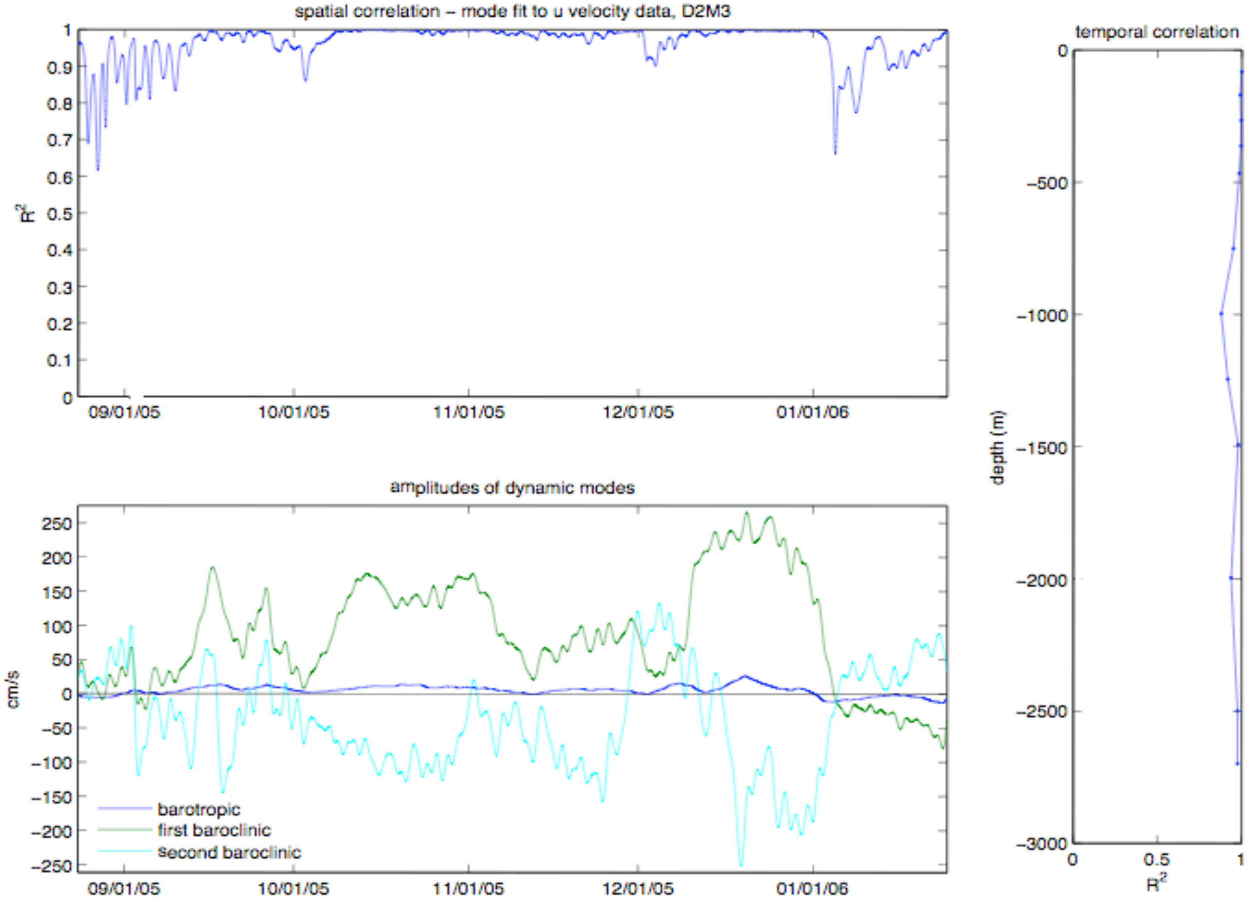

Figure A-44. (Top) Spatial correlation between observed *u*-velocity at mooring M3 from deployment 2 and the modeled *u*-velocity from CTD cast data on the EGOM hydrographic cruises. (Bottom) Amplitudes of the first three theoretical modes based on the least squares regression. (Right) Temporal correlation between the modeled and observed velocity.

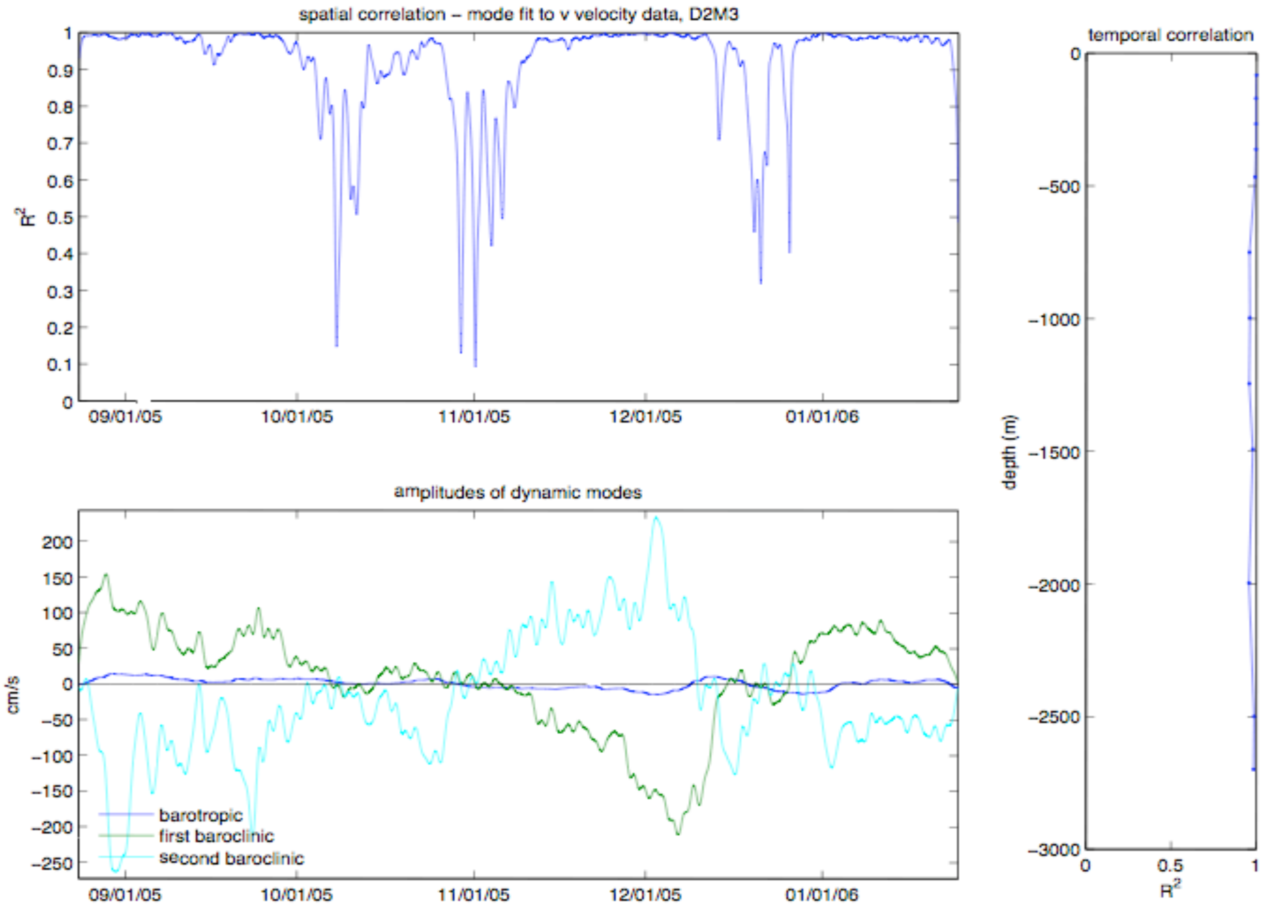

Figure A-45. (Top) Spatial correlation between observed *v*-velocity at mooring M3 from deployment 2 and the modeled *v*-velocity from CTD cast data on the EGOM hydrographic cruises. (Bottom) Amplitudes of the first three theoretical modes based on the least squares regression. (Right) Temporal correlation between the modeled and observed velocity.

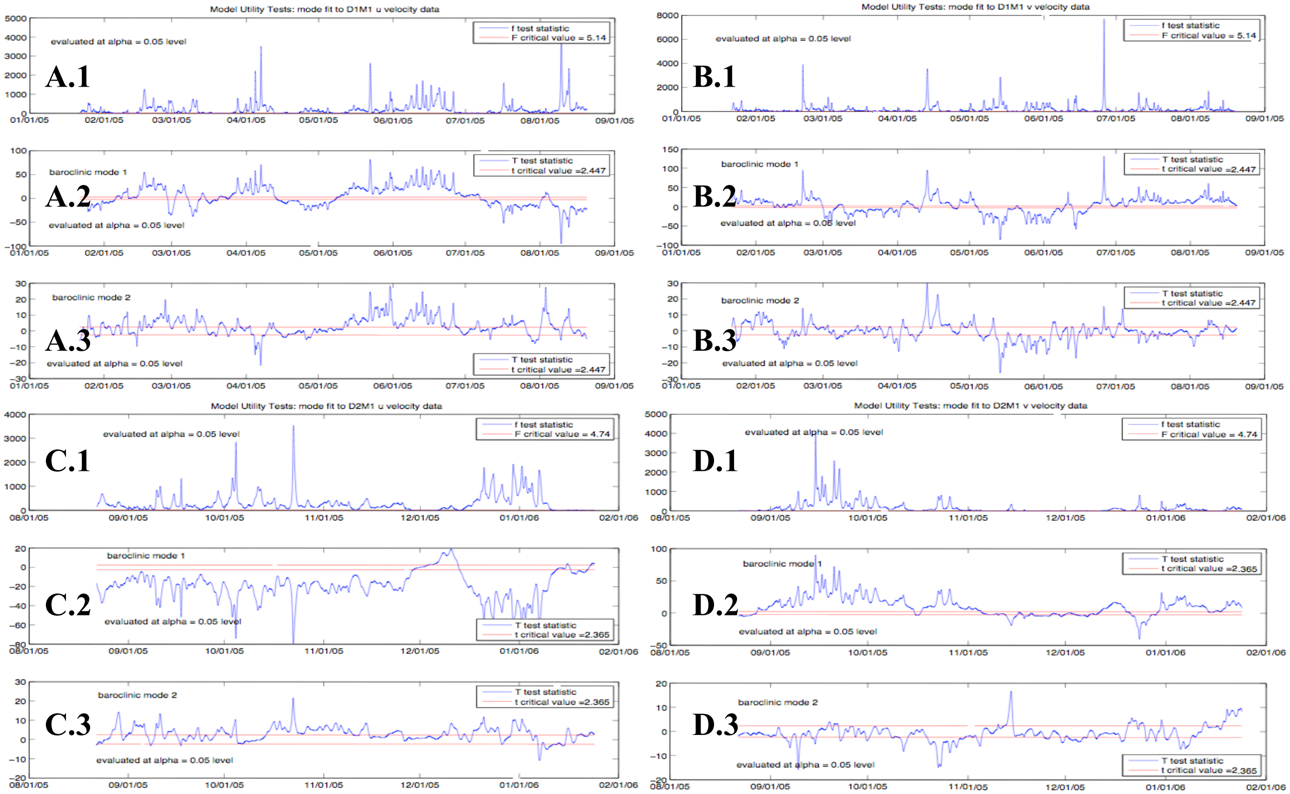

Figure A-46. Goodness of fit tests for A. M1 *u*-velocity during deployment 1, B. M1 *v*-velocity during deployment 1, C. M1 *u*-velocity during deployment 2, and D. M1 *v*-velocity during deployment 2. Panels labeled with 1 are model utility tests of the necessity of the first three modes in the model. Panels labeled 2 and 3 are tests for the necessity of the first baroclinic and second baroclinic modes respectively to the model.

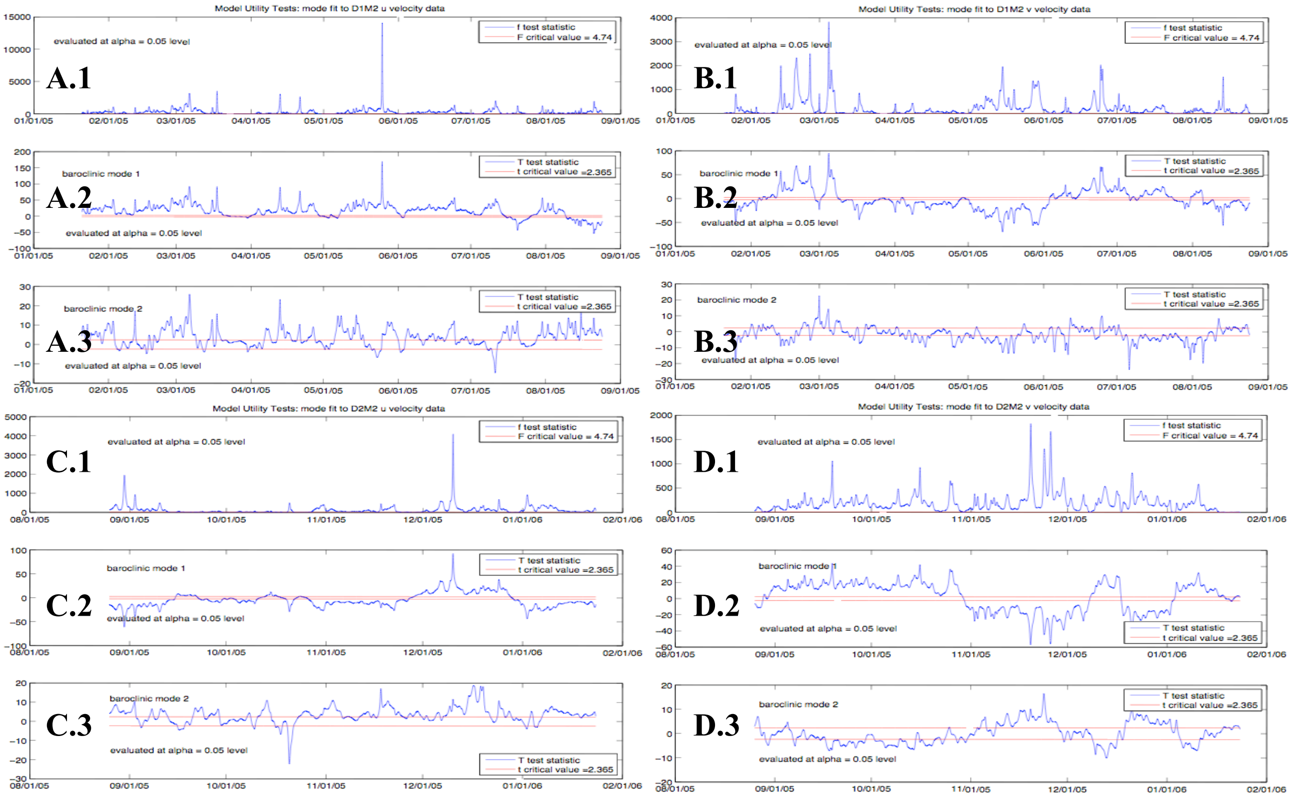

Figure A-47. Goodness of fit tests for A. M2 *u*-velocity during deployment 1, B. M2 *v*-velocity during deployment 1, C. M2 *u*-velocity during deployment 2, and D. M2 *v*-velocity during deployment 2. Panels labeled with 1 are model utility tests of the necessity of the first three modes in the model. Panels labeled 2 and 3 are tests for the necessity of the first baroclinic and second baroclinic modes respectively to the model.

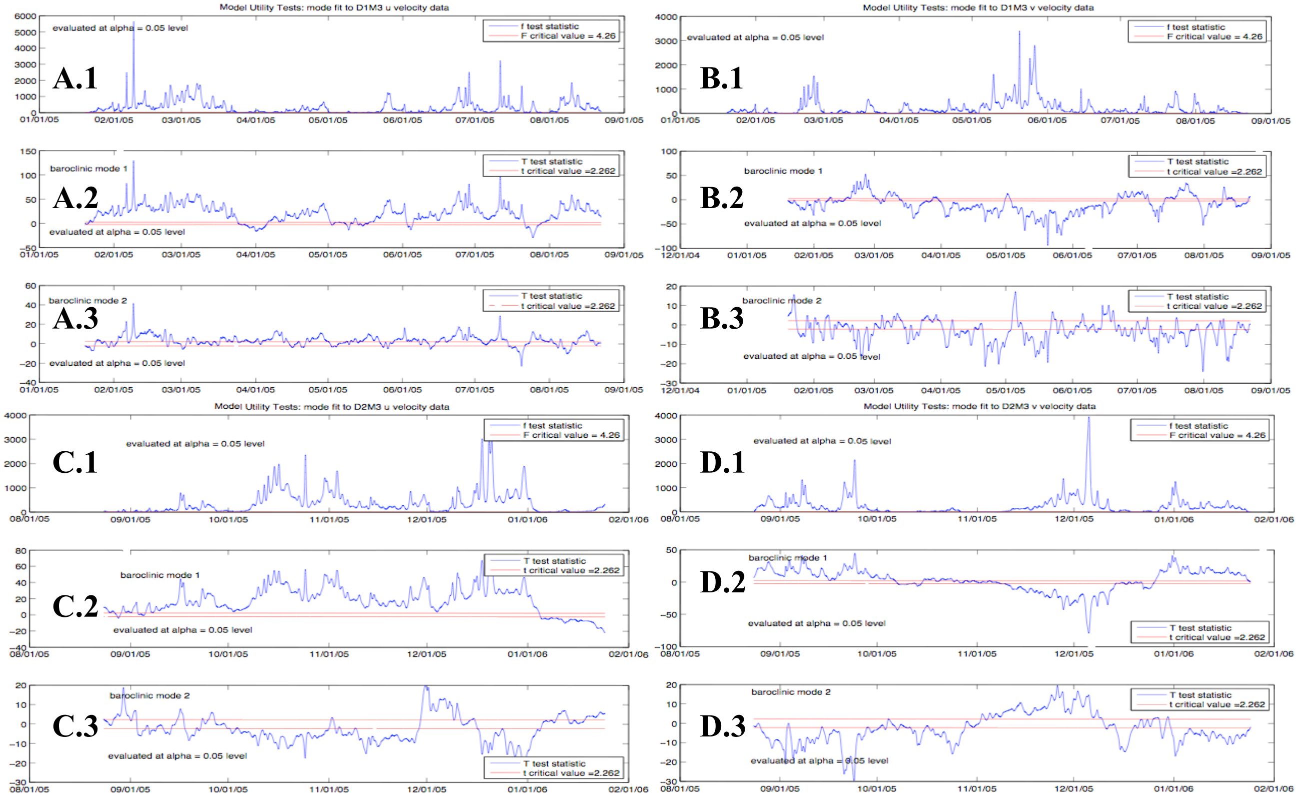

Figure A-48. Goodness of fit tests for A. M3 *u*-velocity during deployment 1, B. M3 *v*-velocity during deployment 1, C. M3 *u*-velocity during deployment 2, and D. M3 *v*-velocity during deployment 2. Panels labeled with 1 are model utility tests of the necessity of the first three modes in the model. Panels labeled 2 and 3 are tests for the necessity of the first baroclinic and second baroclinic modes respectively to the model.

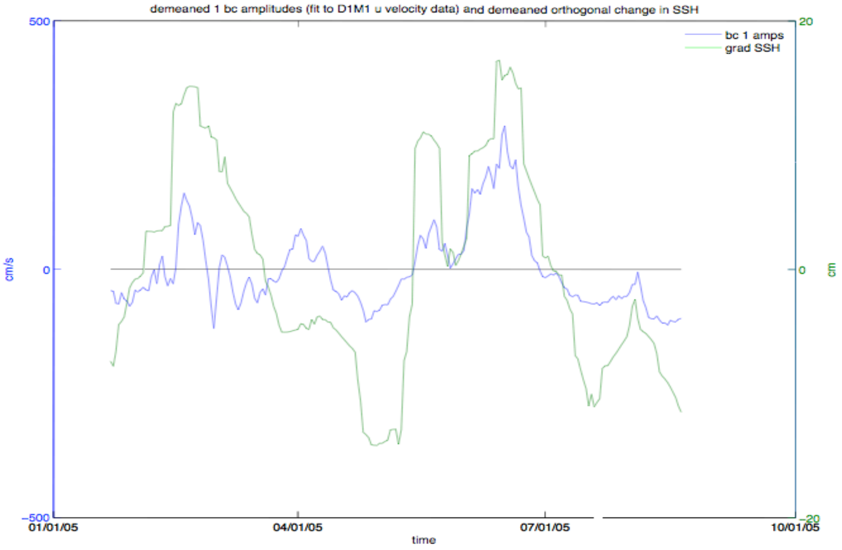

Figure A-49. Temporal amplitudes of the first baroclinic mode for the east-west velocity component at mooring M1 during deployment 1 (blue) and the SSH gradient in the north-south direction (green).

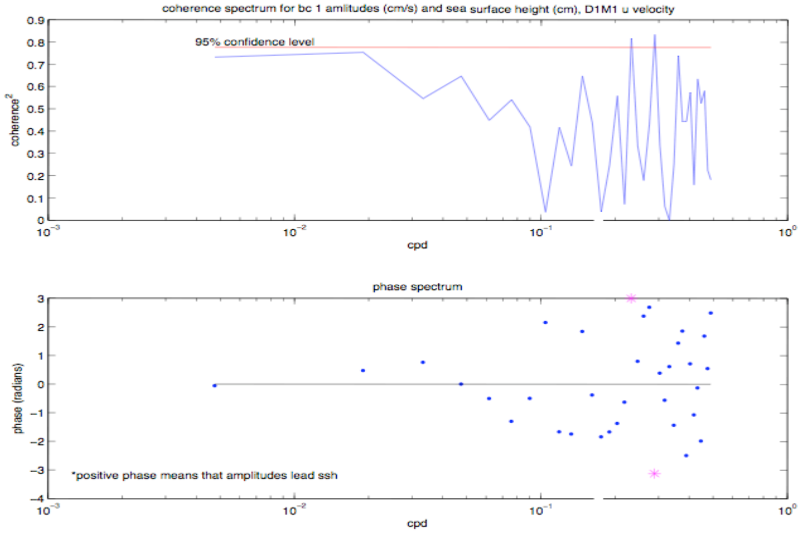

Figure A-50. Coherency (top) and phase (bottom) spectra of the temporal amplitudes of the first baroclinic mode for the east-west velocity component at mooring M1 during deployment 1 and the SSH gradient in the north-south direction.

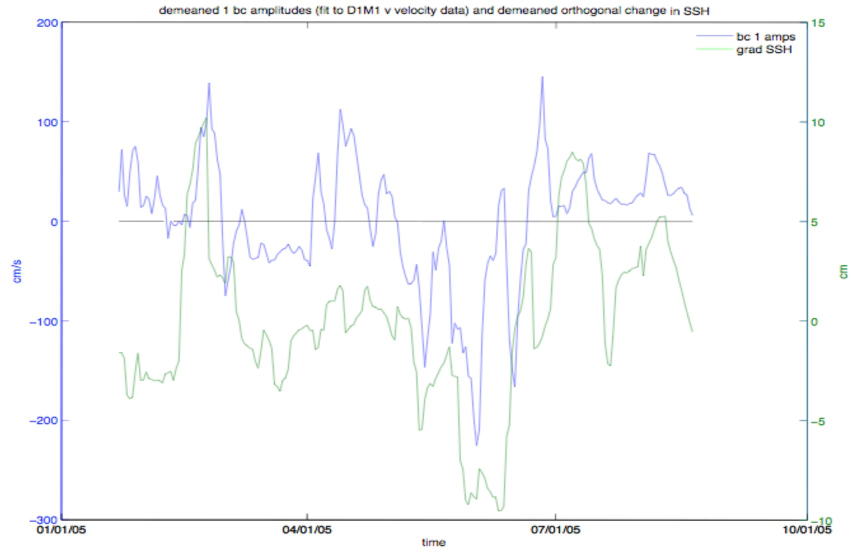

Figure A-51. Temporal amplitudes of the first baroclinic mode for the north-south velocity component at mooring M1 during deployment 1 (blue) and the SSH gradient in the east-west direction (green).

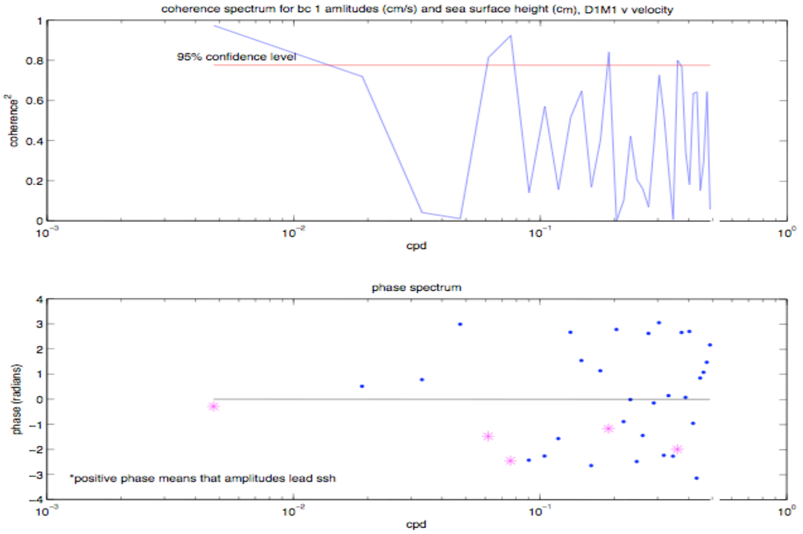

Figure A-52. Coherency (top) and phase (bottom) spectra of the temporal amplitudes of the first baroclinic mode for the north-south velocity component at mooring M1 during deployment 1 and the SSH gradient in the east-west direction.

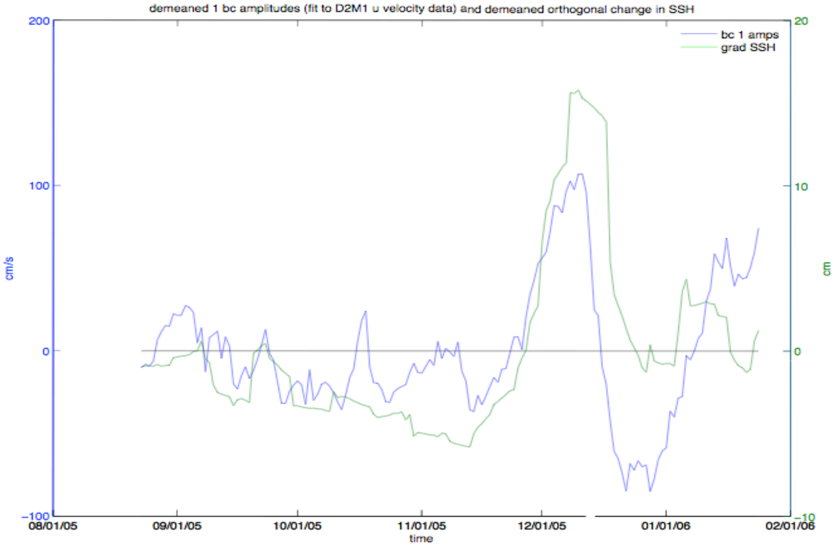

Figure A-53. Temporal amplitudes of the first baroclinic mode for the east-west velocity component at mooring M1 during deployment 2 (blue) and the SSH gradient in the north-south direction (green).

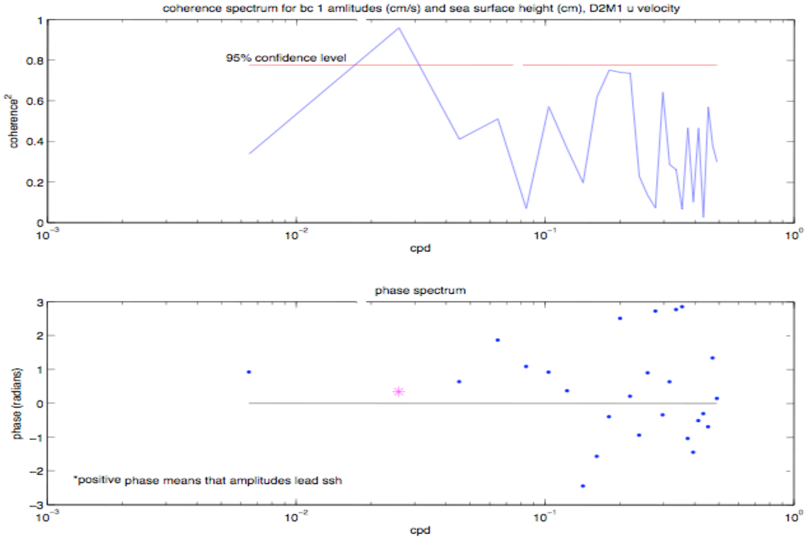

Figure A-54. Coherency (top) and phase (bottom) spectra of the temporal amplitudes of the first baroclinic mode for the east-west velocity component at mooring M1 during deployment 2 and the SSH gradient in the north-south direction.

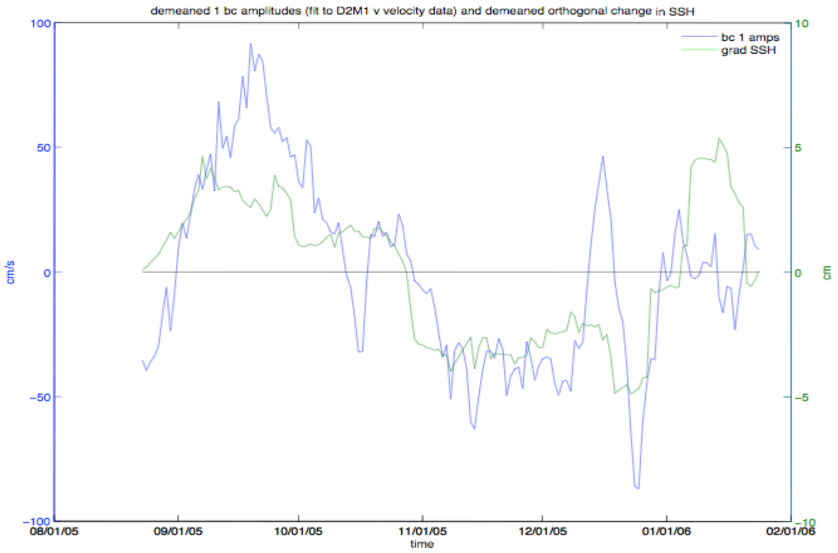

Figure A-55. Temporal amplitudes of the first baroclinic mode for the north-south velocity component at mooring M1 during deployment 2 (blue) and the SSH gradient in the east-west direction (green).

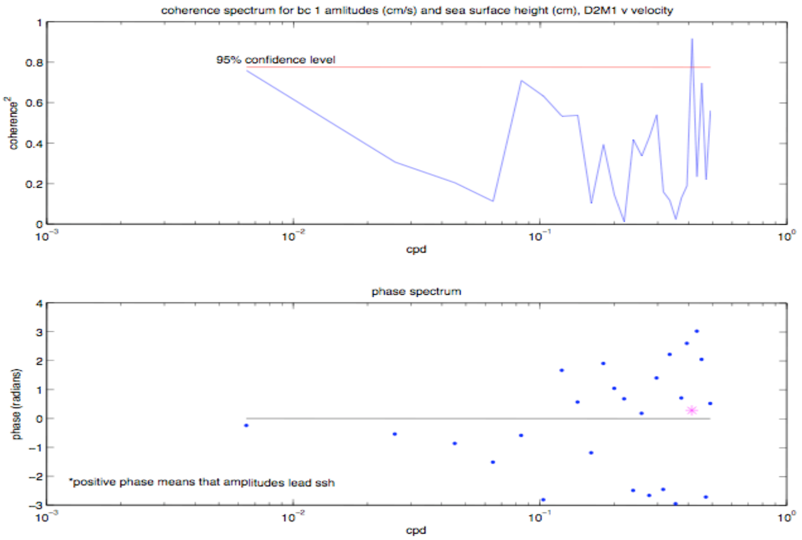

Figure A-56. Coherency (top) and phase (bottom) spectra of the temporal amplitudes of the first baroclinic mode for the north-south velocity component at mooring M1 during deployment 2 and the SSH gradient in the east-west direction.

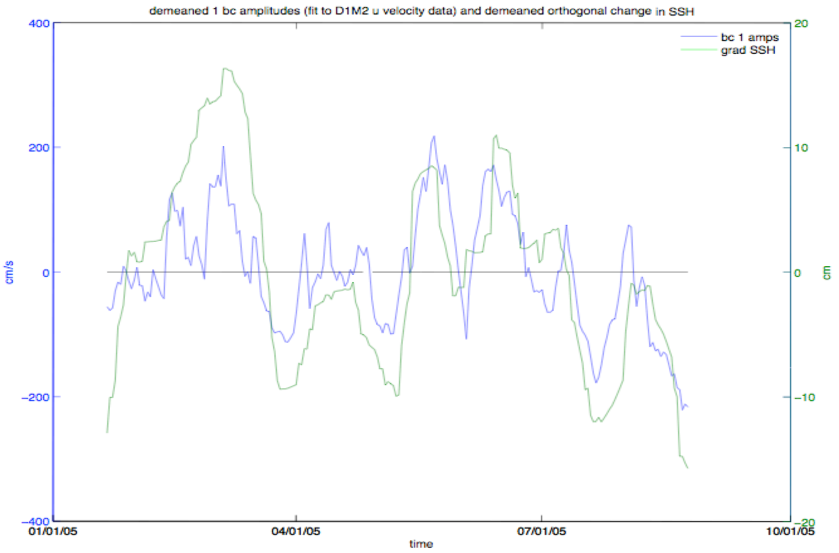

Figure A-57. Temporal amplitudes of the first baroclinic mode for the east-west velocity component at mooring M2 during deployment 1 (blue) and the SSH gradient in the north-south direction (green).

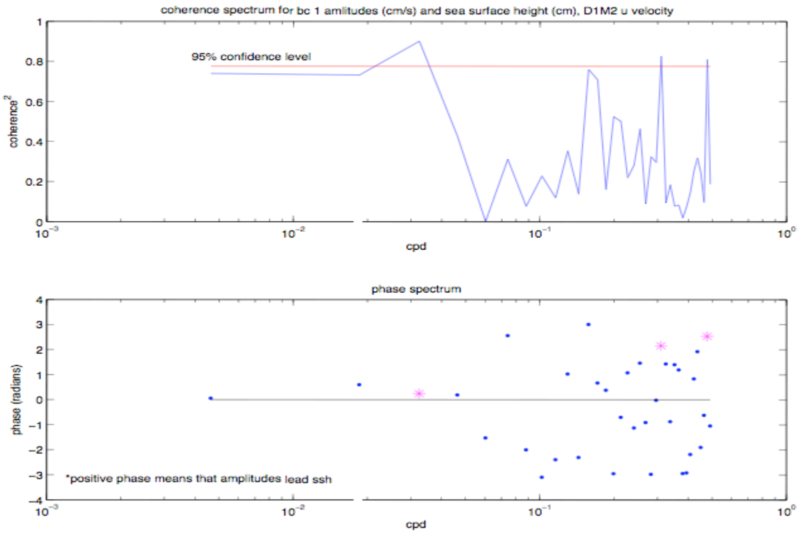

Figure A-58. Coherency (top) and phase (bottom) spectra of the temporal amplitudes of the first baroclinic mode for the east-west velocity component at mooring M2 during deployment 1 and the SSH gradient in the north-south direction.

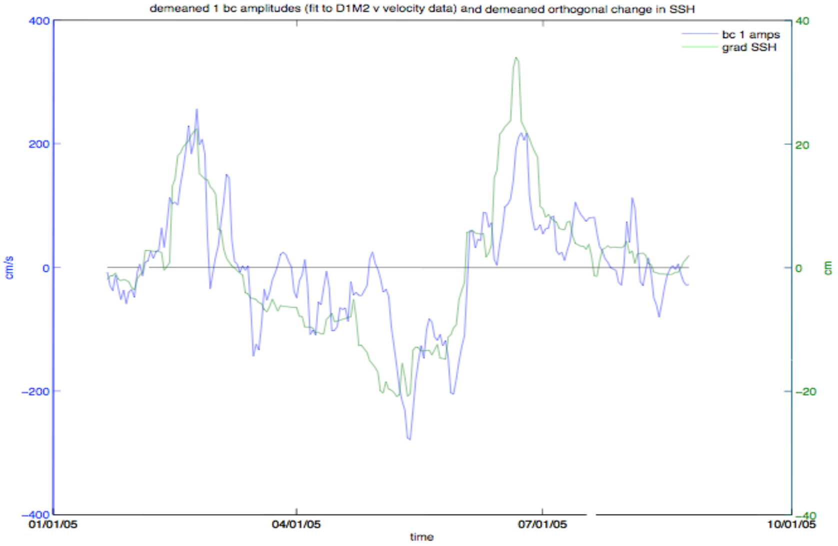

Figure A-59. Temporal amplitudes of the first baroclinic mode for the north-south velocity component at mooring M2 during deployment 1 (blue) and the SSH gradient in the east-west direction (green).

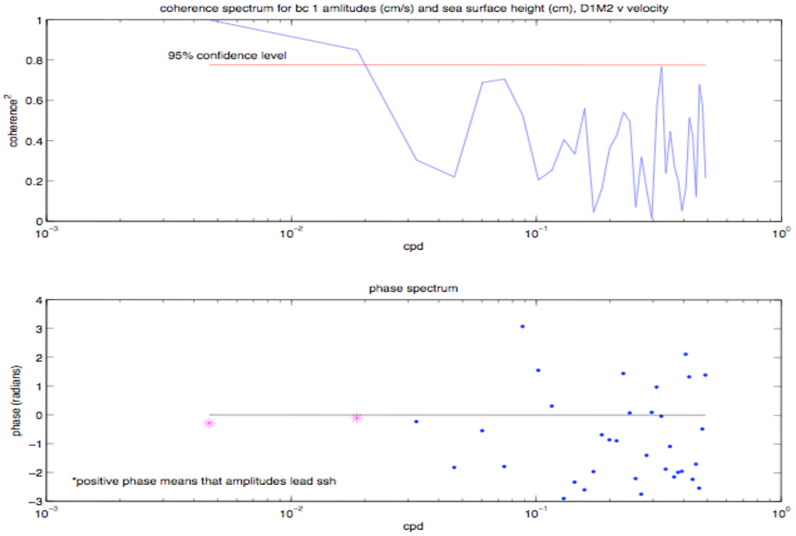

Figure A-60. Coherency (top) and phase (bottom) spectra of the temporal amplitudes of the first baroclinic mode for the north-south velocity component at mooring M2 during deployment 1 and the SSH gradient in the east-west direction.

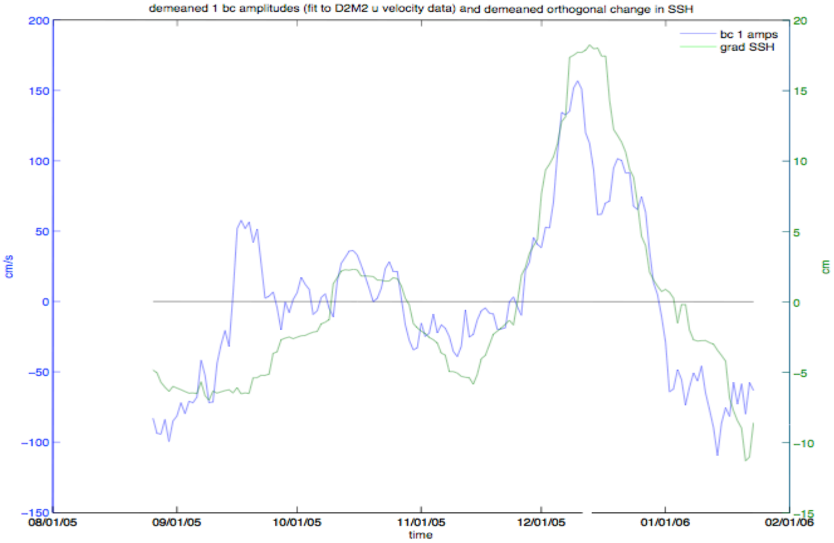

Figure A-61. Temporal amplitudes of the first baroclinic mode for the east-west velocity component at mooring M2 during deployment 2 (blue) and the SSH gradient in the north-south direction (green).

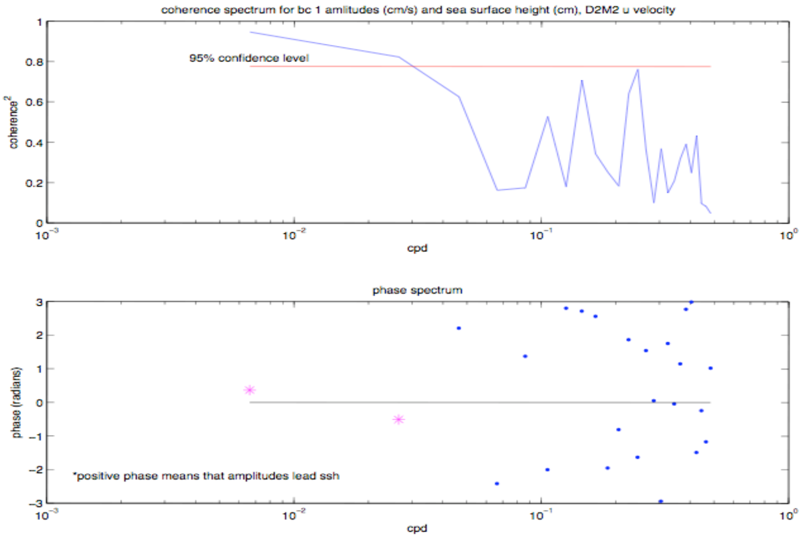

Figure A-62. Coherency (top) and phase (bottom) spectra of the temporal amplitudes of the first baroclinic mode for the east-west velocity component at mooring M2 during deployment 2 and the SSH gradient in the north-south direction.

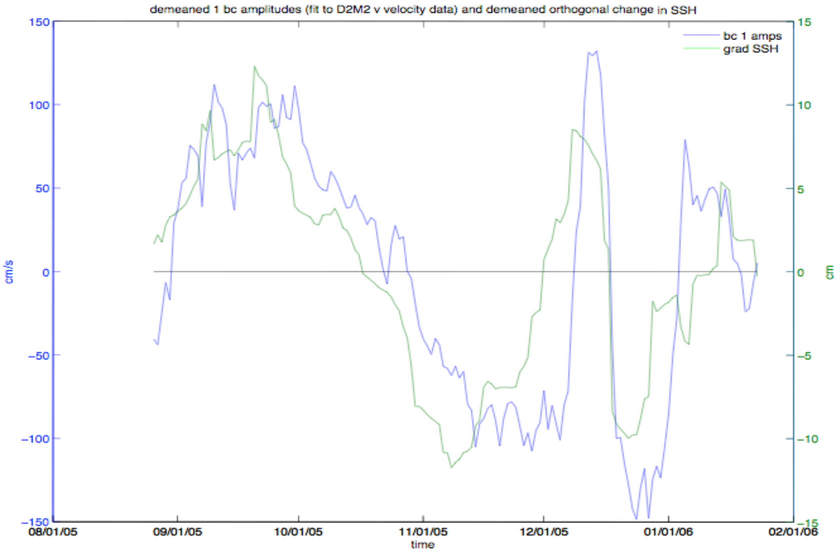

Figure A-63. Temporal amplitudes of the first baroclinic mode for the north-south velocity component at mooring M2 during deployment 2 (blue) and the SSH gradient in the east-west direction (green).

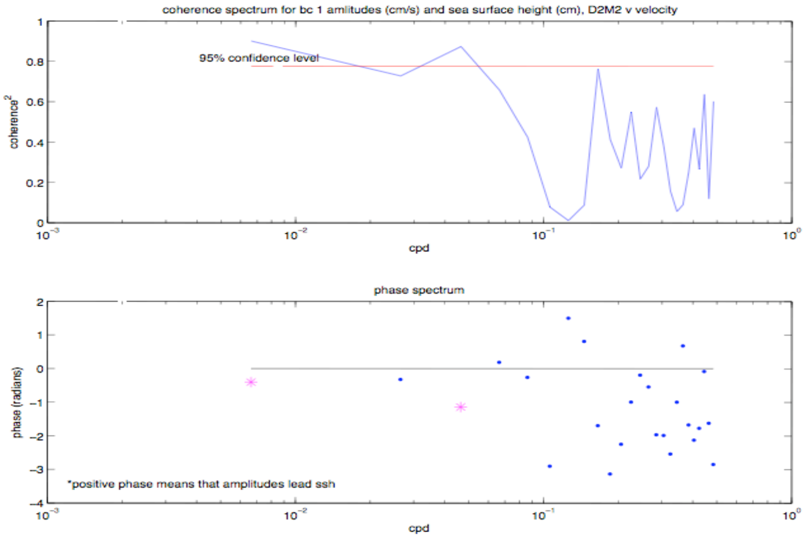

Figure A-64. Coherency (top) and phase (bottom) spectra of the temporal amplitudes of the first baroclinic mode for the north-south velocity component at mooring M2 during deployment 2 and the SSH gradient in the east-west direction.

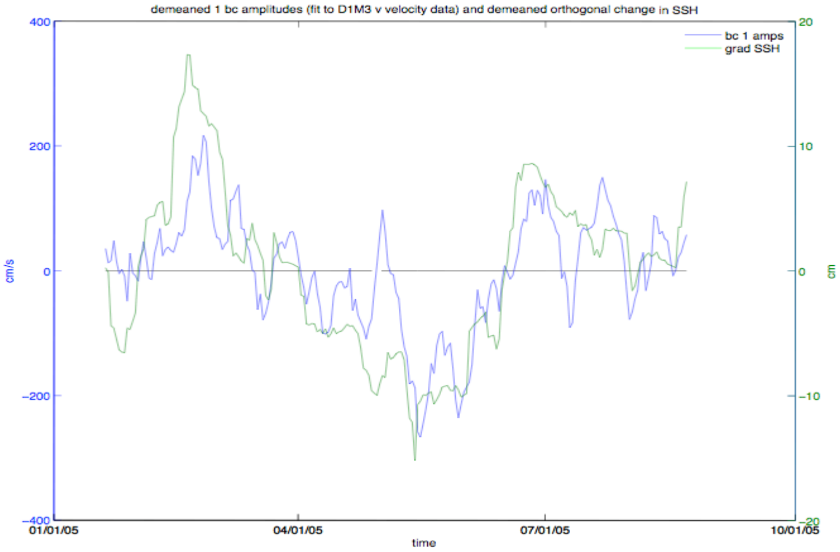

Figure A-65. Temporal amplitudes of the first baroclinic mode for the north-south velocity component at mooring M3 during deployment 1 (blue) and the SSH gradient in the east-west direction (green).

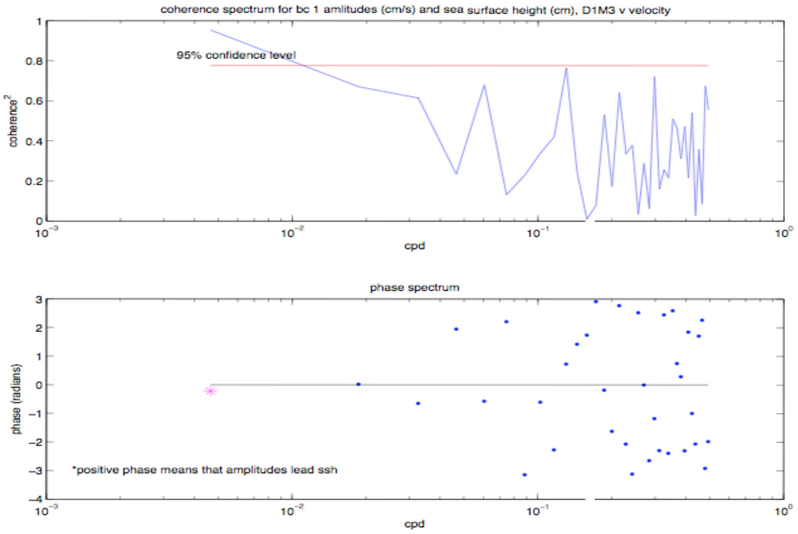

Figure A-66. Coherency (top) and phase (bottom) spectra of the temporal amplitudes of the first baroclinic mode for the north-south velocity component at mooring M3 during deployment 1 and the SSH gradient in the east-west direction.

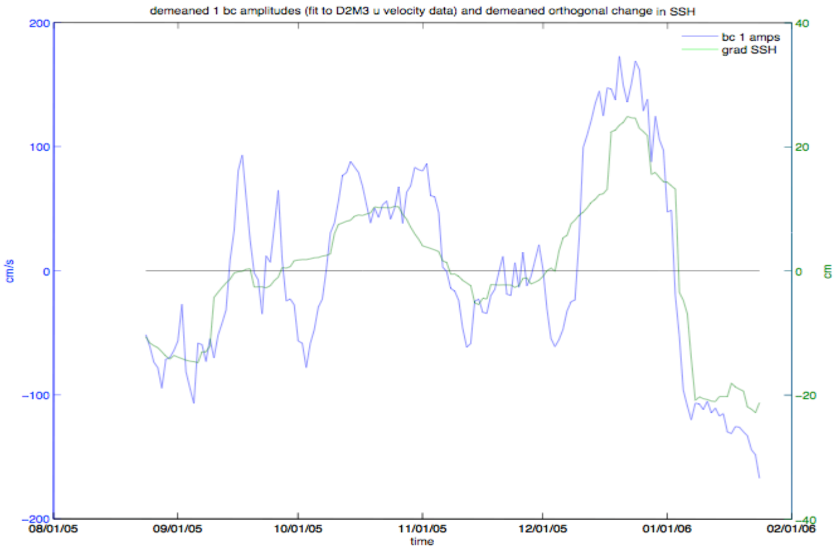

Figure A-67. Temporal amplitudes of the first baroclinic mode for the east-west velocity component at mooring M3 during deployment 2 (blue) and the SSH gradient in the north-south direction (green).

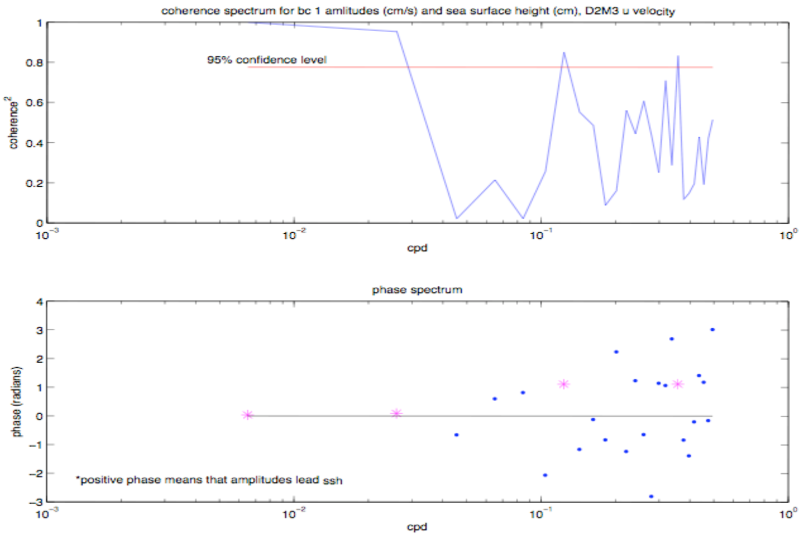

Figure A-68. Coherency (top) and phase (bottom) spectra of the temporal amplitudes of the first baroclinic mode for the east-west velocity component at mooring M3 during deployment 2 and the SSH gradient in the north-south direction.

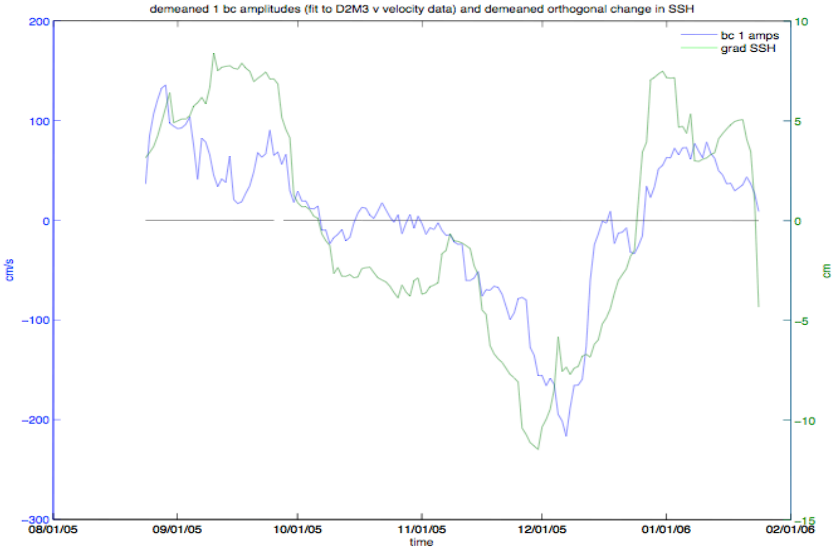

Figure A-69. Temporal amplitudes of the first baroclinic mode for the north-south velocity component at mooring M3 during deployment 2 (blue) and the SSH gradient in the east-west direction (green).

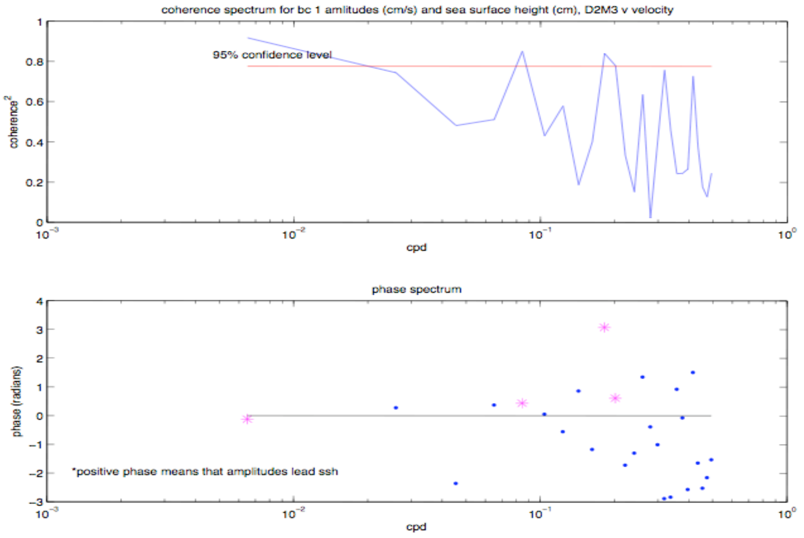

Figure A-70. Coherency (top) and phase (bottom) spectra of the temporal amplitudes of the first baroclinic mode for the north-south velocity component at mooring M3 during deployment 2 and the SSH gradient in the east-west direction.

APPENDIX B

Table B-1. Summary of the Dynamic normal mode decomposition of the EGOM data for east-west and north-south velocity components during deployment 1. F-test (t-test) refers to the fraction of time when F > 95 % confidence level (t ≥ 95 % confidence level). Correlation (C) and percent root mean squared error (% ERROR) of the mode fit to the data are depth-averaged values.

	D_0 mean (std)	**D_1 mean (std)**	**D_2 mean (std)**	**F-test**	**t-test BC1**	**t-test BC2**	**C**	**% ERROR**
M1								
u-component	1.43 (6.27)	30.17 (83.16)	27.25 (46.73)	93.83 %	93.99 %	59.60 %	0.96	8.96 %
v-component	1.07(4.81)	6.26(61.40)	-4.55(36.06)	95.41 %	93.51 %	54.58 %	0.96	9.06 %
M2								
u-component	5.04 (7.41)	89.59(91.50)	29.80(47.97)	91.48 %	92.02 %	63.41 %	0.95	12.07 %
v-component	-1.08(8.13)	-14.94(96.07)	-18.87(46.03)	91.15 %	89.62 %	58.98 %	0.94	12.93 %
M3								
u-component	6.67(7.00)	107.96(92.61)	20.02(60.32)	95.10 %	92.19 %	70.49 %	0.97	6.62 %
v-component	-1.86(8.14)	-47.17(91.65)	-29.81(58.62)	94.09 %	92.62 %	68.16 %	0.98	5.22 %

Table B-2. Summary of the Dynamic normal mode decomposition of the EGOM data for east-west and north-south velocity components during deployment 2. F-test (t-test) refers to the fraction of time when F > 95 % confidence level (t ≥ 95 % confidence level). Correlation (C) and percent root mean squared error (% ERROR) of the mode fit to the data are depth-averaged values.

	D_0 mean (std)	**D_1 mean (std)**	**D_2 mean (std)**	**F-test**	**t-test BC1**	**t-test BC2**	**C**	**% ERROR**
M1								
u-component	-5.70(3.27)	-59.64(40.49)	17.34(25.96)	94.45 %	93.70 %	57.92 %	0.92	19.54 %
v-component	3.03(3.07)	26.04(37.09)	-4.35(22.64)	83.70 %	82.85 %	39.64 %	0.92	19.74 %
M2								
u-component	-1.53(4.05)	-18.38(58.65)	35.47(39.15)	94.90 %	90.92 %	67.97 %	0.96	11.70 %
v-component	1.09(7.47)	15.62(74.46)	0.33(47.85)	96.58 %	96.06 %	63.48 %	0.97	8.76 %
M3								
u-component	4.83 (7.10)	87.50(80.15)	-38.68(75.52)	98.94 %	97.46 %	78.92 %	0.97	8.41 %
v-component	0.74(7.05)	8.35(72.60)	-21.37(85.14)	91.18 %	83.82 %	81.22 %	0.98	4.72 %

Table B-3. Time scales of the barotropic and first two baroclinic modes for east-west and north-south velocity components for EGOM data during deployment 1 based on the first zero crossing of the autocovariance function.

	Time Scale (days)		
	BT	**BC 1**	**BC 2**
M1			
u-component	21	22	29
v-component	23	23	24
M2			
u-component	34	33	5
v-component	23	23	9
M3			
u-component	13	13	6
v-component	25	39	7

Table B-4. Time scales of the barotropic and first two baroclinic modes for east-west and north-south velocity components for EGOM data during deployment 2 based on the first zero crossing of the autocovariance function.

	Time Scale (days)		
	BT	**BC 1**	**BC 2**
M1			
u-component	10	11	12
v-component	40	37	10
M2			
u-component	7	21	12
v-component	38	36	12
M3			
u-component	19	17	11
v-component	34	31	33

Table B-5. Percentages of kinetic energy in the barotropic (BT), first baroclinic (1BC), and second baroclinic (2BC) modes at each depth level at mooring M1 during deployment 1. The figure on the right is a summary plot of the Kinetic energy percentages in the table.

Depth	$\%T_{BT}(z_m)$	$\%T_{1BC}(z_m)$	$\%T_{2BC}(z_m)$
100 m	6.53 %	91.40 %	2.07 %
172 m	12.46 %	86.39 %	1.15 %
252 m	18.73 %	74.54 %	6.73 %
332 m	26.05 %	60.84 %	13.11 %
428 m	36.56 %	44.43 %	19.01 %
749 m	88.84 %	0.81 %	10.36 %
1244 m	50.80 %	47.30 %	1.91 %
1492 m	47.02 %	50.20 %	2.78 %
2499 m	45.82 %	51.09 %	3.09 %

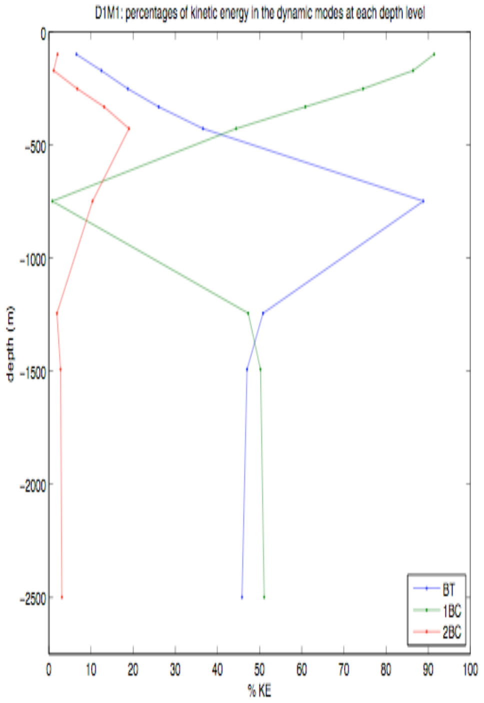

Table B-6. Percentages of kinetic energy in the barotropic (BT), first baroclinic (1BC), and second baroclinic (2BC) modes at each depth level at mooring M2 during deployment 1. The figure on the right is a summary plot of the Kinetic energy percentages in the table.

Depth	$\%T_{BT}(z_m)$	$\%T_{1BC}(z_m)$	$\%T_{2BC}(z_m)$
90 m	6.05 %	92.94 %	1.02 %
154 m	13.73 %	85.16 %	1.11 %
226 m	21.39 %	73.71 %	4.90 %
322 m	32.94 %	57.56 %	9.50 %
418 m	46.16 %	41.28 %	12.57 %
749 m	92.47 %	4.15 %	3.38 %
997 m	65.99 %	33.87 %	0.14 %
1244 m	52.55 %	46.03 %	1.42 %
1492 m	49.45 %	48.65 %	1.89 %
1995 m	48.67 %	49.30 %	2.03 %

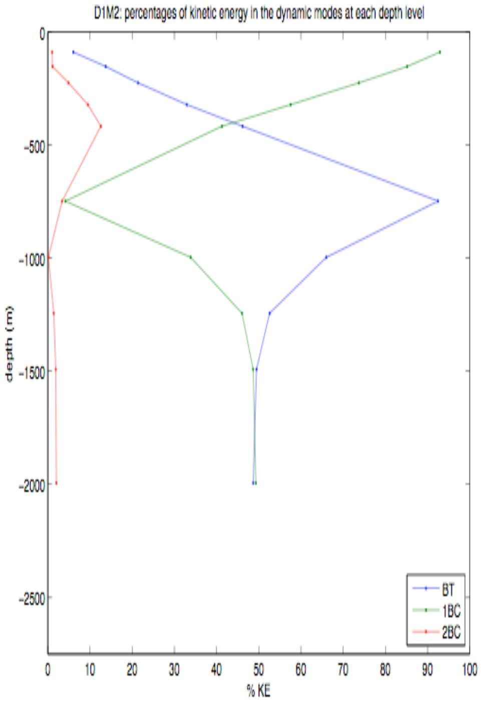

Table B-7. Percentages of kinetic energy in the barotropic (BT), first baroclinic (1BC), and second baroclinic (2BC) modes at each depth level at mooring M1 during deployment 2. The figure on the right is a summary plot of the Kinetic energy percentages in the table.

Depth	$\%T_{BT}(z_m)$	$\%T_{1BC}(z_m)$	$\%T_{2BC}(z_m)$
65 m	8.03 %	88.71 %	3.26 %
161 m	17.21 %	82.48 %	0.32 %
265 m	28.20 %	67.65 %	4.15 %
369 m	40.80 %	51.08 %	8.11 %
489 m	58.35 %	30.92 %	10.73 %
749 m	95.02 %	0.70 %	4.28 %
997 m	74.57 %	25.42 %	0.00 %
1492 m	57.05 %	41.68 %	1.28 %
1995 m	56.01 %	42.57 %	1.42 %
2499 m	55.98 %	42.59 %	1.42 %

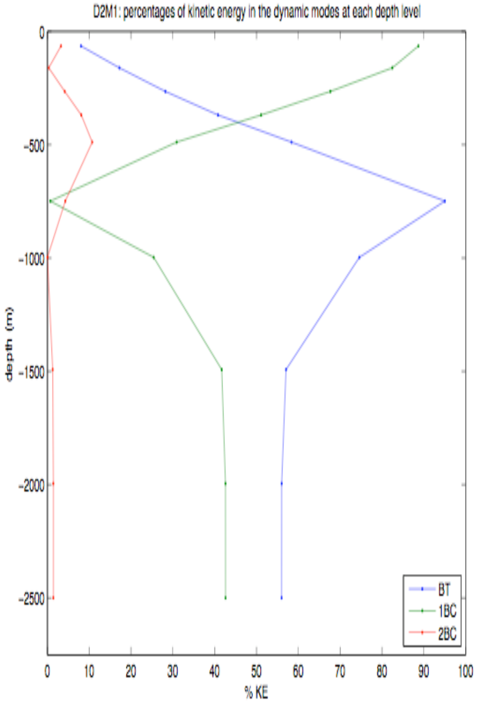

Table B-8. Percentages of kinetic energy in the barotropic (BT), first baroclinic (1BC), and second baroclinic (2BC) modes at each depth level at mooring M2 during deployment 2. The figure on the right is a summary plot of the Kinetic energy percentages in the table.

Depth	$\%T_{BT}(z_m)$	$\%T_{1BC}(z_m)$	$\%T_{2BC}(z_m)$
70 m	6.92 %	88.77 %	4.31 %
166 m	18.51 %	79.30 %	2.18 %
270 m	30.03 %	57.21 %	12.75 %
374 m	42.41 %	36.08 %	21.51 %
494 m	60.13 %	15.57 %	24.29 %
749 m	88.03 %	6.85 %	5.12 %
997 m	64.08 %	35.15 %	0.77 %
1244 m	53.47 %	43.23 %	3.30 %
1492 m	51.05 %	44.86 %	4.10 %
1995 m	50.56 %	45.18 %	4.26 %

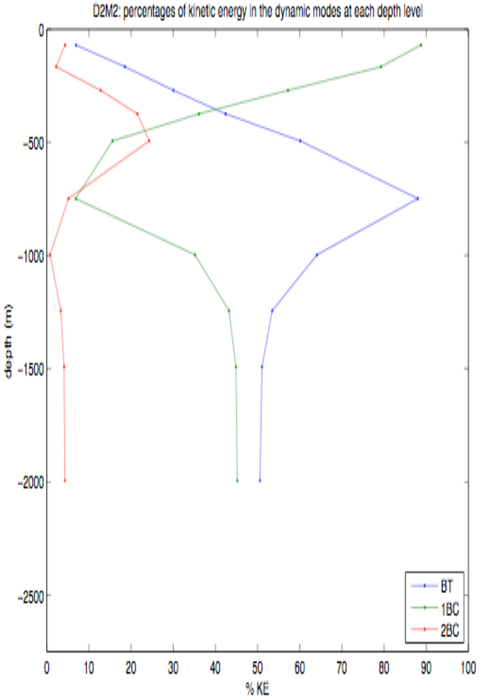

Table B-9. Percentages of kinetic energy in the barotropic (BT), first baroclinic (1BC), and second baroclinic (2BC) modes at each depth level at mooring M3 during deployment 2. The figure on the right is a summary plot of the Kinetic energy percentages in the table.

Depth	$\%T_{BT}(z_m)$	$\%T_{1BC}(z_m)$	$\%T_{2BC}(z_m)$
82 m	6.10 %	93.00 %	0.89 %
170 m	18.29 %	73.87 %	7.84 %
266 m	33.26 %	44.43 %	22.31 %
362 m	45.49 %	26.08 %	28.43 %
466 m	61.49 %	10.72 %	27.79 %
750 m	88.56 %	7.11 %	4.33 %
997 m	67.46 %	31.13 %	1.41 %
1245 m	58.56 %	37.30 %	4.14 %
1492 m	56.30 %	38.68 %	5.02 %
1996 m	55.45 %	39.19 %	5.37 %
2499 m	55.44 %	39.19 %	5.37 %
2699 m	55.44 %	39.19 %	5.37 %

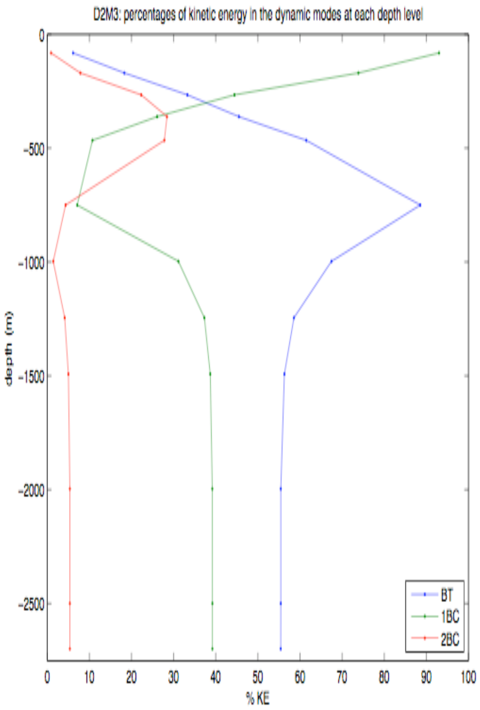

Table B-10. East-west and north-south velocity mode amplitude correlations at mooring M1 for deployment 1. Bold values indicate significant zero lag correlation at the 90% confidence level.

	East-west velocity			**North-south velocity**		
	BT	**BC 1**	**BC 2**	**BT**	**BC 1**	**BC 2**
BT	**1.00**	**0.91**	0.31	**1.00**	**0.86**	0.22
BC1	**0.91**	**1.00**	0.48	**0.86**	**1.00**	**0.42**
BC2	0.31	0.48	**1.00**	0.22	**0.42**	**1.00**

Table B-11. East-west and north-south velocity mode amplitude correlations at mooring M2 for deployment 1. Bold values indicate significant zero lag correlation at the 90% confidence level.

	East-west velocity			**North-south velocity**		
	BT	**BC 1**	**BC 2**	**BT**	**BC 1**	**BC 2**
BT	**1.00**	**0.52**	0.07	**1.00**	**0.87**	0.01
BC1	**0.52**	**1.00**	0.03	**0.87**	**1.00**	0.01
BC2	0.07	0.03	**1.00**	0.01	0.01	**1.00**

Table B-12. East-west and north-south velocity mode amplitude correlations at mooring M3 for deployment 1. Bold values indicate significant zero lag correlation at the 90% confidence level.

	East-west velocity			**North-south velocity**		
	BT	**BC 1**	**BC 2**	**BT**	**BC 1**	**BC 2**
BT	**1.00**	0.35	0.00	**1.00**	0.52	0.01
BC1	0.35	**1.00**	0.00	0.52	**1.00**	0.01
BC2	0.00	0.00	**1.00**	0.01	0.01	**1.00**

Table B-13. East-west and north-south velocity mode amplitude correlations at mooring M1 for deployment 2. Bold values indicate significant zero lag correlation at the 90% confidence level.

	East-west velocity			**North-south velocity**		
	BT	**BC 1**	**BC 2**	**BT**	**BC 1**	**BC 2**
BT	**1.00**	**0.65**	0.04	**1.00**	0.67	0.02
BC1	**0.65**	**1.00**	0.00	0.67	**1.00**	0.01
BC2	0.04	0.00	**1.00**	0.02	0.01	**1.00**

Table B-14. East-west and north-south velocity mode amplitude correlations at mooring M2 for deployment 2. Bold values indicate significant zero lag correlation at the 90% confidence level.

	East-west velocity			**North-south velocity**		
	BT	**BC 1**	**BC 2**	**BT**	**BC 1**	**BC 2**
BT	**1.00**	0.10	0.02	**1.00**	**0.85**	**0.61**
BC1	0.10	**1.00**	0.01	**0.85**	**1.00**	**0.60**
BC2	0.02	0.01	**1.00**	**0.61**	**0.60**	**1.00**

Table B-15. East-west and north-south velocity mode amplitude correlations at mooring M3 for deployment 2. Bold values indicate significant zero lag correlation at the 90% confidence level.

	East-west velocity			**North-south velocity**		
	BT	**BC 1**	**BC 2**	**BT**	**BC 1**	**BC 2**
BT	**1.00**	**0.60**	0.20	**1.00**	0.34	0.57
BC1	**0.60**	**1.00**	0.29	0.34	**1.00**	0.60
BC2	0.20	0.29	**1.00**	0.57	0.60	**1.00**

VITA

Kelly Lynne Cole received her Bachelor of Science degree in applied mathematics from Texas A&M University in 2004. She entered the Oceanography program at Texas A&M University in January 2006, and received her Master of Science degree in August 2008.

Ms. Cole's mailing address is 3146 TAMU, College Station, TX 77843. Her email is kcole@ocean.tamu.edu.